Ultra-thin mems fabricated tynodes for electron multiplication

Prodanovic, Violeta

DOI
10.4233/uuid:1f889837-0d94-415c-8137-6065c0a44245

Publication date
2019

Document Version
Final published version

Citation (APA)
Prodanovic, V. (2019). *Ultra-thin mems fabricated tynodes for electron multiplication*. [Dissertation (TU Delft), Delft University of Technology]. https://doi.org/10.4233/uuid:1f889837-0d94-415c-8137-6065c0a44245

Important note
To cite this publication, please use the final published version (if applicable).
Please check the document version above.

ULTRA-THIN MEMS FABRICATED TYNODES FOR ELECTRON MULTIPLICATION

ULTRA-THIN MEMS FABRICATED TYNODES FOR ELECTRON MULTIPLICATION

Proefschrift

ter verkrijging van de graad van doctor
aan de Technische Universiteit Delft,
op gezag van de Rector Magnificus prof. dr. ir. T.H.J.J. van der Hagen,
voorzitter van het College voor Promoties,
in het openbaar te verdedigen op
dinsdag 19 november 2019 om 15:00 uur

door

Violeta PRODANOVIĆ

Master of Science in Electrical Engineering and Computer Science,
Universiteit van Belgrado, Belgrado, Servië,
geboren te Zvornik, Joegoslavië.

Dit proefschrift is goedgekeurd door de

promotor: prof. dr. ir. P.M. Sarro
promotor: prof. dr. ir. H. van der Graaf

Samenstelling promotiecommissie:

Rector Magnificus,	voorzitter
Prof. dr. ir. P.M. Sarro,	Technische Universiteit Delft
Prof. dr. ir. H. van der Graaf,	Technische Universiteit Delft
Onafhankelijke leden:	
Prof. dr. J. Schmitz,	Universiteit Twente
Prof. dr. J.E.J. Schmitz,	Technische Universiteit Delft
Prof. dr. ir. P. Kruit,	Technische Universiteit Delft
Prof. dr. K. Desch,	Universität Bonn, Duitsland
Dr. G. Nutzel,	Photonis, Frankrijk

Keywords: Tynodes, ultra-thin membranes, timed-photon counter, secondary electron emission, atomic layer deposition

Printed by: Ipskamp

Front & Back: Cover design by Ipskamp and the author

ISBN 978-94-6384-085-9

An electronic version of this dissertation is available at
http://repository.tudelft.nl/.

And if you find her poor, Ithaka won't have fooled you.

C.P. Cavafy

CONTENTS

List of Acronyms and Symbols

δ	(Total) secondary electron yield
δ_m	Maximum secondary electron yield
$BSEY$	Back-scattered electron yield
E_a	Electron affinity
E_I	First crossover energy of PEs for which $\delta = 1$
E_{II}	Second crossover energy of PEs for which $\delta = 1$
E_m	Energy of primary electrons corresponding to maximum δ (δ_m)
E_{PE}	Energy of primary electrons
$FSEY$	Forward-scattered electron yield
REY	Reflection electron yield (calculated as: $REY = RSEY + BSEY$)
$RSEY$	Reflection secondary electron yield
TEY	Transmission electron yield (calculated as: $TEY = TSEY + FSEY$)
$TSEY$	Transmission secondary electron yield
Al_2O_3	Aluminium oxide, alumina
AlN	Aluminium nitride
BCl_3	Boront trichloride
C_2F_6	Hexafluoroethane
C_2H_2	Acetylene
Cs	Caesium
CsI	Caesium iodide
DCS, SiH_2Cl_2	Dichlorosilane
HCl	Hydrogen chloride
HF	Hydrofluoric acid
HNO_3	Nitric acid
KCl	Potassium chloride
KOH	Potassium hydroxide
$Mg(Cp)_2$	Bis(cyclopentadienyl)magnesium
$Mg(CpEt)_2$	bis(ethylcyclopentadienyl)magnesium
$Mg(OH)_2$	Magnesium hydroxide

$MgCO_3$	Magnesium carbonate
MgO	Magnesium oxide
NH_3	Ammonia
SiC	Silicon carbide
SiH_4	Silane
SiN, Si_3N_4	Silicon nitride
TMA, $Al(CH_3)_3$	Trimethylaluminium
AFM	Atomic force microscopy
ALD	Atomic layer deposition
BSE	Backscattered electron
CMOS	Complementary metal-oxide-semiconductor
CVD	Chemical vapour deposition
DFC	Dual Faraday cup
DRIE	Deep reactive ion etching
GPC	Growth per cycle
ICCD	International center diffraction database
LAPPD	Large-area picosecond photodetector
LPCVD	Low pressure chemical vapour deposition
MCP	Microchannel plate
MEMS	Microelectromechanical systems
MPCVD	Microwave-plasma enhanced chemical vapour deposition
NEA	Negative electron affinity
PE	Primary electron
PEALD	Plasma enhanced atomic layer deposition
PECVD	Plasma enhanced chemical vapour deposition
PET	Positron emission tomography
PMT	Photomultiplier tube
QE	Quantum efficiency
RIC	Radiation induced conductivity
RMS	Root mean square
RSEE	Reflection secondary electron emission
SE	Secondary electron
SE	Spectroscopic ellipsometry
SEE	Secondary electron emission

SEM	Scanning electron microscope
SEY	Secondary electron yield
TiPC	Timed photon counter
TSEE	Transmission secondary electron emission
UNCD	Ultrananocrystalline diamond
XPS	X-ray photoelectron spectroscopy
XRD	X-ray diffraction

SUMMARY

FOR decades, photomultiplier tubes (PMTs) have been the most common choice in single photon detection, covering the spectral range from deep-ultraviolet to near-infrared. PMT is a vacuum tube with three crucial components: photocathode, chain of dynodes and anode. At the photocathode, photons are converted to electrons in a photoelectric effect, after which they are directed to the dynodes chain. The material and geometry of dynodes are chosen to efficiently amplify the charge through the secondary electron emission (in reflection mode). Finally, created avalanche of electrons is collected and measured by the anode.

Timed Photon Counter (TiPC) is a novel vacuum-based photomultiplier proposed to overcome limitations of PMTs in terms of size, speed, spatial resolution and operation in the presence of magnetic field. The key novelty of TiPC is a tynode – a large-size array of ultra-thin, free-standing membranes which, in contrast to dynodes, multiply electrons in the transmission mode. Due to the short and straight crossing paths of electrons between subsequent tynodes, the time resolution of the TiPC can be in the order of 10^{-12} s. The set of tynodes is placed under the photocathode, and on top of a CMOS detecting chip. With such design, TiPC represents a light, compact and ultra-fast photodetecting device with a high relevance for solid state, atomic and molecular physics experiments, medical imaging and 3D optical imaging. The focus of this thesis is microelectromechanical systems (MEMS) fabrication of the tynodes. To our knowledge, this is the first time MEMS technology is employed as a powerful tool for the production of large arrays of free-standing membranes, with thicknesses of only a few nanometers, to be used in photodetection. Detailed analysis in terms of mechanical, optical, electrical and structural properties were performed in order to discern the most suitable material for the TiPC application among the investigated candidates. The transmission SEY (TSEY) of the released tynodes is analysed with a dedicated setup, specifically developed in our group, inserted in a scanning electron microscope (SEM).

Low pressure chemical vapour deposition (LPCVD) was employed as a technique to grow silicon nitride (SiN) tynodes with varied layout, elemental stoichiometry and thicknesses in the range from 25 to 40 nm. Due to its inability to produce good-quality films with thicknesses lower than 20 nm, LPCVD was replaced by atomic layer deposition (ALD). It was found that SiN performs poorly in terms of secondary electron emission (SEE), and we selected Al_2O_3 (alumina) as the next tynode material. The ALD of alumina is investigated in the temperature range from 300 down to 100 °C, with the goal to determine its viability in the coating of temperature-sensitive substrates such as photoresist. We demonstrated the fabrication of 5 – 25 nm-thick ALD alumina tynodes which exhibited moderately high TSEY. Apart from SiN and alumina, other materials subjected to SEE analysis in this work were: chemical vapour deposited (CVD) ultrananocrystalline

diamond (UNCD), monocrystalline silicon and LPCVD silicon carbide (SiC).

Applying atomic layer deposited magnesium oxide (MgO) as the tynode material resulted in a transmission secondary electron yield (TSEY) of up to 5.5, by which it proved to be the most efficient electron multiplier among materials taken into account in this work. During the fabrication of tynodes, SEE films were exposed to different MEMS processing steps, and thus inevitably undewent a surface modification which alters the SEE properties. On that account, we conducted a study on the ALD MgO films subjected to various chemical and thermal treatments and explored the methods to further enhance their SEE.

For the final application in the TiPC, stacked tynodes should provide the focusing of electrons. To meet this requirement, the emission film was grown on a pre-patterned substrate, which enabled hemi-spherical shape of the released membranes. Finally, for the vertical stacking and alignment of the tynodes, steps for the formation of V-grooves were added in the standard fabrication flowchart.

SAMENVATTING

AL voor decennia zijn fotomultiplicator buizen (PMTs) de gebruikelijke keuze ten behoeve van enkele foton detectie, met een spectraal bereik van diep ultraviolet tot nabij-infrarood licht. De PMT is een vacuüm buis met drie cruciale componenten: de fotokathode, een reeks van dynodes en een anode. In de fotokathode worden fotonen omgezet naar elektronen in een foto-elektrisch effect, waarna deze worden gericht op de reeks van dynodes. Het materiaal en de geometrie van de dynodes zijn zodanig gekozen dat de lading wordt versterkt door de secondaire elektron emissie (in reflectie modus). Uiteindelijk resulteert dit in een lawine van elektronen die worden opgevangen en gemeten op de anode.

De getimede foton teller (TiPC) is een vernieuwde fotonmultiplicator gebaseerd op vacuüm, die wordt voorgesteld om limitaties van PMTs te overwinnen in termen van grootte, snelheid, ruimtelijke resolutie en operatie in de nabijheid van een magnetisch veld. De sleutel innovatie van de TiPC is een tynode – een grote reeks van ultra dunne, vrijstaande membranen – welke, in contrast tot dynodes, elektronen multipliceren in de transmissie modus. Doordat de kruisende paden van elektronen tussen opvolgende tynodes kort en recht zijn, is het mogelijk dat de TiPC resolutie in de orde van 10^{-12} s kan zijn. De set van tynodes is geplaatst onder de fotokathode en bovenop een CMOS detectie chip. Met een dusdanig ontwerp, representeert de TiPC een licht, compact en ultra snel fotodetectie apparaat met een hoge relevantie voor vaste staat, atomische en moleculaire fysica experimenten, medische afbeelding en 3D optische afbeelding. De focus van deze dissertatie is micro elektromechanisch systeem (MEMS) fabricatie van de tynodes. Naar ons beste weten is dit de eerste keer dat MEMS technologie is gebruikt als een krachtig gereedschap voor de productie van grote reeksen van vrijstaande membranen, met een dikte van slechts enkele nanometers, ten behoeve van fotodetectie. Gedetailleerde analyse in termen van mechanische, optische, elektrische en structurele eigenschappen zijn uitgevoerd om het meest geschikte materiaal voor de TiPC applicatie te kunnen identificeren. De transmissie SEY (TSEY) van de vrijstaande tynodes is geanalyseerd met een setup, speciaal ontworpen in onze groep, welke in een scanning elektron microscoop (SEM) geplaatst kan worden.

Lage druk chemische damp depositie (LPCVD) werd gebruikt als techniek om silicium nitride (SiN) tynodes te groeien met gevarieerde geometrie, elementaire stoichiometrie en diktes in een bereik van 25 tot 40 nm. Vanwege de gebrekkige kwaliteit van lagen dunner dan 20 nm, is LPCVD vervangen door atomische laag depositie (ALD). Uit onderzoek bleek dat SiN slecht presteert in termen van secundaire elektron emissie en dus werd aluminiumoxide (Al_2O_3) geselecteerd als volgende tynode materiaal. De ALD van aluminiumoxide is onderzocht in het temperatuur bereik van 100 tot 300 °C, met als doel de mogelijkheid voor het coaten van temperatuur gevoelige substraten, zoals

foto lak, te onderzoeken. We hebben de fabricatie van 5 – 25 nm dikte ALD aluminium-oxide tynodes gedemonstreerd, welke een gemiddeld tot hoge TSEY toonden. Naast SiN en aluminiumoxide, werden ook chemische damp depositie (CVD) ultrananokristallijn diamant (UNCD), monokristallijn silicium en LPCVD silicium carbide (SiC) onderworpen aan SEE analyse in dit onderzoek.

Het toepassen van atomische laag depositie magnesium oxide (MgO) als het tynode materiaal, resulteerde in een secundaire elektron transmissie opbrengst (TSEY) tot 5.5, waarbij werd aangetoond dat dit de meest efficiënte elektron multiplicator is van de materialen die onderzocht zijn in dit onderzoek. Tijdens de fabricatie van de tynodes, werden SEE lagen blootgesteld aan verschillende MEMS fabricage stappen, welke dus onvermijdelijk oppervlakte modificatie ondergingen wat de SEE eigenschappen verandert. Omwille van die reden hebben wij de ALD MgO lagen, welke verschillende chemische en thermische behandelingen ondergingen, bestudeert en methodes om de SEE te verbeteren onderzocht.

Voor de uiteindelijke applicatie in de TiPC moeten gestapelde tynodes de elektronen voldoende focussen. Om deze eis te halen, werd een emissie laag gegroeid op een gepatterneerd substraat. Dit maakt het mogelijk om een halve bolvormige vorm te realiseren voor de vrijstaande membranen. Uiteindelijk werden de stappen om V-groeven te formeren toegevoegd aan het fabricatie stappenplan, ten behoeve van het verticaal stapelen en uitlijnen van de tynodes.

1

INTRODUCTION

1

1.1. DETECTION OF LIGHT

THE General Assembly of the United Nations proclaimed 2015 as the International Year of Light and Light-based Technologies. As stated in the adopted resolution, light science and technology "has revolutionized medicine, opened up international communication via the Internet, and continues to be central to linking cultural, economic and political aspects of the global society." [1]

The detection of light is one of the most crucial procedures in optics, equivalent in significance to light creation. The performances of photodetectors and light sources as central components in any optoelectronic system are invariably coupled. The design of a photodetector and choice of material is dictated by the end application and the portion of optical spectrum that the device is meant to analyse.

Semiconductor materials benefit from the internal photoelectric effect, i.e. the process of electron-hole pairs creation as a response upon absorption of photon with energies equal or larger than their band gap. Moreover, the blooming of the semiconductor industry made these materials an economically advantageous choice for a large variety of light detecting devices, such as photodiodes, phototransistors and solar cells. Some of the remarkable attributes of semiconductor photodetectors are their compact size, low bias voltage and wide spectral range, and one of their most significant application is in fiber-optic communications for receiving near-infrared wavelengths. Figure 1.1 shows typical commercially available semiconductor based devices for detecting light in different spectral regions and for different applications.

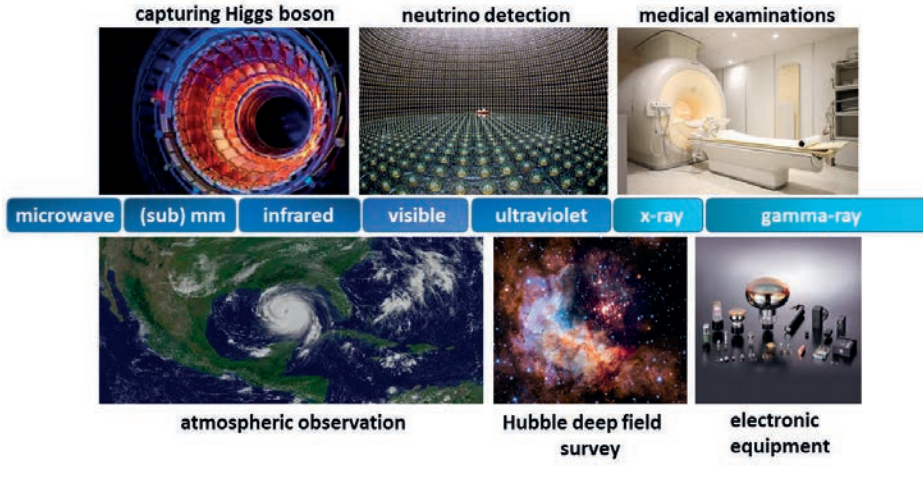

Figure 1.1: Applications of photodetectors over different regions of the radiation spectrum.

One of the most challenging tasks in photodetection is the detection of a single photon, with extraction of its time of arrival to the detector and spatial information (regard-

ing the initial location of a photon). Such measurement of light with ultimate sensitivity is essential in numerous applications in particle physics, medicine, automated optical sensing and material science. Up to now, one of the most widely used devices for the detection of a single photon has been the photomultiplier tube (PMT). PMT was historically the first type of photodetector: its concept was proposed a century ago by J. Slepian in 1919 [2] and a working device was reported in 1936 by V. Zworykin [3]. The development of PMTs was enabled by two prior achievements: the separate discoveries of the photoelectric effect and of secondary electron emission. PMT is essentially a vacuum tube with an operating principle that can be divided into three stages, as schematically illustrated in Figure 1.2a:

- Incident low-energy (soft) photons are converted to electrons at the photocathode, due to the photoelectric effect;
- Electrons, accelerated by an electric field, are directed towards the chain of electrodes named dynodes. Upon impact of incoming electrons, low energetic secondary electrons are emitted from the surface of each dynode;
- An avalanche of electrons is collected by an anode output electrode.

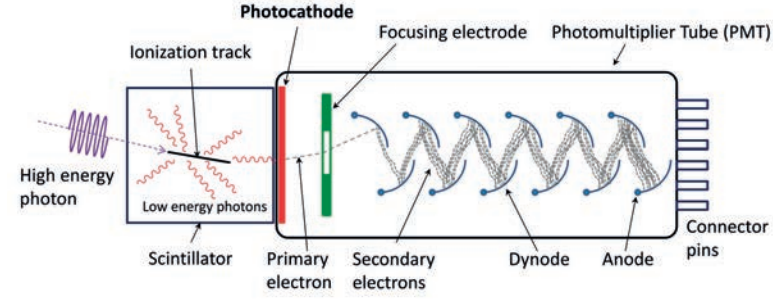

(a)

(b)

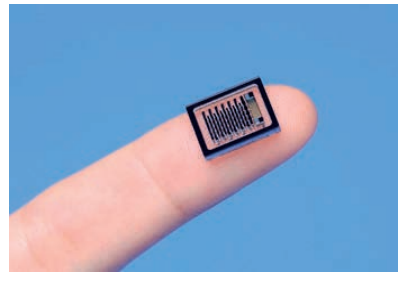

(c)

Figure 1.2: (a) Basic structure and operation principle of a PMT, illustration adapted from [4]; (b) commercially available PMTs of different sizes, image taken from [5]; (c) micro-PMT developed by Hamamatsu is a portable version of a photosensing instrument, much lighter and smaller than a conventional PMT [6].

The design of PMTs has been refined over the years and their performance improved

due to development of photocathodes and to the optimization of dynode stages with regard to geometry and a material choice. They can be fabricated in a variety of formats (Figures 1.2b and 1.2c), including very large areas of up to 50×50 cm^2. Owing to their efficiency, time resolution, low noise, and low power consumption, PMTs continue to be widely used as extremely sensitive photodetectors in the visible, ultraviolet and near infrared range of radiation. Even with recent development of solid-state based photodetectors, such as silicon photomultiplier (SiPM), PMT still remains a paramount choice in many applications where single photon detection with extremely low dark current (down to 10^{-18} A/cm^2) is demanded. Namely, CMOS imagers have a dark current 4 to 8 orders of magnitude larger than photocathode based electron multipliers [7]. There are, however, four major limitations associated to a PMT with a design as described above:

- Lack of spatial resolution;
- Relatively large size, with a bulky chain of dynodes being usually 3 to 8 times larger than a photocathode;
- Degradation of performance in the presence of magnetic field (such as in magnetic resonance imaging, MRI);
- High costs.

This set of disadvantages originates largely from the long trajectories of reflected secondary electrons over the dynode chain. Crossing of electrons along zig-zag lines greatly affects the speed and enlarges the size of a PMT, the resolution and the costs. In order to surpass the abovementioned pitfalls, and preserve the benefits of PMTs at the same time, we propose a novel photomultiplier based on ultra-thin dynodes operating in transmission mode.

1.2. TIMED PHOTON COUNTER (TIPC) AND MEMS FABRICATED TYNODES

To reduce the size of a photodetecting device and further increase its speed, the reflection of secondary electrons from a dynode surface ought to be replaced by another multiplication mechanism. Utilizing ultra-thin membranes instead of bulky dynodes will provide efficient creation of secondary electrons in transmission mode. Furthermore, vertical stacking of these membranes with spacing in the order of a hundred of micrometers, and setting them at different potentials (of up to 1 kV difference between two consecutive tynodes), guarantee a very fast and straightforward motion of electrons inside the detector.

As previously mentioned, most of commercially available PMTs are not able to provide spatial information on the detected photons. To address this problem, we utilize an all-digital TimePix CMOS chip for detection of charge signal exiting the bottom tynode [8]. A TimePix chip allows for measurement of arrival time, “time-over-threshold” (TOT), and/or event counting independently in each pixel, by using an external reference clock [9]. Hence, mapping out the spatial path of an incoming photon is enabled

after activation of a certain pixel on the sensing chip placed under the multiplication unit. To ensure the mechanical stability, the tynode itself is designed as a large-size array of freestanding membranes, rather than just a single large area membrane. Moreover, a matrix of membranes is designed with a geometry similar to that of TimePix chip, as will be shown in later chapters.

The combination of the transmission dynodes, named herein as **tynodes**, and the TimePix chip gives an advanced type of detector for photons, electrons and energetic charged particles. A stacked set of curved miniature tynodes in vacuum in itself is an efficient single free electron detector. By capping the system with a traditional photocathode, a highly sensitive single soft photon counter, named TImed Photon Counter (TiPC), can be realized. The amplification provided by the tynodes is essentially free of noise in terms of dark current, bias current and dark counting rate. The time resolution of this device can be in the order of a few picoseconds since the electron crossing paths between two tynodes are effectively uniform and two orders of magnitude smaller than in conventional PMTs.

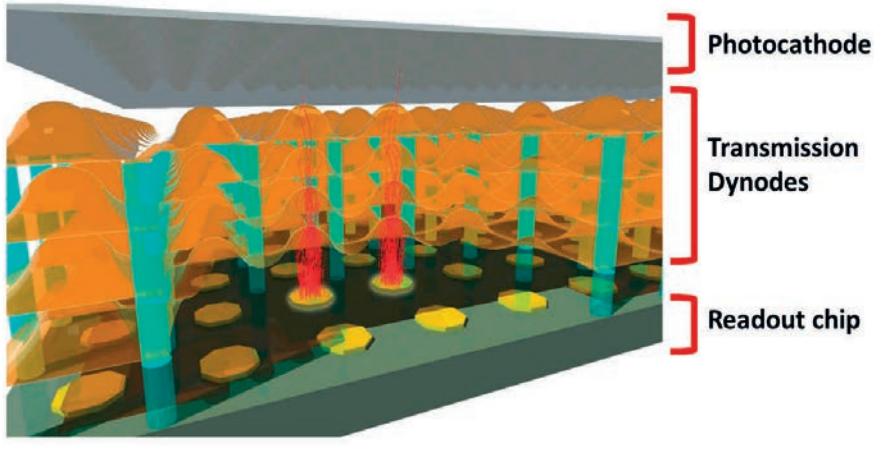

Figure 1.3: The core element of the TImed Photon Counter is a set of vertically stacked transmission dynodes (tynodes) for electron multiplication. The amplifying unit is placed in between a photocathode on top and a CMOS detecting chip on bottom. Illustration adopted from [10].

Consequently, TiPC, being a planar, light and compact device, can satisfy a wide range of application needs and replace any existing PMT. In fact, the performance of positron emission tomography (PET) medical imaging scanners would greatly benefit by the utilization of TiPC, on ccount of the fact that its performance is not affected by magnetic field [11]. Moreover, this photomultiplier would be relevant for solid state, atomic and molecular physics experiments, and commercial applications such as fast 3D optical imaging or night goggles.

This thesis focuses on the realization and performance analysis of tynodes for ap-

plication in TiPC. Here reported experiments have been conducted with the main aim to:

- Identify an efficient secondary electron emitter;
- Explore methods which may increase the secondary electron emission of that material;
- Design and produce the tynodes which are ready for assembly in the TiPC.

The choice of materials we studied was governed by several requirements, the first one being the secondary electron yield (SEY), with the desired value of 4 or higher for here aimed application. This property has been widely investigated for a range of insulators that are, unlike (semi)conductors, efficient secondary electrons emitters. Most of previous work in this field dates from 1950s and report on reflection SEY (RSEY) [12], mainly due to technological limitations in the fabrication of very thin membranes. In this work we give a characterization of different materials employed as electron multipliers in a transmission configuration. For the first time microelectromechanical systems (MEMS) technology is employed as a powerful tool for the fabrication of large arrays of free-standing membranes, with thicknesses of only a few nanometers, to be used in photodetection. Moreover, MEMS large scale production of tynodes would significantly reduce costs of TiPC compared to existing photodetectors for similar applications. In this regard, it is important to take into account additional requirements in the choice of the tynode material:

- Deposition method must provide continuous, pinhole-free layers with thicknesses of only a few nm;
- Mechanical properties of these layers should enable the fabrication of robust, large and ultra-thin free-standing membranes;
- A controllable fabrication method should be developed for the realization of the arrays of free-standing membranes.

We investigated suitability of various MEMS methods for growing the thin tynode films, developed and tailored the fabrication process for the release of tynodes of different thicknesses and of several materials. Namely, low pressure chemical vapor deposition (LPCVD) and atomic layer deposition (ALD) were employed for growing silicon nitride (SiN), alumina (Al_2O_3) and magnesium oxide (MgO) tynodes, among others. The transmission SEY (TSEY) of the released tynodes is analysed with a specifically developed setup inserted in a scanning electron microscope (SEM). Finally, as a validation of the proposed novel concept, we report on:

- The performance of the tynodes, in terms of TSEY vs. energy of primary electrons characteristic;
- The first attempts to stack the tynodes and achieving their precise alignment.

1.3. OUTLINE OF THE THESIS

SEVERAL materials and processing schemes for the fabrication of ultra-thin tynodes to be implemented in the novel TiPC are investigated. Detailed analysis in terms of mechanical, optical, electrical and structural properties is performed in order to discern the most suitable material among the investigated candidates.

In Chapter 2 we explain the working principle of photomultiplier tubes and briefly recap the theory on reflection secondary electron emission (RSEE), the mechanism on which the performance of PMTs is based. This is followed by a short literature review on materials with high RSEY. Moving ahead, we set out the transmission secondary electron emission (TSEE) as an introduction to the operating principle of TiPC. In the similar manner, the part on TSEE is finalized by listing the materials with significantly high TSEY. In Chapter 3, the flowchart for fabrication of LPCVD SiN tynodes with different elemental stoichiometry and layout is introduced. An overview of abovementioned properties of SiN is presented together with the characterization techniques used. Chapter 4 focuses on applicability of atomic layer deposition (ALD) for the manufacturing of tynodes. In particular, we study aluminium oxide (Al_2O_3, alumina) membranes with different thicknesses and compare them to previously studied SiN tynodes. Chapter 5 contains discussion on ALD magnesium oxide (MgO) as a tynode material and demonstrates its advantages for this application over other candidates. During the fabrication of tynodes, SEE films are exposed to different MEMS processing steps, and thus inevitably undergo a surface modification which alters the SEY. On that account,this chapter also gives a study on the RSEY of ALD MgO films subjected to various chemical and thermal treatments. Chapter 6 presents a study on electron multiplication of four additional materials: ultra-nanocrystalline diamond (UNCD), aluminium nitride (AlN), silicon, and silicon carbide (SiC). Moreover, here we present the improvements in the design of tynodes which help in minimizing charging-up. An aluminium grid is implemented as a substrate for the deposition of MgO, as the tynode material, to supress severe charging of the supporting SiN mesh. Moving further, we present the realization of ALD alumina tynodes with different radius of curvature, as well as a method for stacking them.

REFERENCES

[1] http://www.light2015.org/Home/About/IYL-Final-Report.html.

[2] S. Joseph. Hot-cathode tube, 1923. US Patent 1,450,265.

[3] V.K. Zworykin, G.A. Morton, and L. Malter. The secondary emission multiplier-a new electronic device. *Proceedings of the Institute of Radio Engineers*, 24(3):351–375, 1936.

[4] https://en.wikipedia.org/wiki/Photomultiplier_tube.

[5] https://www.flickr.com/photos/tsiklonaut/8685632278.

[6] https://www.hamamatsu.com/eu/en/product/optical-sensors/pmt/micro-pmt/index.html.

[7] P. Seitz and A.J.P. Theuwissen. *Single-photon imaging*, volume 160. Springer Science & Business Media, 2011.

[8] https://medipix.web.cern.ch/technology-chip/timepix-chip.

[9] X. Llopart, R. Ballabriga, M. Campbell, L. Tlustos, and W. Wong. TimePix, a 65k programmable pixel readout chip for arrival time, energy and/or photon counting measurements. *Nuclear Instruments and Methods in Physics Research Section A: Accelerators, Spectrometers, Detectors and Associated Equipment*, 581(1-2):485–494, 2007.

[10] H. van der Graaf, H. Akhtar, N. Budko, H.W. Chan, C.W. Hagen, C.C.T. Hansson, G. Nützel, S.D. Pinto, V. Prodanović, B. Raftari, and et. al. The tynode: A new vacuum electron multiplier. *Nuclear Instruments and Methods in Physics Research Section A: Accelerators, Spectrometers, Detectors and Associated Equipment*, 847:148–161, 2017.

[11] P. Lecoq, E. Auffray, S. Brunner, H. Hillemanns, P. Jarron, A. Knapitsch, T. Meyer, and F. Powolny. Factors influencing time resolution of scintillators and ways to improve them. *IEEE Transactions on Nuclear Science*, 57(5):2411–2416, 2010.

[12] Hajo Bruining. Physics and applications of secondary electron emission. 1954.

2

SECONDARY ELECTRON EMISSION AND ITS ROLE IN PHOTODETECTORS

In this chapter we discuss the development of vacuum-based single photon detectors, starting with the concept of photomultiplier tubes (PMTs). To comprehend the working principle of the PMTs and for a better grasp of novel developments of imaging devices, it is necessary to briefly describe the theory of photoelectric effect and secondary electron emission.

2.1. PHOTOMULTIPLIER TUBES

PHOTOMULTIPLIER tubes (PMTs) are still widely used in low light-level measurements, covering the spectral range from deep-ultraviolet to near-infrared region and enabling single-photon detection in numerous applications, such as high energy physics experiments, medical equipment, biotechnology-related equipment, oil well logging devices, and astronomical observation equipment [1] [2]. A PMT converts light into an electrical signal and amplifies it to the required detection level by means of secondary electron emission. Its main elements are an input window, a photocathode as a photosensitive surface, electrodes for electron multiplication (dynodes) and an anode, all sealed in a vacuum container as shown in Figure 2.1. The output signal is produced in the following three stages:

1. **Electron generation**: light passes through the input window and hits the photocathode. Due to the photoelectric effect, photoelectrons are emitted into the vacuum;
2. **Multiplication**: photoelectrons are then accelerated and focused onto the first dynode which creates secondary electrons. The process of secondary emission is repeated in all successive dynodes, each put at a different potential, to ensure the energy of electrons is adequate for multiplication;
3. **Detection**: a cluster of electrons is multiplied up to $\delta^N = 10^7$ times (where δ represents multiplication of each stage, i.e. the secondary electron yield of the dynode material, and N is the number of dynode stages), and collected by the anode.

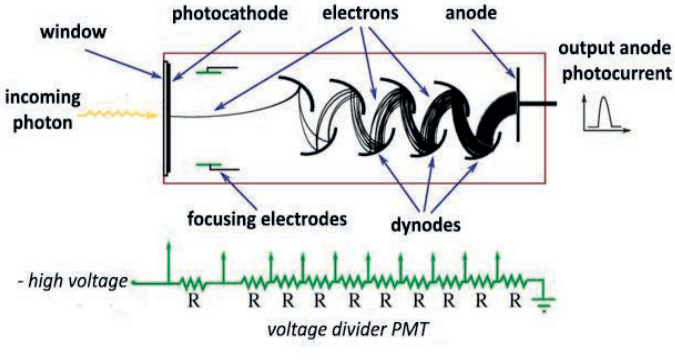

Figure 2.1: Cross-section of a PMT illustrating the components and the operation mechanism of the device [2].

2.1.1. PHOTOCATHODES

The two phenomena crucial for the operation of a PMT are the photoelectron emission and the secondary electron emission. Photoelectron emission may refer to an internal photoelectric (photovoltaic) effect in which, upon the absorption of photons, electrons are excited to the conduction band in a semiconductor material. Photoemission can be split into three steps:

1. Incident photons impart their energy ($h\nu$) to electrons in the valence band;

2. Electrons in the conduction band diffuse through the material, possibly losing some energy;

3. Electrons which reach the surface of the material may escape into the surrounding vacuum, if they are sufficiently energized.

The ratio of electrons emitted from the photocathode and the incoming photons is the quantum efficiency (QE) of a material, $\eta(\nu)$. This ratio depends on the wavelength of the incident light and the properties (composition and thickness) of the photoemissive material, as described by the Spicer's three step model [3]:

$$\eta(\nu) = (1-R)\frac{P_\nu}{k}\left(\frac{1}{1+\frac{1}{kL}}\right)P_s, \tag{2.1}$$

where R, k and P_ν represent, respectively, reflection coefficient, full absorption coefficient of photons, and probability that absorbed photons with frequency ν may excite electrons to energies higher than the vacuum level. The diffusion length of electrons (L) can be increased by a proper choice of the photocathode crystal. Finally, P_s stands for the probability that electrons, transported to the surface of a photocathode, may escape to the vacuum (P_s). This parameter is largely influenced by the electron affinity (E_a), which is the difference between vacuum level and the conduction band, as can be seen in the band model of an alkali photocathode (Figure 2.2a). The surface of a photocathode can be activated in such a way that the energy band bends down, resulting in a negative value of E_a. As an illustration, the band model of a GaAsP negative electron affinity (NEA) photocathode is shown in Figure 2.2b.
After photoemission, the following stage in operation of PMTs is a multiplication of electrons at the dynodes. Just like photocathodes, dynodes should meet the requirement of a low work function (preferrably negative electron affinity, NEA) at the surface, in order to promote the ejection of electrons. The same condition is essential for the emission surface of dynodes operating in transmission mode.

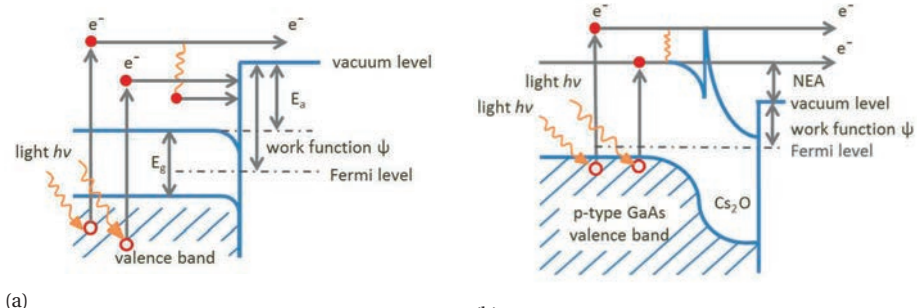

Figure 2.2: Band model of an alkali (a) and III-V semiconductor (b) photocathode. Graphs adapted from [2].

2.1.2. DYNODES AND SECONDARY ELECTRON EMISSION (SEE) PROCESS

As stated previously, photoelectrons emitted from the surface of a photocathode are directed onto a chain of dynodes. The arrangement of dynodes is carefully planned with respect to their size and shape, as well as to the supply voltage, optimised time resolution, 2D calculations of electron trajectories in the presence of complicated electric field, and amplification provided by the dynode material. The array of dynodes initially required 14 – 16 stages to achieve the gain of $\sim 10^8$ to provide a single-photon detection. With discovery of more efficient secondary electron emission materials, and by implementing surfaces like tricesium antimony (Cs_3Sb) and cesiated gallium phosphide (GaP:Cs), the number of dynodes has been reduced to 8 – 12 [4]. Other efficient dynode materials include beryllium oxide (BeO), magnesium oxide (MgO) and gallium arsenide phosphide (GaAsP), usually deposited as thin films onto a curved metal electrode.

2.2. REFLECTION SECONDARY ELECTRON EMISSION (RSEE)

SECONDARY electron emission (SEE) is a fundamental process in the operation of various vacuum electronic devices. In some applications, a chosen material must suppress the generation of secondary electrons, whereas in others high SEE materials are desirable. For example, low SEE coatings are used as collectors in microwave and millimeterwave power tubes, or to reduce the multipactor discharge (a resonant vacuum discharge frequently observed in microwave systems) [5] [6] [7]. On the other hand, films with enhanced emission of secondary electrons are employed in electron multipliers [8] and as cathodes in crossed-field amplifiers (magnetron-based type of microwave amplifiers) [9].

Emission of secondary electrons (SEs) from the material surface is induced by electron or ion bombardment of the material. Due to a large difference in the masses of electrons and ions, the energy of an ion beam needed to induce maximum SEY is typically in the MeV energy range. At the energy position of maximum SEY induced by electrons (a few hundreds eV) in metals, ion-initiated electron emission is approximately one to two orders of magnitudes lower than the electron-induced SEE, the latter one normally having values near or greater than unity [10]. Ion-induced SEE is of great importance for the operation of electron multipliers in mass spectroscopy or cathodes [11], but it is not the focus of this work. The electron-matter interaction which results with the emission of SEs can be divided in three subsequent steps [12], as illustrated in Figure 2.3:

1. **Generation**: the production of internal SEs in material upon the impact of primary electrons (PEs). The number of excited SEs depends on the energy of PEs.
2. **Transport**: propagation of SEs through the material toward the surface. A number of produced SEs reaches the material surface, losing their energy in various scattering processes.
3. **Escape**: crossing of SEs from the material into the vacuum.

To further discuss SEE mechanism, it is necessary to introduce two new parameters: penetration depth and escape depth. **Penetration depth** is defined as the average distance between the PE impact spot and the point where PEs are stopped in the material.

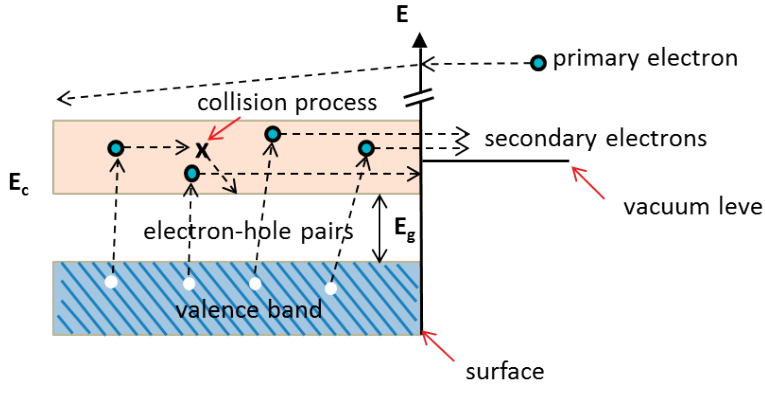

Figure 2.3: Schematic drawing of the SEE process in a semiconductor material. Image adapted from [13].

It strongly depends on the energy of PEs and material properties (density, band gap energy, atomic weight, etc.). Penetration range of a large group of materials is tabulated in databases provided by the National Institute of Standards and Technology (NIST) [14]

The distance between a surface which emits SEs and the point in the bulk from which SEs are still able to escape the material, is defined as the **escape depth**. SEs in metals lose their energy predominantly through interactions with other electrons and, to a lesser extent, with lattice vibrations and defects. In insulators, on the other hand, interactions between SEs excited into the conductive band and electrons in the valence band are obstructed by a large band gap. For that reason, escape depth in insulators is much larger than in conductors (10 – 50 nm, as opposed to 0.5 – 1.5 nm [15] [16]). Hence, conductive materials exhibit poor SEE behaviour, even though the number of initially generated SEs is large.

As mentioned in Section 2.1.1, secondary electrons reaching the surface of the irradiateds semiconductor or insulator can escape into the vacuum if their energy allows them to overcome the potential barrier - **electron affinity** (E_a) at the surface. In the presence of a positive electron affinity, the majority of the secondary electrons will be reflected or trapped. However, a negative electron affinity (NEA) helps the emission of SEs into the vacuum. In metals, on the other hand, the work function requires a minimum escape energy typically larger than 10 eV, which is another reason why they display low SEY. Typically, SEY of metals is in the range of 0.5 – 2 [17], whereas insulators and semiconductors in some cases can exhibit SEY greater than 100 (see the discussion in Section 2.2.1).

Evidently, insulators are applied where materials with enhanced SEE are demanded. Still, a surface potential created by the presence of induced negative charge (due to the absorption of a number of incident electrons) and induced positive charge (due to the emission of the SEs), degrades the SEE yield of a dielectric material [18] [19]. Similar effect on the SEE performance of insulators is produced by electron-hole recombina-

tion. This aspect, together with common techniques for the charge neutralization, will be discussed in Section 2.5.

In the reflection SEE process (RSEE), three groups of electrons are generated: backscattered electrons (BSEs), re-diffused electrons, and "true" secondary electrons. Backscattered electrons are primary electrons that are elastically reflected by atoms at the surface of the material. Thus, their energy is smaller than the primary electron one, E_{PE}. Re-diffused electrons are primary electrons that have undergone inelastic collisions inside the material and have lost energy due to scatterings with phonons, impurities, or other electrons. With an arbitrary adopted rule, their energy level is below E_{PE}, but larger than 50 eV [20] [21]. Secondary electrons, originated from the bombarded material and forced out into the vacuum by primary electron impact are referred to as "true" secondary electrons (here addressed simply as secondary electrons, SEs) and have energies below 50 eV.

SEE has been the subject of numerous theoretical studies, with the goal to determine empirical equations for the dependence of the total secondary electron yield (SEY) on the energy of primary electrons and/or their incident angle with respect to the surface. The major contribution to the development of theoretical models of SEE from solids was provided by Bruining [20], Jonker [22], Lye and Dekker [23], Dionne [24], and recently in a work by Joy and Lin [25] where SEE behaviour of 44 elements is examined and related to their atomic number. In spite of all the efforts, SEE mechanisms are still quantitatively not well interpreted and no "universal law" which applies to a large group of materials has been demonstrated yet. Moreover, the published experimental results on SEY greatly depend on the used measurement method.

SEY is generally defined as the ratio of the number (current) of emitted electrons to the number (current) of incident electrons (I_0):

$$SEY = \delta = \delta_{SE} + \delta_{BSE} = \frac{I_{SE} + I_{BSE}}{I_0} \tag{2.2}$$

In the Equation 2.2, emitted electrons include contribution of backsctattered (and re-diffused) electrons (δ_{BSE}) and SEs (δ_{SE}). Constituent δ_{SE} is often refered to as "true" SEY. In this work, the term SEY is used as equivalent of total SEY (δ).

Most commonly, SEE in reflection configuration is analysed by the δ plot versus the energy of incident electrons, as shown in Figure 2.4. The yield originating from BSEs is flattened and has a slight variation over the range of incident energy. Accordingly, the shape of SEY is mostly governed by δ_{SE} component. The single-peaked SEY curve has three characteristic points: crossover energies E_I and E_{II} for which SEY = 1, and a primary energy E_m at which SEY reaches its maximum value (δ_m).

At energies $E_{PE} < E_I$, the penetration depth is smaller than the escape depth and the majority of generated SEs can escape the material. However, δ is still smaller than unity, since not many SEs can be produced by the impact of low energetic PEs. On the other hand, high energetic PEs ($E_{PE} > E_{II}$) efficiently generate SEs, but at sites which are too deep in the bulk of the material. These SEs recombine on the trajectory towards the surface, thus lowering the value of δ below 1. Electron multiplication arises in the region between the two cross-over energies ($E_I < E_{PE} < E_{II}$). We distinguish three segments of the SEY curve:

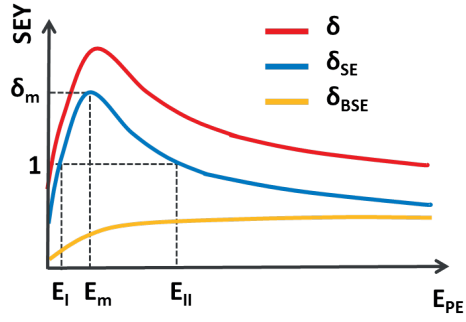

Figure 2.4: SEY in the reflection mode versus energy of PEs.

1. When $E_{PE} < E_m$ the penetration depth is smaller than the escape depth and δ is increasing with E_{PE};

2. At $E_{PE} = E_m$ the penetration depth is equivalent to the escape depth and δ reaches its maximum value (δ_m), often referred to as *the* SEY (this annotation will be kept throughout following chapters);

3. For higher energies of PEs ($E_{PE} > E_m$) the large escape depth prevents the escape of the majority of SEs.

2.2.1. MATERIALS WITH HIGH REFLECTIVE SECONDARY ELECTRON YIELD (RSEY)

A variety of compound insulators, mainly alkali halides and alkaline earth compounds, have been investigated for application in photomultipliers. The large discrepancy in RSEY results of the material analysed by different groups can be explained by non-identical preparation conditions and measurement methods. A short literature overview of RSEY of various materials (including the ones investigated in our study) is given in Table 2.1. Due to a lack of morphological and composition characterization of the materials in these early studies, the results are hard to compare and should be taken with precaution. For example, for a pore-free polycrystalline alumina ceramic [26], two largely different values were measured: 6.4 and 19 [27], and for MgO a maximum RSEY in the range from 3 to 24 has been reported [28] [29]. One of the most attractive electron emission materials is diamond. Its excellent transport properties include large escape depth and a rather simple surface treatment method for introducing the negative electron affinity (NEA) at the surface (H, Cs and Cs-O termination). Doping (by boron or nitrogen), thickness and crystallographic properties are some of the parameters which determine the RSEE behaviour of diamond, with maximum yields varying across a large range, from 3 to 132 [30]. Most of these materials have been applied as dynode coatings in traditional PMTs. With the development of miniaturized PMTs based on microchannel plates (MCPs) in the late 1990s, novel deposition techniques have been explored for the application of these materials in electron multiplication. The following section briefly describes the working principle of MCP PMTs and gives an overview of atomic

Reflection dynode material	δ_m	E_m (keV)	Reference
Lucalox alumina	19	1.3	[27]
polished Lucalox alumina	6.4	0.65	[27]
MgO crystals	24.3	1.3	[28]
electron beam evaporated MgO	3.3	0.7	[29]
microcrystalline CVD diamond	14	0.7	[31]
nanocrystalline CVD diamond	12	0.7	[31]
ultra-nanocrystalline CVD diamond	8.3	0.7	[31]
single-crystal C(100) diamond	3	0.65	[30]
single-crystal C(100) diamond terminated with Cs	132	2.9	[30]
ALD Al_2O_3	2.9	0.25	[32]
ALD MgO	6.9	0.45	[32]

Table 2.1: List of materials with a maximum RSEY (δ_m) higher than 3, measured for the energy E_m of the incident beam.

layer deposited (ALD) films used to provide high SEE in the microchannels. More details on ALD of materials utilized in this work are given in Chapters 4 – 6.

SEE MATERIALS IN DETECTORS BASED ON MICROCHANNEL PLATES (MCPS)

Microchannel plate (MCP) PMT is a very attractive photon sensor for low light level applications in strong magnetic fields (> 1 T). Fundamentally, this photodetector is built by assembling many channel electron multipliers with a small diameter, with the design characteristics as listed in Table 2.2. The outlook of MCP and its main components are presented in Figure 2.5, together with a multiplication mechanism inside a single channel. Fabrication of tilted MCP channels helps in eliminating the ion-feedback, and a carefully designed stack of two MCP stages can provide a gain of $10^6 - 10^7$ (typical for "Chevron" configuration [33]). Thus, compact MCPs, consisting of a single continuous dynode, were offered as a replacement for a dynode cascade and have therefore significantly reduced the bulky size of PMTs. Moreover, the operation of MCPs is not hindered by magnetic fields and these photodetectors are considerably faster compared to the traditional PMTs, with a jitter time of only 20 ps [34].

Parameter	Range
Pore diameter (d)	(6 – 25) µm
Channel length (L)	(400 – 1000) µm
Diameter-to-length ratio ($\alpha = L/d$)	40 – 100
Open-area ratio	(55 – 65)%

Table 2.2: Geometrical features of MCPs [35].

The MCP surface must be functionalized with conformal layers of materials which have well-controlled conductivity as well as high SEY in reflection mode (RSEY). So far, atomic layer deposition (ALD) proved to be the best method for coating the MCP channels [36]. This approach was first used in Planacon, an MCP PMT-based family of prod-

ucts developed by Photonis. Planacon is a square-shaped photodetector with an active area of 53 × 53 mm^2, convenient for tiling together to image large areas [37]. Use of ALD emissive layers has also been reported by Large-area Picosecond Photodetector (LAPPD) collaboration [38]. The goal of this project is to develop large area systems based on MCPs (with the size of up to 20 × 20 cm^2), for the measurement of time-of-arrival of relativistic particles with a time resolution of 10 ps, and for signals in positron emission tomography (PET). With its predicted time resolution of ~ 1 ps and a better acceptance of electrons, TiPC is performing better than MCP-based photodetectors.

Studies conducted within LAPPD report on the utilization of ALD MgO and Al_2O_3 films as coatings of inexpensive borosilicate MCPs [35]. The largest RSEY value (6.9) was obtained for 20 nm-thick MgO film, whereas the optimum thickness of Al_2O_3 was found to be 5 nm, with RSEY of 2.9 [32]. Apart from thickness, the study discusses the influence of surface composition on SEE performance. A strong dependence of emission on the electron dose was shown for both Al_2O_3 and MgO. However, a different trend is observed: while the deposition of carbon during the exposure to electron beam deteriorated the SEE of Al_2O_3, the RSEY of MgO increased. This might be related to the contribution of the surface carbon compound, which has RSEY greater than Al_2O_3, but lower than MgO. As a part of research within our group, too, ALD Al_2O_3 and MgO were characterized in terms of RSEY (results reported in [39] and in Chapters 4 and 5 of this thesis).

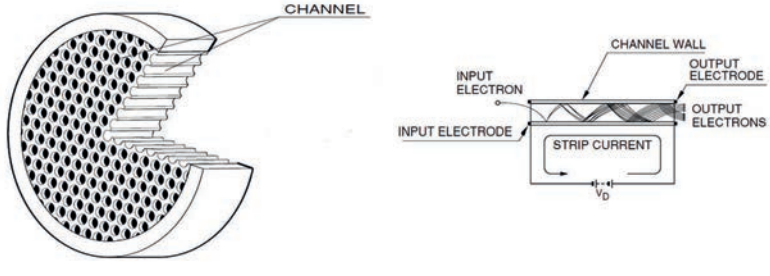

(a) (b)

Figure 2.5: Design (a) and a working principle (b) of an MCP photomultiplier. The MCP consists of a large number of slanted channels. Impinging electrons are multiplied at the inner walls of these channels, and then accelerated by voltage V_D applied across both ends of the MCP [2].

2.3. WORKING PRINCIPLE OF TIMED PHOTON COUNTER (TIPC) AND TYNODES

EVEN though the PMT is still widely used due to its efficiency, time resolution and low noise, the performance of the photomultiplier may be further improved by replacing the reflective dynodes with ones operating in the transmission mode. In this work, we explore the viability of various MEMS fabricated transmission dynodes (tynodes) for the electron multiplication in the novel timed photon counter (TiPC). With tynodes placed under the photocathode, TiPC would be an advanced type of a photodetector for soft photons, with wavelengths in the 0.1 – 10 µm range (corresponding to energies from 0.12

to 12 eV). Alternatively, capping the tynodes with an electron emission membrane ("e-brane"), will result in a Minimum Ionization Particle (MIP) tracking "Trixy" detector [40].

The tynode is essentially an array of free-standing membranes with thicknesses in the order of only a few nanometers. After the impact of an incoming electron on one side of the tynode, noise-free amplification is expected to be provided through SEE at the other ("emission") side of the membrane. Emission of electrons in transmission mode allows a significant reduction in size and weight of the device in comparison with existing photodetectors such as PMTs. In the envisioned design of TiPC, vertically stacked tynodes, put at different potentials in vacuum, will be placed on top of an all-digital sensing TimePix chip [41]. If our expectations are met, once it is realized, TiPC will provide an outstanding performance in terms of spatial and time resolution. The operating principle of the TiPC is presented in Figure 2.6.

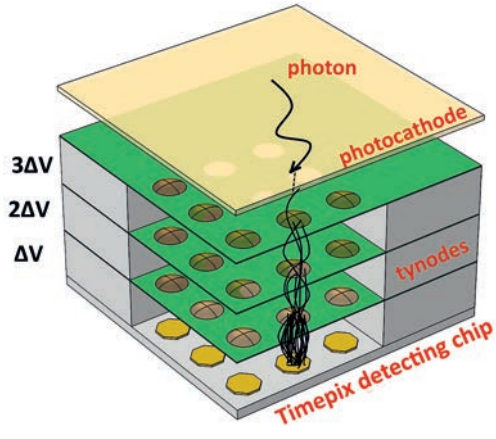

Figure 2.6: The operating principle of TiPC consists of three steps: 1. Conversion of a photon to an electron at the photocathode; 2. Electron multiplication provided by a stack of tynodes with thicknesses of only a few nm; 3. Signal detection through a pixel activation on the TimePix chip. Schematic drawing is not to scale.

The separation between tynodes is limited by the thickness of the supportive silicon frame. The minimal thickness of silicon wafers used for the fabrication of the tynodes in this work is 300 µm, but can be reduced by choosing a different substrate as a starting material. The separation is further increased by adding insulating spacers for the spark protection and the alignment of the tynodes (details on vertical stacking of the tynodes are given in Chapter 6). We predict that the crossing paths of electrons between tynodes will be effectively straight, with little variations, and the transit time two orders of magnitude smaller than in existing photomultipliers [42]. The rise time of a charge signal at the pixel input pad is determined by the crossing time of electrons over the gap between the last tynode and the TimePix chip. As a consequence, the ultimate time resolution of TiPC is expected to be in the order of a picosecond, though it eventually may be influenced by the delay of emission of secondary electrons after they are produced in the bulk of the tynode. Presumably, back-flow positive ions created in the process of elec-

tron multiplication [43] are blocked in the TiPC, so that no degradation of photocathode and tynodes take place.

With such design, TiPC would be a light, thin, flat and compact device, which can be used in a wide range of applications, including solid state, atomic and molecular physics experiments, medical imaging, and commercial applications such as 3D optical "flash" imaging. The motion of electrons in the TiPC is governed almost entirely by the electrostatic component, which allows the device operation in the presence of a strong magnetic field (prediction presented in the following paragraph).

To illustrate the working principle of TiPC and predict its operation when magnetic field is introduced, we used Comsol Multiphysics 5.3 software (Figure 2.7). 2D electron paths are computed by using the Charged Particle Tracing interface which can be found in Particle Tracing Module. This interface is mainly employed to trace ions and electrons under the influence of electric and magnetic forces [44]. Ten electrons at a time, with initial kinetic energy of 5 eV, are released from three geometrical entities which mimic photocathode in the envisioned TiPC design. Next, electrons strike the curved walls (i.e. tynodes), after which secondary electrons are emitted. Electrons are multiplied at five stages of tynodes, sealed in vacuum. The potential step between the tynodes is 200 V, center-to-center pitch and vertical distance between tynodes are 25 µm and 55 µm, respectively. The tynode is chosen to have a spherical-cap shape defined by radius of the sphere and height of the cap (30 and 4.7 µm, respectively). Unlike flat tynodes, here defined tynodes provide focusing of electrons (more details on this aspect will follow in Chapter 6). The tynodes do not trap electrons and have a TSEY of 3. On the other hand, all electrons "freeze" after they hit the outer boundary (i.e. the black box around the tynodes). In Figure 2.7a electron trajectories are simulated only in the presence of electric force specified by electric potential, whereas in Figure 2.7b a magnetic field of 1 T is added, perpendicular to the shown plane (up).

The total number of electrons released from the last tynode (closest to the detecting chip) is $TSEY^N$, where TSEY is the transmission secondary electron yield of a tynode material, and N the number of stacked tynodes. If the tynode material has a TSEY of 4, a stack of 4 tynodes provides a charge signal of 256 electrons, which is sufficient to drive the pixel circuitry of the TimePix-3 chip (a new generation of TimePix chip [45]). At the same time, the process of stacking that many tynodes would still not be too complex from the fabrication point of view. Previous studies have often put focus only on reflection configurations, which are of interest for applications such as PMTs, or, more recently, in LAPPD (as summarized in Section 2.2.1). There, a wide range of insulators was reported to have a high RSEY, which usually suggests efficient electron multiplication in transmission mode as well. However, in transmission mode, optimal electrical conductivity is required for replenishing vacancies in the membrane after the escape of secondary electrons. To avoid charging, the tynodes need to be covered by a very thin electrically conductive layer (see Section 2.5). The conductivity is of the utmost importance for the last tynode, which releases the largest number of electrons and governs the development of the charge signal induced on the pixel input by electrostatic influention of electrons crossing the gap towards the TimePix chip.

Another vital requirement relates to the mechanical and chemical properties of the selected tynode material. Low residual stress and chemical inertness to certain etchants used for the overall device fabrication are necessary, as the membrane material must be mechanically and chemically stable during and after the fabrication process. The details on the selection of a tynode material will be presented in following chapters. Furthermore, to improve the focusing of electrons, tynodes might be fabricated in semispherical shape. The focusing ability is especially critical for the first tynode, positioned closest to the photocathode. For the investigation of SEE flat tynodes have been employed, due to the more simple fabrication procedure. The method for producing curved tynodes will be reported in Chapter 6, together with simulation of electron trajectories in the stack of tynodes with different radii of curvature.

2.4. TRANSMISSION SECONDARY ELECTRON EMISSION (TSEE)

IF the dynode material is sufficiently thin (typically << 1 μm), secondary electron emission occurs not only at the incident surface, but on the back side (opposite of the irradiated side) of the film as well. To separate these two processes, a transmission secondary electron emission coefficient (TSEE) is introduced and defined as the ratio of the transmitted secondary current to the incident primary current. Transmitted current includes the contibution of sufficiently energetic forward-scattered electrons, and similarly to the SEE in reflection mode, we will use a term "transmission secondary electron yield" (TSEY) to refer to the maximum value of total TSEE. More details on currents generated upon the electron irradiation of tynodes is given in Chapter 3, together with the outlook of the TSEY measurement setup.

Transmission dynodes are fabricated by removing the substrate in a form of free standing films, obtained by removing the substrate from the area which is usually not larger than a few mm^2. Investigation of TSEE performance of a material is often conducted to assist RSEE analysis to determine the escape depth of electrons. In reflective configuration, SEs are emitted in all directions from the impact point. Therefore, they hit a successive dynode at a slanted angle of incidence and new SEs are created closer to the emitting surface, by which the escape probability is increased. In contrast to that, electrons impinge stacked tynodes perpendicularly and penetrate deeper into the material. Due to this, RSEY usually has higher values than TSEY. Moreover, since a portion of secondary electrons are emitted from the incident side of the transmission dynode, a proper functionalization (such as termination) of that surface should be conducted to reduce the losses. Likewise, an activation of the emitting (back) side is favoured for improving the TSEY.

At the same time, a difference in spatial distribution of reflected and transmitted SEs affects the complexity of these two types of electron multiplication devices. Namely, a reflective configuration requires more complicated geometry to direct electrons onto the next stage in a dynode array. For a device in transmission mode, multiplication stages can simply be stacked on top of each other, with a precision of alignment defined by the design of the tynodes.

Inevitably, escape of secondary electrons builds up a positive charge on the emitting surface of a dynode, normally being a high resistivity material. As a result, the local change of potential occurs, defined by the thickness of the emission material, its deielec-

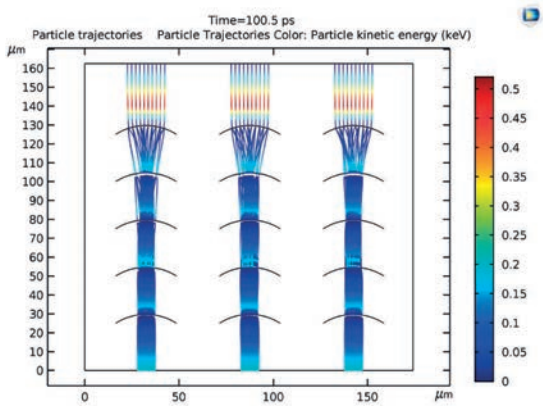

(a)

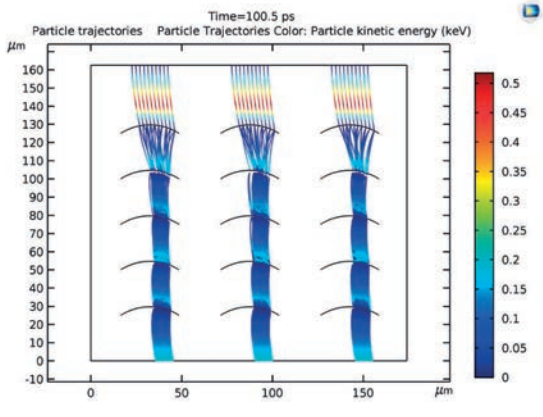

(b)

Figure 2.7: Simulated 2D trajectories of electrons, suggesting strong focusing effect originating from the curvature of tynodes with TSEY of 3. The potential step between tynodes is 200 V, center-to-center pitch and vertical distance between tynodes are 25 µm and 55 µm, respectively. The tynode is chosen to have a spherical-cap shape defined by radius of the sphere and height of the cap (30 and 4.7 µm, respectively) (a). Simulation with the same set of parameters performed in the presence of a magnetic field of 1 T perpendicular to the shown plane, up (b). Colour bars on the right represent the kinetic energy of electrons, in keV.

tric permittivity and electrical characteristics of the surrounding media. This increase of potential raises the electron affinity and reduces the SEY. Moreover, the vacancies in the dynode material represent the trapping spots for secondary electrons and disable their escape.

2.4.1. MATERIALS WITH HIGH TRANSMISSION SECONDARY ELECTRON YIELD (TSEY)

The use of transmission secondary electron emission for electron multiplication has been proposed much later than reflection configurations. The main reason for this was

the technological challenge in producing ultra-thin free standing films. The early transmission dynodes were developed to operate as multistage image intensifiers [46] [47]. Among the first studied materials for this application were alkali halides, such as KCl, which was deposited on top of a very thin scattering Au film and a supporting SiO layer [48]. The stopping metal improves the formation of secondary electrons and reduces the number of fast electrons which passes through the dynode. At the same time, it was demonstrated that decreasing the thicknesses of Au and KCl elevates the TSEY.

In Table 2.3 we summarize work on some efficient transmission dynode materials conducted by other groups, with the details on thicknesses of each film and energy corresponding to TSEY peaks. As indicated in [48], the optimal combination of 2 nm-thick Au and 60 nm of KCl provided a TSEY of 8. Unlike solid film KCl dynodes, a low-density KCl exhibited elevated TSEY of up to 37 with the applied extracting electric field (i.e. collecting voltage, denoted as V_C in Table 2.3)[49]. Similarly to the configuration with KCl, a CsI transmission dynode in a combination with Al_2O_3 as a substrate film and Al acting as conducting layer, was developed by Hamamatsu [50]. Two major advantages of this tynode were the reduced sensitivity to air exposure and the possibility to introduce NEA by Cs activation on the emission side of surface. Such termination almost doubled the TSEY from 15 to 27 for 70 nm-thick CsI film. Extremely high TSEY with value up to 112 were reported for self-supported GaAs membranes with Cs or Cs-O treated surfaces [51], and even more efficient multiplication was ascribed to Si [52]. NEA enabled by hydrogen termination made diamond an attractive choice as electron emitters in photomultipliers. Additionally, even better performance in terms of TSEY has been provided by doping of diamond with boron or nitrogen. Due to much longer diffusion lengths, single-crystal diamond proved to be a better amplifier film than polycrystalline diamond, displaying TSEY of 3 – 4 when a 20 keV incident beam was used [53] [54]. Nevertheless, a cardinal drawback of terminated diamond films is the degradation of NEA and the desorption of surface species throughout the ion and electron bombardment.

Up to now, the majority of well performing diamond free-standing membranes are of higher thicknesses, in the order of a few micrometers, which requires high energies of primary electrons. The main challenge in growth of ultra-thin diamond films is overcoming the poor seeding density which promotes non-continuity in a layer [57]. However, the fabrication of 150 nm-thick nanocrystalline, boron doped, CVD diamond film was demonstrated, with TSEY reaching a value of 5 [55]. Surprisingly, one of the pioneer investigation of transmission electron multiplication employed a MgO film with thickness down to 5 nm, deposited on top of an Al metallic support by vacuum distillation [56]. Combination of these two materials, together with surface activation by Cs, gave a TSEY of 5 at 3.5 keV and proved to be more stable in time than halides (analysed in the same work).

2.5. CHARGING OF INSULATORS

CHARGING of insulating materials under electron irradiation has a critical role in various fields. Processes of charging often obstruct interpretation, or even lead to a data loss in X-ray microanalysis and Auger electron spectroscopy [58], whereas in elec-

Transmission dynode material	Thickness	δ_m	E_m (keV)	Reference
SiO / Au / KCl (bulk)	SiO: 10 nm Au: (1.5 - 2.5) nm KCl: (30 – 60) nm	6 - 8	2.5 - 3.5	[48]
Al / KCl (porous)	Al: not specified KCl: (10 - 20) µm	2 - 42	6 - 7.5	[49]
Al_2O_3 / Al / CsI(Cs)	Al_2O_3: 60 nm Al: 20 nm CsI(Cs): 70 nm	27	9	[50]
GaAs (NEA applied, but not specified)	3.5 µm	112	20	[51]
Si (Cs-O)	(4 – 5) µm	725	20	[52]
polycrystalline CVD diamond (boron doped)	5 µm	2.4	35	[53]
single-crystal CVD diamond (treatments applied)	8.3 µm	0.9 – 3.4	20	[54]
nanocrystalline CVD diamond (boron doped)	150 nm 2.5 µm	5 3	7 18	[55]
Al / MgO	40 nm / 15 nm	5	3.5	[56]

Table 2.3: List of materials commonly used as transmission dynodes and their properties, where δ_m represents the maximum TSEY and E_m the matching energy of incident electrons. In case of combination of materials, the film providing electron multiplication is indicated as the last one (KCl and CsI), and was deposited on top of the supporting grid (SiO, Al_2O_3) and/or the scattering metal (Al, Au). If applied, surface termination of the emission side is specified in brackets (Cs and Cs-O). Selected literature reports cover the timeframe from 1950s until now.

tron microscopy cause defocusing and unstable imaging conditions [59]. In the design of spacecrafts, charging under cosmic radiation must be taken into consideration, as it is may lead to its failure through electrostatic discharges and electric arcs on components [60]. As discussed by Cazaux [61] [62], charged-up area consists of a positively and negatively charged layer, formed by escape of secondary electrons from the target and trapping of primary electrons, respectively. For convenience, SEY of non-charged material from Figure 2.4 is plotted again in Figure 2.8 (blue curve). Looking at it, we conclude that a sample is positively charged when the energy of the primary beam is between two crossover energies ($E_I < E_{PE} < E_{II}$), and the total number of electrons leaving the material is greater than the number of incoming electrons. Likewise, at energies $E_{PE} < E_I$ and $E_{PE} > E_{II}$, the total SEY is less than 1 and the sample is negatively charged.

Charging effects change the profile of the SEY curve as a function of primary energy (E_{PE}), by rapidly decreasing its values in the range of positive potential, and causing a slight increase at energies much higher than E_{II}. The distortion of SEY of a charged insulator is given in Figure 2.8 (green curve), from which is observed that the second

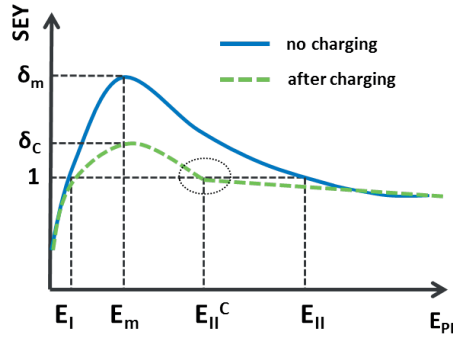

Figure 2.8: Typical trend of SEY of a non-charged insulator (blue curve) and after its charging (green curve).

crossover energy E_{II} is shifted to a lower value (E_{II}^{C}), forming a break in the slope of the curve (circular marker in Figure 2.8). The steady equilibrium state in a charged material is reached not only when the total $SEY^{C} = \delta^{C} = \delta_{SE}^{C} + \delta_{BSE}^{C} = 1$, (at primary energy $E_{PE} = E_{II}^{C}$), but also requires the additional condition that the surface potential (V_S) equals zero. This is fulfilled when the penetration range of PEs is nearly the same as the maximum escape depth of the SEs, and the recombination of generated electrons and holes is promoted. As an example, it is predicted by calculations that the second crossover energy for MgO films decreases to 1.1 – 1.7 keV from its initial value of 30 keV [63] [28]. However, even at the energy E_{II}^{C}, SEY can be affected by strong internal field near the surface (formed between two identically charged layers) and the leakage current flowing toward the grounded substrate. In addition, charging is governed by the density of trapping sites such as dislocations, atomic vacancies, impurities and contaminants on the material surface. It is difficult to determine these factors, and proposed theoretical models are often not in agreement with experimental results. Besides the abovementioned work of Cazaux, extensive discussion on the charging mechanism, including both analytical approaches and a set of measurement data is offered in references [64] [65]. More comments on how charging influences the SEY profile of particular materials investigated in this work will be given in the following chapters.

VERTICAL AND HORIZONTAL CONDUCTIVITY

Under the impact of primary electron beam, dielectric film exhibits so called “radiation induced conductivity” (RIC) in vertical direction, as discussed by Melchinger and Hofmann [66]. The electron-irradiated area has a higher electrical conductivity than non-irradiated parts of the film. RIC (γ) can be calculated by using the stopping law-relation:

$$\gamma = \gamma_0 D^{\Delta} = \gamma_0 \left(\frac{10^8 I_{PE} E_{PE}}{FR\rho} \right) \tag{2.3}$$

where I_{PE}, E_{PE} and F are the current, energy and spotsize of the primary electron beam (in A, keV and cm^2), respectively. R is the penetration depth of primary electrons (in cm), ρ the material density (in g/cm^3) and Δ is the material parameter. γ_0 represents the RIC at a reference dose rate (1 rad/s). The size of the RIC region is controlled

by the primary beam energy, and its efficiency in reducing charging up in dynodes is related to its distance from the conducting substrate. In tynodes (and sufficiently thin dynodes), the depth of the RIC volume is near to the film thickness, so that vertical conductivity is always contributing to the charge neutralization with maximum efficiency. For more efficient suppression of charging, it is necessary to provide a horizontal conductivity from the irradiated part of the SEE material towards the substrate. As a solution to this, the most common practice is coating the dynode/tynode by a conductive film, which is adopted in our study too.

2.5.1. STRATEGIES TO MINIMIZE CHARGING IN SEY MEASUREMENTS

One of the most common tactics to minimize the incident charge exposure and surface potential of the insulating target is the use of a low amplitude pulsed electron source. In the typical measurement configuration, time duration of a pulse is below 100 µs, and incident current is in the range 1 – 100 nA. Detailed summary of SEY studies on insulators and applied approaches to neutralize charging are given in reference [67]. As will be described in Section 3.3.7, the measurement setup for the evaluation of SEY in this work consists of a continuous electron beam inside a scanning electron microscope. It is important to point out that charging up is critical for the measurement of the SEY, but is of no concern in the operation of TiPC. Several strategies are used to control surface potentials are:

Deposition of a thin conductive film on top of insulating material. It is a common practice in scanning and transmission electron microscopy (SEM, TEM), as well as in energy dispersive X-ray detectors (EDX), to prepare samples on thin carbon films, or to add the conductive film such as carbon, gold, gold-palladium, tungsten, chromiuim etc., before the investigation in order to eliminate severe charging of the sample [68] [69]. This film should have small grains and a low thickness so it does not affect the surface morphology of the emission film. In the SEE investigation, the thickness of conductive films above tens of nanometers will "mask" the SEY of a target material, as demonstrated for copper layer applied on top of MgO in reference [70]. According to the work reported in [71], evaporation of a carbon film with a thickness of 10 nm or less on top of an almost 3 µm-thick insulator (mica foil) eliminated sample charge build-up. The most efficient techniques to deposit uniformly distributed coating are evaporation of metals, carbon evaporation and sputter coating [72]. Metal evaporation is a vacuum technique and produces relatively thin films with fine grains, but such sample preparation is often time consuming. Besides, high deposition temperature may damage the specimen. Carbon evaporation, on the other hand, is suitable for the samples without pronounced topographic features. Sputtering technique, on the other hand, can be conducted relatively fast and at low temperatures.

In case of emission in reflection mode, charge-up effects are limited due to the bulky metal substrate onto which the dynode material is deposited. For transmission dynode, on the other hand, the conductive film may be at a distance of half-width of the active membrane area, which is several orders of magnitudes larger than the dynode thickness. To overcome this disadvantage, a thin conductive layer should be placed on top at the incident side. This coating prevents the degradation of TSEY by inducing a

vertical leak of the positive charge, following an exponential decay with the time constant τ. At the same time, if thin enough, the coating should absorb a minimal energy portion of primary electrons and allow them to participate in the creation of secondary electrons. Even though this requirement makes metals a less convenient choice for such application, some research groups reported on the successful implementation of Al and Au films [49] [50] [46]. However, these transmission dynodes operate at high energies of a primary beam, in the order of a few keV, which is much above the desired operational energy range of the TiPC (TSEY peak at the primary energy in the range from 300 to 500 eV). In this work we applied sputtered TiN to provide the optimal lateral conductivity to materials subjected to SEE investigation.

Grounding the sample surface to compensate surface charge. It has been demonstrated that full charge compensation of an insulator can take from several hours up to months, depending on its resistivity and thickness [73] [74]. To facilitate the discharging through a leakage current, irradiated material should be connected to the conductive substrate. Consequently, tynode materials in this study were connected to silicon substrate by applying silver paint at the edge of samples.

Doping of the insulating material. Bulk conductivity in insulators can be acquired by introducing suitable type of dopants. By doing so, one affects the transport of secondary electrons, which then reflects on the SEE. For example, a drastic change of the SEY of diamond was demonstrated after the doping by boron or nitrogen was conducted [12] [75]. Also, MgO cermet films prepared by adding particles of Au, Ag and Ni exhibited enhanced SEY [76] [77], and so did a composite material MgO/Al_2O_3 [78]. On the ground of that, we made an attempt to provide sufficient conductivity to LPCVD SiN tynodes by increasing their Si content (see Chapter 3), and investigated the SEY of N-doped ultrananocrystalline diamond (UNCD), as will be reported in Chapter 6.

Sample heating. Heating can be applied as a technique to neutralize charge effect through de-trapping of charges accumulated on the insulating surface, or a deeply embedded charge. The temperature range required for this compensation depends on the band structure, dielectric constant and thermoelectrical properties of the insulator. A significant charge reduction is recorded for several insulators under a temperature increase up to 400 °C in reference [79]. SEY of a sample can been recorded at elevated temperatures, or upon the cooling down. Even though this strategy has been proved to be effective in charge replenishment, it is time consuming and can often lead to the decrease of the SEY caused by frequent phonon scattering [80] [81]. SEM used for the investigation of SEY in this work was not suitable for installing a heating stage. Consequently, we performed ex-situ thermal treatment on (MgO) tynodes (Chapter 5). Other methods to neutralize surface potentials include UV irradiation and flooding by ions and low-energy electrons. UV irradiation induces conductivity in some insulators, and is therefore effective in discharging negatively charged materials [82]. On the other hand, low-energy ($<$ 1 eV) electrons are efficient in removal of positive surface charges [83], but only under the condition that penetration depth of flooding electrons is very close to the depth at which targeted positive charge is distributed.

2.6. CONCLUSIONS

IN this chapter we use a photomultiplier tube (PMT) as an example to introduce the mechanism of photoelectric effect and reflective secondary electron emission, enabled by photocathodes and the dynode chains in PMTs, respectively. A short review of microchannel plates (MCPs) is given, as a technology which brought a significant reduction in size of PMTs and a better time resolution. Next, a design and operating method of a novel photodetector for single photons, TiPC, is presented and compared to existing photomultipliers. A main advantage of TiPC is a modified dynode (tynode), used as an example to demonstrate the SEE in transmission mode. Moreover, we listed here the most efficient materials for SEE in both configurations. Charging induced in isulators by electron irradiation is set out as one of the critical aspects in the SEY measurements. Following chapters will investigate applicability of different materials in the fabrication of tynodes.

REFERENCES

[1] C. Marmonier and C. Flyckt. Photomultiplier tubes: Principles and applications. *Photonis, September*, 2002.

[2] Photomultiplier tubes: Basics and applications. *Hamamatsu Photonics KK, Iwata City*, 2006.

[3] W.E. Spicer. Photoemissive, photoconductive, and optical absorption studies of alkali-antimony compounds. *Physical review*, 112(1):114, 1958.

[4] S. Donati and T. Tambosso. Single-photon detectors: From traditional PMT to solid-state SPAD-based technology. *IEEE Journal of Selected Topics in Quantum Electronics*, 20(6):204–211, 2014.

[5] N. Diaz, S. Casraneda, J.M. Ripalda, I. Montero, L. Galan, S. Feltham, D. Rabosa, and F. Rueda. Materials of low secondary electron emission to prevent the multipactor effect in high-power RF devices in space. In *6th Spacecraft Charging Technology*, pages 205–209, 1998.

[6] R.A. Kishek, Y.Y. Lau, L.K. Ang, A. Valfells, and R.M. Gilgenbach. Multipactor discharge on metals and dielectrics: Historical review and recent theories. *Physics of Plasmas*, 5(5):2120–2126, 1998.

[7] I. Montero, L. Aguilera, L. Olano, M.E. Dávila, V. Nistor, L. Galán, J.R. Dennison, and G. Wilson. Extremely low secondary electron emission from metal/dielectric particulate coatings. 2016.

[8] V.K. Zworykin, G.A. Morton, and L. Malter. The secondary emission multiplier-a new electronic device. *Proceedings of the Institute of Radio Engineers*, 24(3):351–375, 1936.

[9] Richard G. Carter. Crossed-field amplifiers. In *Microwave and RF Vacuum Electronic Power Sources*, The Cambridge RF and Microwave Engineering Series, pages 629—-658. Cambridge University Press, 2018.

[10] S.Y. Lai, A. Brown, J.C. Vickerman, and D. Briggs. The relationship between electron and ion induced secondary electron imaging: A review with new experimental observations. *Surface and interface analysis*, 8(3):93–111, 1986.

[11] R.A. Baragiola and P. Riccardi. Electron emission from surfaces induced by slow ions and atoms. In *Reactive Sputter Deposition*, pages 43–60. Springer, 2008.

[12] A. Shih, J. Yater, C. Hor, and R. Abrams. Secondary electron emission studies. *Applied surface science*, 111:251–258, 1997.

[13] S.W. McKnight and DiMarzio C.A. Materials considerations in photoemission detectors. https://slideplayer.com/slide/6286488/.

[14] https://physics.nist.gov/PhysRefData/Star/Text/ESTAR.html.

[15] K. I Grais and A.M. Bastawros. A study of secondary electron emission in insulators and semiconductors. *Journal of Applied Physics*, 53(7):5239–5242, 1982.

[16] H. Seiler. Secondary electron emission in the scanning electron microscope. *Journal of Applied Physics*, 54(11):R1–R18, 1983.

[17] C.G.H. Walker, M.M. El-Gomati, A.M.D. Assa'd, and M. Zadražil. The secondary electron emission yield for 24 solid elements excited by primary electrons in the range 250–5000 eV: a theory/experiment comparison. *Scanning*, 30(5):365–380, 2008.

[18] J.W. Gibson and R.E. Thomas. Secondary electron emission and conductivity mechanisms of epitaxial MgO films. *Applications of Surface Science*, 14(1):56–72, 1982.

[19] X. Meyza, D. Goeuriot, C. Guerret-Piécourt, D. Tréheux, and H-J. Fitting. Secondary electron emission and self-consistent charge transport and storage in bulk insulators: Application to alumina. *Journal of applied physics*, 94(8):5384–5392, 2003.

[20] H. Bruining. *Physics and applications of secondary electron emission.* McGraw-Hill, 1954.

[21] A.J. Dekker. Secondary electron emission. 6:251–311, 1958.

[22] J.L.H. Jonker. On the theory of secondary electron emission. *Philips Res. Rep.*, 7:1–20, 1952.

[23] R.G. Lye and A.J. Dekker. Theory of secondary emission. *Physical Review*, 107(4):977, 1957.

[24] G.F. Dionne. Origin of secondary-electron-emission yield-curve parameters. *Journal of Applied Physics*, 46(8):3347–3351, 1975.

[25] Y. Lin and D.C. Joy. A new examination of secondary electron yield data. *Surface and Interface Analysis: An International Journal devoted to the development and application of techniques for the analysis of surfaces, interfaces and thin films*, 37(11):895–900, 2005.

[26] J.E. Burke. Lucalox alumina: The ceramic that revolutionized outdoor lighting. *MRS Bulletin*, 21(6):61–68, 1996.

[27] P.H. Dawson. Secondary electron emission yields of some ceramics. *Journal of Applied Physics*, 37(9):3644–3645, 1966.

[28] N.R. Whetten and A.B. Laponsky. Secondary electron emission of single crystals of MgO. *Journal of Applied Physics*, 28(4):515–516, 1957.

[29] Y. Ushio, T. Banno, N. Matuda, Y. Saito, S. Baba, and A. Kinbara. Secondary electron emission studies on MgO films. *Thin Solid Films*, 167(1-2):299–308, 1988.

[30] J.E. Yater and A. Shih. Secondary electron emission characteristics of single-crystal and polycrystalline diamond. *Journal of Applied Physics*, 87(11):8103–8112, 2000.

[31] R. Vaz, P.W. May, N.A. Fox, C.J. Harwood, V. Chatterjee, J.A. Smith, C.J. Horsfield, J.S. Lapington, and S. Osbourne. Measurement of the secondary electron emission from CVD diamond films using phosphor screen detectors. *Journal of Instrumentation*, 10(03):P03004, 2015.

[32] S.J. Jokela, I.V. Veryovkin, A.V. Zinovev, J.W. Elam, A.U. Mane, Q. Peng, Z. Insepov, and et. al. Secondary electron yield of emissive materials for large-area micro-channel plate detectors: surface composition and film thickness dependencies. *Physics Procedia*, 37:740–747, 2012.

[33] J.L. Wiza and et. al. Microchannel plate detectors. *Nucl. Instrum. Methods*, 162(1-3):587–601, 1979.

[34] H. Kume, K. Koyama, K. Nakatsugawa, S. Suzuki, and D. Fatlowitz. Ultrafast microchannel plate photomultipliers. *Applied optics*, 27(6):1170–1178, 1988.

[35] T. Gys. Micro-channel plates and vacuum detectors. *Nuclear Instruments and Methods in Physics Research Section A: Accelerators, Spectrometers, Detectors and Associated Equipment*, 787:254–260, 2015.

[36] A. Lehmann, A. Britting, W. Eyrich, M. Pfaffinger, F. Uhlig, A. Belias, R. Dzhygadlo, A. Gerhardt, K. Götzen, G. Kalicy, and et. al. Tremendously increased lifetime of MCP-PMTs. *Nuclear Instruments and Methods in Physics Research Section A: Accelerators, Spectrometers, Detectors and Associated Equipment*, 845:570–574, 2017.

[37] https://www.photonis.com/product/planacon%E2%84%A2-photodetector.

[38] H.J. Frisch and et. al. A brief technical history of the large-area picosecond photodetector (LAPPD) collaboration, 2016.

[39] H. van der Graaf, H. Akhtar, N. Budko, H.W. Chan, C.W. Hagen, C.C.T. Hansson, G. Nützel, S.D. Pinto, V. Prodanović, B. Raftari, and et. al. The tynode: A new vacuum electron multiplier. *Nuclear Instruments and Methods in Physics Research Section A: Accelerators, Spectrometers, Detectors and Associated Equipment*, 847:148–161, 2017.

[40] H. van der Graaf, M. Bakker, H.W. Chan, E. Charbon, F. Santagata, P.M. Sarro, and D. Schaart. The Tipsy single soft photon detector and the Trixy ultrafast tracking detector. In *2012 IEEE Nuclear Science Symposium and Medical Imaging Conference Record (NSS/MIC)*, pages 1952–1956. IEEE, 2012.

[41] X. Llopart, R. Ballabriga, M. Campbell, L. Tlustos, and W. Wong. TimePix, a 65k programmable pixel readout chip for arrival time, energy and/or photon counting measurements. *Nuclear Instruments and Methods in Physics Research Section A: Accelerators, Spectrometers, Detectors and Associated Equipment*, 581(1-2):485–494, 2007.

[42] R.H. Hadfield. Single-photon detectors for optical quantum information applications. *Nature photonics*, 3(12):696, 2009.

[43] N.R. Rajopadhye, V.A. Joglekar, V.N. Bhoraskar, and S.V. Bhoraskar. Ion secondary electron emission from Al_2O_3 and MgO films. *Solid state communications*, 60(8):675–679, 1986.

[44] Comsol. Introduction to particle tracing module. https://doc.comsol.com/5.4/doc/com.comsol.help.particle/IntroductionToParticleTracingModule.pdf.

[45] https://medipix.web.cern.ch/technology-chip/timepix3-chip.

[46] M.M. Wachtel, D.D. Doughty, G. Goetze, A.E. Anderson, and E.J. Sternglass. Image intensification by transmission secondary electron emission. *Review of Scientific Instruments*, 31(5):576–578, 1960.

[47] A.E. Anderson. The transmission secondary emission image intensifier and its application to low light level imaging. *IRE Transactions on Nuclear Science*, 7(2-3):133–136, 1960.

[48] E.J. Sternglass. High-speed electron multiplication by transmission secondary electron emission. *Review of Scientific Instruments*, 26(12):1202–1202, 1955.

[49] E.J. Sternglass and G.W. Goetze. Field-enhanced transmission secondary emission for high-speed counting. *IRE Transactions on Nuclear Science*, 9(3):97–102, 1962.

[50] M. Hagino, S. Yoshizaki, M. Kinoshita, and R. Nishida. Caesium activated CsI transmission-type secondary emission dynode. In *Advances in electronics and electron physics*, volume 33, pages 469–482. Elsevier, 1972.

[51] R.U. Martinelli, M.L. Schultz, and H.F. Gossenberger. Reflection and transmission secondary emission from GaAs. *Journal of Applied Physics*, 43(11):4803–4804, 1972.

[52] R.U. Martinelli. Reflection and transmission secondary emission from silicon. *Applied Physics Letters*, 17(8):313–314, 1970.

[53] V.V. Dvorkin, N.N. Dzbanovsky, N.V. Suetin, E.A. Poltoratsky, G.S. Rychkov, E.A. Il'Ichev, and S.A. Gavrilov. Secondary electron emission from CVD diamond films. *Diamond and related materials*, 12(12):2208–2218, 2003.

[54] J.E. Yater, J.L. Shaw, K.L. Jensen, T. Feygelson, R.E. Myers, B.B. Pate, and J.E. Butler. Secondary electron amplification using single-crystal CVD diamond film. *Diamond and Related Materials*, 20(5-6):798–802, 2011.

[55] J.E. Yater, A. Shih, J.E. Butler, and P.E. Pehrsson. Transmission of low-energy electrons in boron-doped nanocrystalline diamond films. *Journal of applied physics*, 93(5):3082–3089, 2003.

[56] H. Dormont and P. Saget. Émission secondaire par transmission. *Journal de Physique Appliquée*, 20(S4):23–28, 1959.

[57] R.M.A. Vaz. *Studies of the secondary electron emission from diamond films*. PhD thesis, University of Bristol, 2013.

[58] H. Guo, W. Maus-Friedrichs, and V. Kempter. Charging phenomena and charge compensation in AES on metal oxides and silica. *Surface and Interface Analysis: An International Journal devoted to the development and application of techniques for the analysis of surfaces, interfaces and thin films*, 25(6):390–396, 1997.

[59] D.C. Joy. Control of charging in low-voltage SEM. *Scanning*, 11(1):1–4, 1989.

[60] S.C. JR Dennison and C. Thomson. Importance of accurate computation of secondary electron emission for modeling spacecraft charging. In *Proceedings of the 9th Spacecraft Charging Technology Conference,(EPOCHAL TSUKUBA, 2005)*.

[61] J. Cazaux. Some considerations on the secondary electron emission, δ, from e- irradiated insulators. *Journal of applied physics*, 85(2):1137–1147, 1999.

[62] J. Cazaux. Electron-induced secondary electron emission yield of insulators and charging effects. *Nuclear Instruments and Methods in Physics Research Section B: Beam Interactions with Materials and Atoms*, 244(2):307–322, 2006.

[63] J.B. Johnson and K.G. McKay. Secondary electron emission of crystalline MgO. *Physical Review*, 91(3):582, 1953.

[64] A.V. Gostev, E.N. Evstaf'eva, E.I. Rau, A.M. Tagachenkov, and A.A. Tatarintsev. Characteristics of dielectric film charging, depending on their thickness upon electron irradiation. *Bulletin of the Russian Academy of Sciences: Physics*, 78(9):833–838, 2014.

[65] E.I. Rau, E.N. Evstaf'eva, and M.V. Andrianov. Mechanisms of charging of insulators under irradiation with medium-energy electron beams. *Physics of the Solid State*, 50(4):621–630, 2008.

[66] A. Melchinger and S. Hofmann. Dynamic double layer model: Description of time dependent charging phenomena in insulators under electron beam irradiation. *Journal of applied physics*, 78(10):6224–6232, 1995.

[67] C.D. Thomson. *Measurements of the secondary electron emission properties of insulators*. PhD thesis, Utah State University, 2005.

[68] R.M. Glaeser and K.H. Downing. Specimen charging on thin films with one conducting layer: Discussion of physical principles. *Microscopy and Microanalysis*, 10(6):790–796, 2004.

[69] V. Der Want. A comparative study of thin coatings of au/pd, pt and cr produced by magnetron sputtering for FE-SEM. *Journal of microscopy*, 189(1):79–89, 1998.

[70] P.J. Møller and J-W. He. Electron beam induced charging of Cu/MgO surfaces. *Nuclear Instruments and Methods in Physics Research Section B: Beam Interactions with Materials and Atoms*, 17(2):137–140, 1986.

[71] O. Hideo, K. Yoshinobu, and K. Koichi. Carbon-coated film method PIXE for thick and insulating samples. *Nuclear Instruments and Methods in Physics Research Section B: Beam Interactions with Materials and Atoms*, 75(1-4):140–143, 1993.

[72] A. Ul-Hamid. *A Beginners' Guide to Scanning Electron Microscopy*. Springer, 2018.

[73] A.R. Frederickson and J.R. Dennison. Measurement of conductivity and charge storage in insulators related to spacecraft charging. *IEEE Transactions on Nuclear Science*, 50(6):2284–2291, 2003.

[74] Prasanna V Swaminathan. Measurement of charge storage decay time and resistivity of spacecraft insulators. 2004.

[75] K.L. Jensen, J.L. Shaw, J.E. Yater, and B.B. Pate. Enhancing secondary yield of a diamond amplifier using a nitrogen layer. *Journal of Applied Physics*, 117(21):214501, 2015.

[76] J.C.C. Fan and V.E. Henrich. Preparation and properties of sputtered MgO/Au, MgO/Ag, and MgO/Ni cermet films. *Journal of Applied Physics*, 45(9):3742–3748, 1974.

[77] J. Li, W. Hu, K. Wang, B. Gao, Y. Li, S. Wu, J. Zhang, and H. Fan. Au doping effect on the secondary electron emission performance of MgO films. *Materials*, 11(11):2104, 2018.

[78] F. Wang, F. Zhou, J. Wang, W. Liu, Q. Zhang, and Q. Yin. Characterization of MgO/Al_2O_3 composite film prepared by DC magnetron sputtering and its secondary electron emission properties. *Journal of Electronic Materials*, 47:4116–4123, 2018.

[79] L. Wang, Y. Ji, B. Wei, Y. Zhang, J. Fu, X. Xu, and X. Han. Charge compensation by in-situ heating for insulating ceramics in scanning electron microscope. *Ultramicroscopy*, 109(11):1326–1332, 2009.

[80] Y. Yamano, S. Kobayashi, S. Michizono, Y. Saito, and et. al. Secondary electron emission and surface charging evaluation of alumina ceramics and sapphire. *IEEE Transactions on Dielectrics and Electrical Insulation*, 13(1):72–78, 2006.

[81] M.I. Khan, S.D. Lubner, D.F. Ogletree, and C. Dames. Temperature dependence of secondary electron emission: A new route to nanoscale temperature measurement using scanning electron microscopy. *Journal of Applied Physics*, 124(19):195104, 2018.

[82] A.D. Bass, P. Cloutier, and L. Sanche. Measurements of charge accumulation induced by monochromatic low-energy electrons at the surface of insulating samples. *Journal of applied physics*, 84(5):2740–2748, 1998.

[83] S. Ichimura, H.E. Bauer, H. Seiler, and S. Hofmann. Reduction of charging in surface analysis of insulating materials by AES. *Surface and interface analysis*, 14(5):250–256, 1989.

3

Low Pressure Chemical Vapour Deposited Silicon Nitride Tynodes

In this chapter we introduce LPCVD SiN as the first material utilized in the microfabrication of the tynodes. In Section 3.1 we describe LPCVD as the deposition method put to use in this study. An overview and working principles of different investigation methods of material properties is set out in Section 3.2. The next section presents a detailed characterization of structural, mechanical and chemical properties of the SiN films with different thicknesses, and deposited with varying process conditions, namely, gass flow ratios. Furthermore, the performance of the tynodes is investigated in terms of secondary electron emission, a fundamental attribute that determines their applicability in TiPC.

Parts of this Chapter have been published in: "Ultra-thin alumina and silicon nitride MEMS fabricated membranes for the electron multiplication", *Nanotechnology*, 29(15):155703, 2018.

3.1. LPCVD SiN

SILICON nitride thin films have a wide number of applications in the semiconductor industry. They are used as diffusion barriers against mobile ions and moisture, as passivation layers, gate dielectrics, masks for selective oxidation of silicon, etch stop layers, and for chemical mechanical polishing (CMP) processes [1]. Mechanical and physical properties of SiN layers have been a subject of many studies, especially for the suitability of this material in load-bearing MEMS applications. Due to their mechanical strength and resistance to common etching chemicals in MEMS, such as pottasium hydroxide (KOH) and, to a less extent, to hydrofluoric acid (HF), SiN films became a very popular choice in the production of large-area thin membranes. Thin SiN membranes have been used as a support layer for devices with various functionalities, such as polysilicon microactuators [2] and a piezoelectric microspeaker [3]. Some other applications and characterization of SiN membranes can be found in references [4] [5] [6]. On account of its ability to provide robust free-standing films with thicknesses down to tens of nm, LPCVD SiN was the first candidate in the tynode fabrication where large arrays of membranes are needed for the electron multiplication in the TiPC, and the initial material we characterized in terms of SEE.

Thin films of SiN can be deposited using various techniques: atmospheric pressure chemical vapour deposition (APCVD), plasma enhanced chemical vapour deposition (PECVD) and low pressure chemical vapour deposition (LPCVD), with the latter two methods being the most extensively employed ones. Growth temperature of PECVD SiN can be below 400 °C [7], whereas the deposition temperature of LPCVD process usually exceeds 700 °C. However, the etch resistance and the step coverage of SiN obtained by LPCVD are surpassing the properties of its PECVD counterpart [8]. Recently, atomic layer deposition (ALD) enabled the deposition of highly conformal SiN layers at temperatures below 550 °C [9] [10] [11].

Chemical vapour deposition (CVD) is defined as a technique to grow a solid film or powder on a surface by dissociation and/or chemical reactants in an environment activated by heat, light or plasma [12]. A CVD process starts with the introduction of reactant gasses into a reaction chamber and the transport of these species by gas-phase diffusion to the wafer surface. The reactants are then adsorbed on the substrate surface, becoming adatoms. This is followed by migration of adatoms to the growth sites where so called heterogeneous reactions for forming solid film and gaseous by-products take place. Alternatively, homogeneous reactions may happen in the gas phase even before the reactants reach the substrate surface. The latter, however, may result with formation of solid clusters which reduce the film quality and cause adhesion problems. Finally, by-products diffuse towards the boundary layer and, after desorption from the surface, they are removed from the reaction chamber. General requirements CVD process should meet are reasonably short deposition time, high throughput and a low temperature which does not affect other films already applied onto the substrates (such as metals with low melting points). In addition, it is also crucial to avoid incorporation of by-products in the growing layer, as this would deteriorate its purity.

LPCVD provides films with better uniformity and step coverage than CVD at atmospheric pressures. This technique is employed for the growth of a variety of films, including Si_3N_4, poly-Si, SiO_2 and (boro)phosphorsilicate glass. Due to the reduced pressure, the diffusivity of the reactant gasses is boosted to an extent where the growth process is no longer driven by mass transfer of reactant species. Instead, film deposition manifests in the reaction-rate limited regime and depends greatly on temperature. Such mechanism enables uniform deposition of large batches of wafers. The rate of gas-phase reactions is significantly decreased at low pressure, thus the risk of particulate contamination is minimized too. Two major limitations of LPCVD method are the relatively high operating temperature and the slow growth rate, when compared to PECVD technique. An attempt to speed up the deposition process by increasing partial pressures of reactants results in the enhancement of gas-phase reactions. Decrease of temperature, on the other hand, causes a very slow deposition rate. For further reading on the mechanism and a model for thin film growth in LPCVD, reference [13] is recommended.

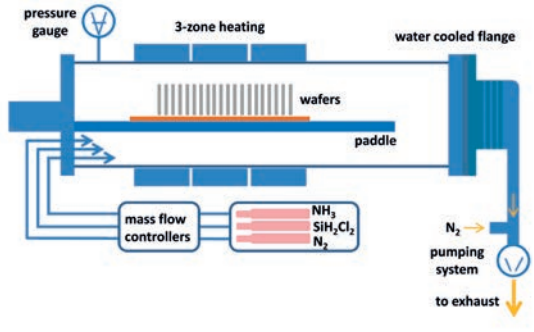

Figure 3.1: Schematic diagram of the reactor and main elements in the LPCVD system used for the SiN films deposition [14].

One of the most common configurations of a LPCVD reactor is a horizontal hot wall tube. This solution provides good uniformity and high throughput. Layers subjected to this study were deposited in a Tempress Systems reactor. The most common gas mixture for SiN LPCVD process consists of dichlorosilane (DCS, SiH_2Cl_2) and ammonia (NH_3) as it provides a very good uniformity of thickness and composition. The use of silane (SiH_4) as silicon source is a less preferred choice, due to the exhaustion phenomena of the chemical species participating in the deposition which causes large non-uniformity in the material properties over the load [15]. The amount of gasses is being managed by mass flow controllers, whereas the vacuum pump connected to the backside of the tube tunes the pressure. For the given tube design, the maximum allowed amount of gasses flowing is 500 sccm, as suggested by the manufacturer. However, to allow the film growth at a safe margin from this maximum value, the total gas flow in this work was set to 400 sccm. Wafers are positioned in quartz boats, perpendicular to the direction of the main gas flow, and with a spacing of 10 mm. In this way, the system facilitates processing of large batches of wafers at once. The paddle with loaded wafers moves automatically in, at the speed of 200 mm/min, which allows wafers to gradually adjust to the starting

temperature of 700 °C inside the tube. To reach the set deposition temperature (generally 850 °C) , the temperature of three different zones was set to 840, 846 and 865 °C. The precursor gasses employed were dichlorosilane (DCS, SiH_2Cl_2) and ammonia (NH_3), the latter diluted in 5% H_2. Ultra-pure nitrogen (N_2) from a liquid nitrogen source was used as the purging gas.

3.2. SiN TYNODES

In this section the design of the SiN tynodes is given, as well as the function of its key elements: membranes, supporting grid and conductive film. This is followed by the detailed MEMS fabrication flowchart of the SiN tynodes, where each component of the tynode is annotated a specific material, thickness and deposition method.

3.2.1. LAYOUT OF THE TYNODES

On each 4-inch wafer 12 tynode chips are produced, each with a size of 2×2 cm^2. Tynodes are designed as $n \times n$ large arrays, where n is the number of a single membrane and was chosen to be 64 or 128 (to allow potential tiling of tynodes and put to use the entire pixelized area of the TimePix chip). Diameter of each membrane (d) was 10, 20 or 30 µm, with a constant center-to-center pitch (a) of 55 µm chosen to match the distance between pixel pads on a detecting TimePix chip, as illustrated in Figure 3.2. Increase of the diameter of individual membrane enlarges the active area of the tynode and reduces the chance of electrons to be absorbed in a thick supporting mesh. Several sizes of membranes are included in the design of the tynodes with the aim to determine the maximum diameter for which the entire array is still mechanically stable and the largest number of membranes remains intact. Over one wafer, yield observed on 8 chips containing 40 nm-thick tynodes in 64×64 arrays was higher around 99%. In the fabrication of SiN tynodes, two films with different Si level are employed, namely "Type 1" and "Type 2" (see Table 3.1). Tynode films are produced in two different thicknesses: 25 and 40 nm, so that four different sets of the tynodes are later subjected to the SEY characterization. Apart from these two layers, a third film, named "Type 3", has also been deposited and subjected to some characterization (to obtain information on its stress, optical properties and morphology). However, it has not been employed in the fabrication of the tynodes, since already "Type 1" and "Type 2" had only negligible differences in their SEE performance (as will be reported in Section 3.4.6). Tuning of composition gasses has been conducted as an effort to reduce the specific resistivity of SiN and charging up which occurs in the SEE measurements.

3.2.2. FABRICATION PROCESS

In this section we introduce the process developed for the fabrication of tynodes using (LPCVD) SiN, schematically depicted in Figure 3.3. Employed substrates are single side polished 4-inch (100), phosphorus doped (5 – 10 Ω cm) wafers with thicknesses of 525 ± 15 µm. Prior to the processing, the wafers are subjected to a standard cleaning procedure including 10 min long dip in 99% ("fuming") and 69.5% ("boiling") HNO_3, each

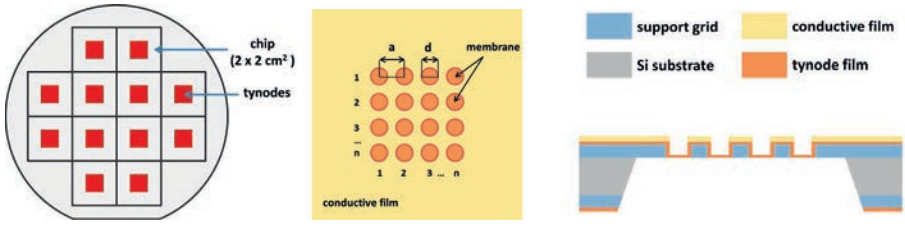

(a) (b) (c)

Figure 3.2: Layout of a wafer containing chips with tynodes. Top view (b) and cross section (c) of the tynode chip with color legend defining main elements in the tynode design. Parameters a, d and n stand for the center-to-center distance between membranes, diameter of a membrane and number of membranes in the array, respectively.

followed by rinsing in de-ionized H_2O. After that, the Si substrate is oxidized in a wet thermal environment at 1100 °C, for a resulting oxide thickness of 500 nm. Moving further, a 500 nm-thick optimized low-stress LPCVD silicon nitride layer ("Type 1" in Table 3.1) is deposited to serve as a support material in which tynodes are suspended (Figure 3.3a). This film is then patterned on the front side of the wafers, using hexafluoroethane (C_2F_6) etching chemistry to form the tynode grid. The thin oxide film left after the dry etching step is subsequently removed in a 0.5% HF solution. This is performed as a precaution step to ensure that the tynode material is deposited on a smoothened surface without sharp corners. In the following step, the SiN films with different Si levels ("Type 1, 2 and 3") were deposited ((Figure 3.3b)) using the reactor described in the Section 3.1 .

In this study, we conducted characterization of 3 different types of SiN films with the goal to develop the layer with sufficiently low resistivity. The Si content in the films was increased by setting DCS/ammonia mixture ratio to 5.67 ("Type 1" SiN film), 9 ("Type 2" SiN film) and 10.43 ("Type 3" SiN film), while the total gas flow was kept constant. The process parameters in the LPCVD of SiN films are given in Table 3.1.

Next, large windows on the back side of wafers are etched (Figure 3.3c). As a conductive film in between membranes, we used 100 nm thin evaporated gold (on 10 nm of Cr, for improved adhesion) patterned by a lift-off technique (Figure 3.3)d). Then, the wafers were mechanically sawed into chips, in order to avoid dicing after the fragile tynodes are formed. Etching of Si substrate was attained by 33% KOH continuously stirred solution, at the temperature of 85 °C. Both SiN and Au are inert to the employed etchant and for this reason no protective vacuum holder is required for the final release of the membranes (Figure 3.3e). A wash in 5% HCl solution followed by a dip in 99% HNO3, each 15 min long, proved to be efficient in the final cleaning procedure of samples. Finally, samples were rinsed by a gentle flow of de-ionized (DI) water and dried in air. SEM image of one fabricated tynode is shown in Figure 3.4.

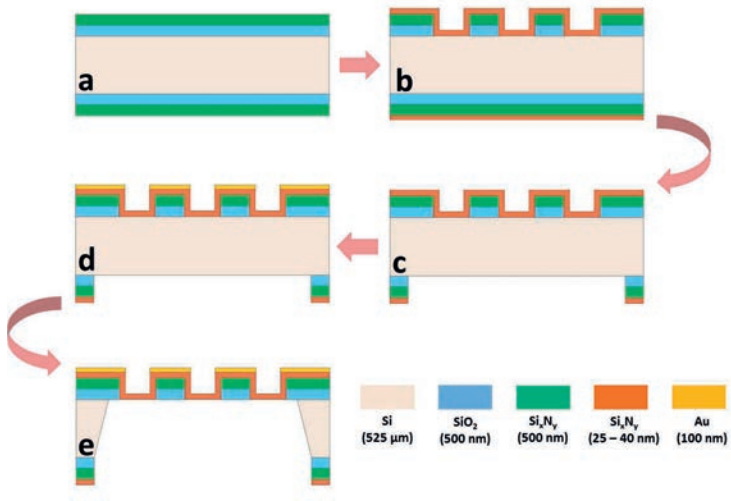

Figure 3.3: MEMS fabrication flowchart of the SiN tynodes: thermal oxidation and deposition of thick SiN grid (a); Patterned SiO_2-SiN structures are coated by a thin SiN tynode film (b); Opening of the large window on the backside of the wafer (c); Evaporation and patterning of Au conductive mesh (d) and a final release of the tynodes (e).

SiN film	SiH_2Cl_2 (sccm)	NH_3 (sccm)	SiH_2Cl_2/NH_3	Temperature (°C)	Pressure (mTorr)
"Type 1"	340	60	5.67	850	150
"Type 2"	360	40	9.00	850	150
"Type 3"	365	35	10.43	850	150

Table 3.1: Process parameters in the LPCVD of investigated SiN films.

3.3. TOOLS FOR THE MATERIAL CHARACTERIZATION

THE SiN films are subjected to the characterization in order to determine the most relevant mechanical, structural and electrical properties of interest for the TiPC application. Here we describe the basic principle of each employed measurement method, with a more extensive description of Dual Faraday Cup, the setup used for the evaluation of SEE. Stresses of films used as the tynode materials are evaluated by measuring the curvature of wafer. The stress level in films, among others, affects the potential of a material to provide, as required here, very thin, large and flat free standing films. In order to perform the accurate thickness acquisition of the tynode, as an attribute which has a great impact on the SEE of a film, we use spectroscopic ellipsometry. Additionally, grain boundaries and roughness of a film have impact on its electron emission properties [16]. Imaging and quantitative characterization of the surface morphology of the layers is achieved by using atomic force microscopy (AFM). Crystallinity of a film plays an important role in the emission of secondary electrons too: crystals are known to exhibit higher SEY than amorphous materials [17]. Atomic structure of the films is determined by using X-ray diffraction. X-ray photoelectron spectroscopy (XPS) is conducted in or-

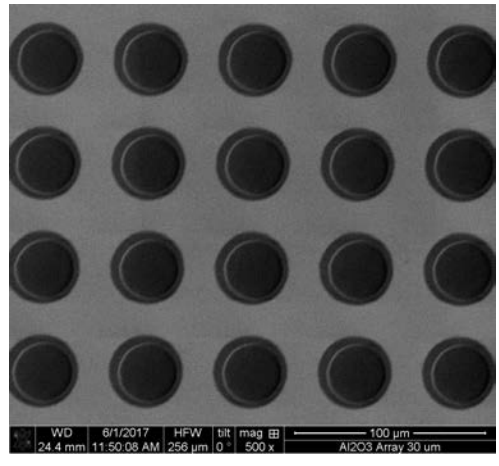

Figure 3.4: SEM image of a 25 nm-thick SiN tynode with a diameter of 30 µm, produced by using "Type 2" film.

der to evaluate the chemical composition of the tynode materials. In the development of a tynode material with less pronounced dielectric properties, a novel gaseous detector with Micromegas is put to use in the resistivity measurements. Finally, inquiry into the pivotal attribute of the tynode material, its SEY, is enabled by a dedicated Dual Faraday Cup (DFC) setup.

3.3.1. WAFER CURVATURE METHOD

Stress in solid materials is caused by displacement of its atoms from the equilibrium states when an external force is applied. Stress may be compressive or tensile, depending on the type of substrate bending caused by the presence of the film (Figure 3.5). Compressive stress induces convex bending of the substrate, i.e. film tends to expand parallel to the substrate surface. Exceeding compressive stress may lead to buckling of the film. Tensile stress leads to concave bending of the substrate and contraction of the film parallel to the substrate surface. Films that exhibit high tensile stress are, on the other hand, prone to cracking. Consequently, high stress is an undesirable property in the microfabrication as it causes unwanted deflection of microstructures, thus negatively affecting the performance of MEMS devices. For many applications, stress-free or stress compensated films are therefore required. According to the convention used, a positive curvature implies a concave shape with the wafer oriented with the film on top, and negative curvature means a convex shape with the same wafer and film orientation. A positive stress is tensile and a negative stress is compressive.

The total stress in the deposited film can be expressed as:

$$\sigma = \sigma_i + \sigma_{th} \tag{3.1}$$

where σ_i is intrinsic (microstructural) stress and originates from the growth mechanism and effects such as lattice mismatch, crystallization, incorporation of foreign atoms, microscopic voids, etc. Thermal stress (σ_{th}) occurs due to the different coefficient of

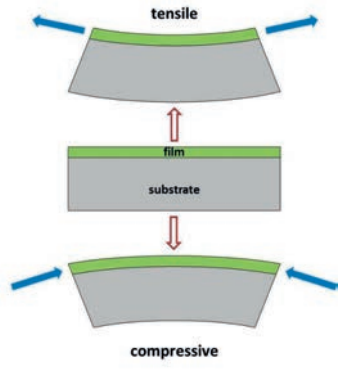

Figure 3.5: Influence of stress in a thin film on the substrate curvature: compressive stress causes a convex deflection, whereas tensile stress leads to a concave deflection.

thermal expansion between the film and substrate. The total stress can be modified by post-processing steps such as ion implantation and thermal annealing of the film. Optionally, bow of the substrate induced by stress in the film can be compensated by adding one or multiple different layers with certain thicknesses and stress [18]. Intrinsic stress of a film can be controlled by tuning the deposition parameters such as flow rate, ambient pressure, ratio of reaction gases, deposition temperature as well as the conditions of the substrate surface. Hence, by an appropriate setting of the above parameters it is possible to tune it, though the impact of films structure on the stress level is not yet fully fathomed. More details on the origin of stress and failure modes it causes in thin films can be found in [19] [20].

The wafer curvature test has emerged as a popular technique for the evaluation of residual stresses in continuous films deposited on thick substrates. As mentioned previously, a film under stress causes bending of the substrate, which allows a precise quantification of stress through measuring the wafer curvature (Figure 3.6). The deflection of a wafer is evaluated by laser scanning. The bow of the wafer is calculated from the angle of the deflected beam, which is then used for approximation of the radius of curvature. For small deformations, and when the film thickness (d_f) is much smaller than the thickness of the substrate (d_s), the magnitude of the residual stress in the film is given by the Stoney formula [21]:

$$\sigma = \frac{E_s}{6(1-\nu_s)} \frac{d_s}{d_f} \left(\frac{1}{R} - \frac{1}{R_0}\right) \tag{3.2}$$

where Young's modulus (E_s) and Poisson's ratio (ν_s) characterize the elastic behaviour of the substrate material. R_0 represents the initial radius of curvature of the wafer, whereas R is the radius after film deposition.

The wafer curvature measurements in this work are conducted with a Tencor FLX-2908, equipped with two lasers operating at 630 and 780 nm. At first, the bow of wafers is measured prior to the deposition. Then, surface profiling of bowed wafers which have

deposited or grown thin films on the front side is performed after completely stripping the back side. Scanning is performed through the centre of wafers in the direction parallel to the main flat, 1 cm away from the edges. In order to increase the precision of the stress evaluation, multiple measurements are performed usually 4 – 5 subsequent scanning cycles, each around 20 s long. These values are then averaged in order to calculate the final stress.

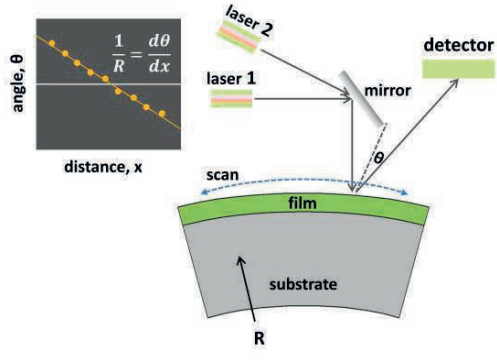

Figure 3.6: The principle of the wafer curvature measurement: a laser beam is directed onto the surface at a known angle, after which the reflected signal is detected by a position sensitive photodiode. Adapted from [22].

3.3.2. SPECTROSCOPIC ELLIPSOMETRY

The thickness and optical properties of the tynode films were determined by spectroscopic ellipsometry. Traditionally, the different methods of generating and analysing the polarization properties of light are termed as ellipsometry. A great feature of spectroscopic ellipsometry is that it measures two independent quantities at each wavelength, thus providing more information than other available techniques, such as conventional reflectometry. Spectroscopic ellipsometry is a highly accurate thin film measurement tool, with a relatively straightforward survey procedure through modelling analysis, especially when isotropic films are studied. This method is non-destructive and indirect (i.e. it requires a model analysis to convert the measured quantities into optical constants), and allows characterization of optically isotropic films, by measuring the change of polarization of light reflected from (or transmitted through) the surface. Spectroscopic ellipsometry is widely used to determine the thickness, optical constants, roughness, composition, crystallinity and other physical quantities related to optical properties. Measurement of thicknesses is possible in a wide range from a few angstroms to tens of microns, both for single layers and multilayer stacks [23].

As stated before, a high accuracy of ellipsometry is enabled by measuring two independent values, Ψ and Δ, which define the ratio of Fresnel reflection coefficients for the polarization parallel (R_p) and perpendicular (R_s) to the incidental plane:

$$\rho = \frac{R_p}{R_s} = \tan\Psi e^{i\Delta} \tag{3.3}$$

After the measurement of Ψ and Δ, a mathematical model specially developed for the investigated film is employed. The model contains known parameters: angle of incidence, the wavelength and polarization state of incoming light beam, but also the unknown quantities, such as the thickness and optical constants. Next, the unknown physical parameters are varied so that the generated fitted data closely matches the measured values of Ψ and Δ. The employed model depends on the type of the tynode material and will be described in details in the result sections of this and the following chapters. The variable angle spectroscopic ellipsometry (VASE) in this work is enabled by the Woollam M2000UI, with the ability to record data at angles between 45 and 75°, with a step of 5°, in the wavelength range between 245 and 1690 nm. Data collection is performed in 13 points across a wafer. Schematic of the principle of ellipsometry is represented in Figure 3.7.

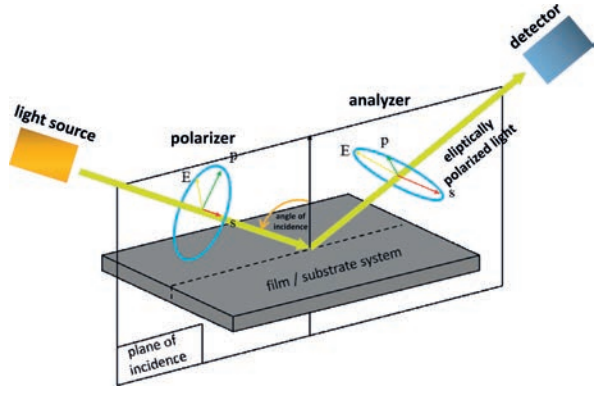

Figure 3.7: Principle of a spectroscopic ellipsometry measurement in which linearly polarized incident light (left) changes to elliptically polarized light (right) after the reflection from the investigated film [22].

3.3.3. ATOMIC FORCE MICROSCOPY (AFM)

AFM was developed as an extending method of scanning tunnelling microscopy for electrically non-conductive materials. It is pursued as a powerful method for characterization of samples in terms of mechanical, electrical and magnetic properties. The AFM probe, consisting of a micromachined cantilever, typically made of silicon or silicon nitride, and a very sharp tip with a radius of curvature down to 5 nm. The probe interacts with the surface through a raster scanning motion during which interatomic forces between the tip and the sample surface induce displacement of the tip and corresponding bending of the cantilever. The vertical movements of the tip are monitored through the beam deflection method. Namely, a laser beam focused on the back of cantilever is being reflected, and subsequently collected by a photodetector. The position change of a reflected laser spot is then translated into a vertical movement of a probe (Figure 3.8). In

this way a topographical image of the surface with atomic resolution is provided. Scanning of the surface is performed along closely spaced lines over a square-shaped area, and the sample is moved by a piezoelectric scanner.

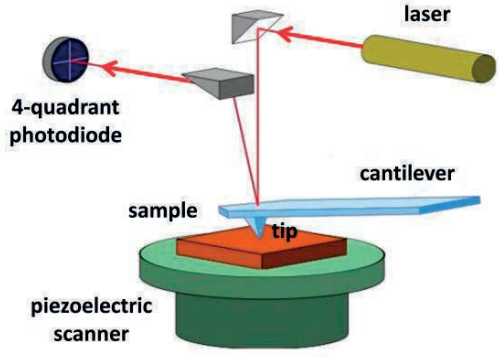

Figure 3.8: A schematic representation of the AFM instrument with its main components. Image adopted from [24].

One of the most common AFM operational procedures is the contact mode, where the tip scans the sample in contact with the surface. A constant force is applied and the cantilever is pushed towards the surface by a piezoelectric positioning element. The deflection of the cantilever is then sensed and compared by the DC feedback amplifier. If the measured value differs from the desired deflection, a voltage is applied to the piezo element and the sample is moved up or down so that the deflection is compensated. The voltage feed sent to piezo is a measure of height features on the sample. However, during the contact mode imaging, the high lateral force applied on the sample can damage the sample surface. To avoid that risk, a tapping mode with oscillation of the cantilever during the imaging may be employed. This method is particularly suitable for soft and fragile samples. The piezoelectric crystal enables the oscillation of the cantilever, near or at its resonant frequency, with amplitude greater than 20 nm when the tip is not in touch with the surface. The tip alternately lifts off and lightly touches the surface, inducing the energy loss and decrease of the oscillation amplitude. The change of amplitude is then used to identify the surface features. A thorough overview of AFM measurement modes and extensive applications can be found in [25].

The surface morphology of films in this work was characterized by Bruker FastScan AFM, with FastScan A probes provided by the manufacturer. Probes are equipped with a 27 μm long triangular silicon nitride cantilever with a nominal resonant frequency of 1400 kHz and a spring constant of 17 N/m. The silicon tip has an extremely sharp 5 nm tip radius, making it suitable for imaging a wide variety of hard and soft materials.

3.3.4. X-RAY DIFFRACTION (XRD)

X-ray diffraction is a technique employed for determining the atomic structure of a material. In an XRD setup, the sample is exposed to monochromatic X-ray radiation. If atoms in a material are arranged in a regular pattern (crystal), incoming waves will be subjected to destructive interference in most of directions. In some directions, however, waves with a wavelength λ will interfere constructively, so that Bragg's law is satisfied:

$$2d\sin\theta = n\lambda \tag{3.4}$$

where d is the separation between crystalline planes, θ is the angle of incidence and n an integer (Figure 3.9a). Scan of the samples at different angles is provided by a goniometer, where sample, photodetector and an X-ray source are mounted (Figure 3.9b). The output result is a set of peaks which are compared to the ICCD (International Center Diffraction Data) database. The intensity, area and FWHM of peaks are used to crystallographic and texture properties. Bruker D8 Advance diffractometer with Bragg-Brentano geometry and Lynxeye position sensitive detector are used for XRD analysis in this study. Data evaluation is conducted by utilizing DiffracSuite.EVA vs 4.2 software, also supplied by Bruker.

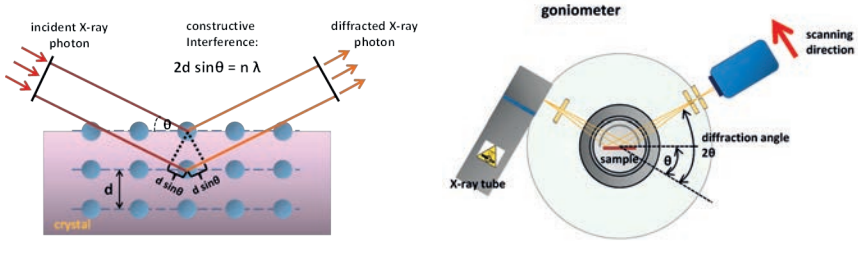

(a) (b)

Figure 3.9: A graphical representation of X-ray radiation diffracting from crystal planes and Bragg's law (a) and an example of an XRD instrument with $\theta - 2\theta$ configuration of the goniometer (b) [26].

3.3.5. X-RAY SPECTROSCOPY (XPS)

X-ray spectroscopy, also known as electron spectroscopy for chemical analysis (ESCA), is a characterization method used for the investigation of surface chemistry. It is a widely used electron spectroscopic technique to determine the elemental composition, as it allows the detection of elements with atomic number equal and greater than 3 in the outer 1 – 10 nm-thick layer of any solid substrate. Thus, hydrogen and helium content is not easily detected by XPS measurement. Additionally, investigation of material composition in areas below the sampling can be carried out through sputter depth profiling from the surface down, typically using Ar^+ energetic ions. Information from XPS data is of vital importance in understanding the electronic structure of solid materials, and can be collected with an easy sample preparation.

In the XPS setup, the surface is irradiated by X-rays (commonly Al Kα or Mg Kα), most often under ultra-high vacuum conditions. Excited core-level electrons are then emitted from their initial states, with kinetic energy and intensity which depend on the incident X-rays and binding energy of the atomic orbital. These quantities are analysed to deduce the concentrations of present elements (providing the minimal concentration is 0.1 atomic %). Electrons ejected into the vacuum are collected by an electron analyser which measures their kinetic energy and produces an energy spectrum of intensity versus binding energy of electrons before excitation (Figure 3.10). Each prominent peak in the spectrum corresponds to a different element, and its intensity is used for the calculation of its concentration. For further understanding of fundamentals and practical aspects of XPS, reference [27] is suggested.

The X-ray photoelectron spectrometer used for the analysis of tynode films is K-Alpha manufactured by Thermo Scientific. The setup has depth profiling capabilities, and sample irradiation is provided by an Al Kα X-ray source, with energies in the range from 100 to 4000 eV.

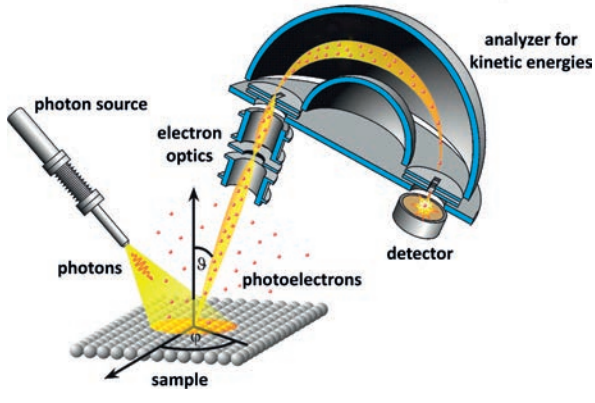

Figure 3.10: Schematic representation of an XPS system: the sample is exposed to an X-ray beam and the energies of emitted photoelectrons are measured by the electron analyzer.

3.3.6. MICROMEGAS DETECTOR

A new procedure for in situ measurements of the specific resistivity of tynode materials involving a so called Micromegas was performed. The Micromegas detector is a modern 2D variant of a Geiger-Muller detector in which the output signal charge is proportional to the ionization charge in a gas-filled volume. For this in-situ method there is no need to apply a second contact electrode and acurate measurements of the total current, surface area and voltage drop are possible.

For in-situ measurements of specific resistivity of high resistive materials, a novel method is developed, based on the use of Micromegas detector [28]. The film under investigation is placed on top of a grounded anode, and the volume in between cathode and anode containing the Micromegas grid is filled with a gas, as shown in Figure

3.11a. When a high voltage, in the range from -300 to -1000 V, is applied between the cathode and grid, electron-ion pairs are created in an ionization process. Electrons passing through holes in the grid ionize gas atoms and molecules, creating an avalanche of secondary electrons. This process has statistical fluctuations, but the average gas gain depends on the potential difference between the grid and the anode, the geometry of Micromegas and the used gas. The SEM image of GridPix detector, consisting of Micromegas, SU-8 dyke supporting structure and CMOS TimePix chip is given in Figure 3.11b, together with dimensions of its components. If the potential on the grid is V_{grid} and V_D the voltage needed to double the gain G, then the average amplification gain can be expressed as:

$$G = G_0 e^{(\frac{\ln 2}{V_D}|V_{grid}|)} \tag{3.5}$$

where G_0 is the gain measured when no potential is applied on the grid and the Micromegas does not contribute to the gas ionization. However, if a resistive film is placed on top of the anode, the potential over avalanche gap is no longer equal to $|V_{grid}|$, and changes to:

$$|V_A| = |V_{grid}| - |V_T| \tag{3.6}$$

where V_T is the potential on top of the resistive layer. In fact, resistive film can be described as a non-ideal capacitor which depletes accumulated charge back to the ground potential, after the electron flow has stopped. Therefore, V_T is a function of time:

$$V_T = V_{T,i} e^{-\frac{t}{\tau}} \tag{3.7}$$

where $\tau = RC$ and $V_{T,i}$ is the initial value of V_T to which the resistive layer charged under the avalanche of electrons. Combining Equations 3.6 and 3.8 results in the formula for average gas gain:

$$G(t) = G_0^{'} e^{(-\frac{\ln 2}{V_D} V_{T,i} e^{-\frac{t}{\tau}})} \tag{3.8}$$

with $G_0^{'}$ given as:

$$G = G_0 e^{(\frac{\ln 2}{V_D}|V_{grid}|)} \tag{3.9}$$

An aluminum airtight container is used as a grounded anode on which a sample with the film under investigation is glued. The Micromegas is placed on top of the resistive layer, as shown in Figure 3.11c. The aluminum container is flushed and filled with a mixture of isobutane and propane. The voltage applied on the cathode is -1000 V, and varies from –300 to –380 V on the grid. Electron-ion pairs are created in the conversion gap between the cathode and the grid by using the radioactive source iron-55 (^{55}Fe). The small potential on the grid is monitored with an oscilloscope and collected by a multichannel analyzer. At first, the value of $G_0^{'}$ can be measured by a short exposure of ^{55}Fe. This is followed by the prolonged exposure to the radioactive source, until the charging of the resistive layer is saturated. Then, the radioactive source is activated at around 10 cm away from the sample so that it does not contribute to the further charging or recharging

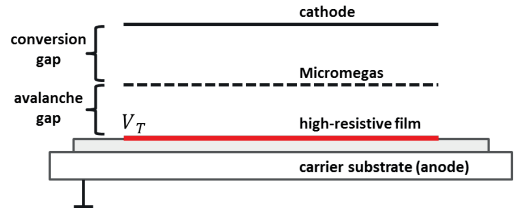

(a)

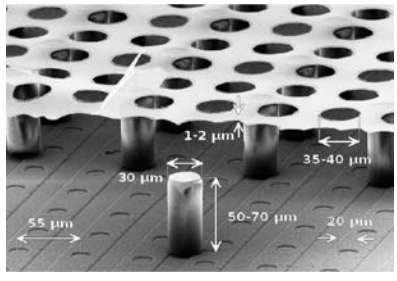

(b)

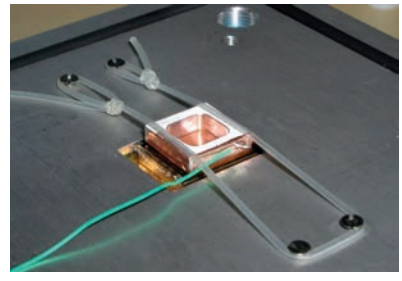

(c)

Figure 3.11: Schematic drawing of the setup used for the specific resistivity measurement (a). SEM image of the Micromegas supported by SU-8 pillars on top of TimePix chip (b). The film under investigation is bonded to the aluminium housing and capped by the Micromegas (c) [29].

of the film. This allows measurement of $G(t)$, conducted in several points in time, with a separation of 5 – 10 min. The saturation of charging is achieved by prolonged exposure to the radioactive source. The Gompertz function is used for fitting the collected data and extracting the values of τ and ρ, as described in [29] [30].

3.3.7. SETUP FOR SEE ANALYSIS

Two most common ways to quantify SEE are a sample biasing method (to repel or attract secondary electrons), or a retarding field grid detector (with a bias between 0 and -50 V). The second approach is more complex, but provides better measurement accuracy. The choice of technique depends on the nature of samples: while analysis of conductive materials is straightforward due to a quick dissipation of charge only by sample grounding, insulators require the use of pulsed electron sources. A detailed overview of measuremet studies on SEE of various insulators is provided by Thomson [31]. The Dual Faraday Cup (DFC) is a setup specially designed in our group for the measurement of transmission secondary electron yield [32] [33]. This apparatus is mounted on the sample stage inside FEI NovaNanoLab 650 Dual Beam scanning electron microscope (SEM), at a vacuum level between 10^{-5} and 10^{-6} mbar. Due to the size of the tynodes (typically less than a mm^2), measurements of transmission yield require an electron beam with a smaller spot size compared to the investigation of reflection yield. The imaging capabilities of the SEM are of great convenience in locating the tynode and as a verification that only the active (ultra-thin) part of the tynode is being irradiated. The DFC setup consists

of a copper sample holder, a retarding grid and a copper collector, as illustrated in Figure 3.12a. The electrodes are isolated from each other and connected to a sourcemeter (Keithley 2450), via a feedthrough. A bias voltage between electrodes can be set from –200 to 200 V, and the currents are measured simultaneously. The SEM is provided with an electron source operating in a wide energy range (0.3 – 30 keV). A beam current, varying from a few pA to a few nA, is measured with a small Faraday cup inside the sample holder. For the analysis of the transmission yield, only the lower section of the DFC is put to use. Essentially, the DFC setup provides a sample-biasing method where two separate measurements are performed.

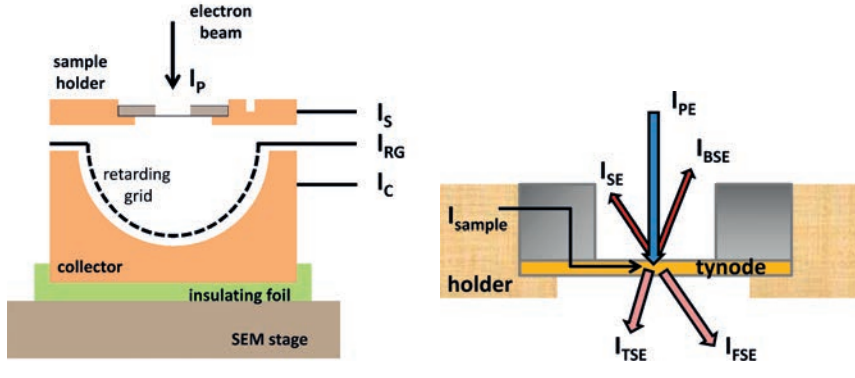

(a) (b)

Figure 3.12: The Dual Faraday Cup (DFC) setup consisting of three electrodes: the sample holder, retarding grid and collector (with corresponding currents I_S, I_{RG} and I_C, respectively), all of which are electrically insulated by Kapton foils and can be biased (a). Different groups of electrons participating in SEE process are shown in (b).

In the first measurement, the sample is negatively biased (−50 V), while retarding grid and collector are at 0 V. The total transmission electron coefficient (TEY) is measured directly and can be expressed as:

$$TEY(E) = \frac{I_{RG,-} + I_{C,-}}{I_P} \tag{3.10}$$

Where I_P is the electron beam current, $I_{RG,-}$ and $I_{C,-}$ are the retarding grid and the collector current, respectively, both measured while the sample is negatively biased. The total emission coefficient (σ) can be determined by measuring the sample current ($I_{S,-}$):

$$\sigma(E) = \frac{I_P - I_{S,-}}{I_P} \tag{3.11}$$

where $I_{S,-}$ stands for the sample current recorded at a negative bias of the sample. Since σ represents the sum of total reflection and transmission coefficents (REY and TEY), the total reflection coefficient (REY) is measured indirectly and can be obtained by substitution of Equations (3.10) and (3.11) into:

$$REY(E) = \sigma(E) - TEY(E) \tag{3.12}$$

The total reflection and transmission coefficients include not only the contribution of true secondary electrons, but also the back-scattered electrons (BSE) and forward-scattered electrons (FSE) with higher energies (currents shown in Figure 3.12b). Therefore, for the second measurement, a positively biased sample is needed to separate the impact of these two electron categories. With the sample holder, retarding grid and collector connected to + 50, 0 and +50 V, respectively, BSEs ($E_{BSE} > 50$ eV) and FSEs ($E_{FSE} > 50$ eV) are stopped at the collector, while ("true") secondary electrons ($E_{SE} < 50$ eV) are recaptured. The forward-scattered electron coefficient $FSEY$ is given by:

$$FSEY(E) = \frac{I_{RG,+} + I_{C,+}}{I_P} \tag{3.13}$$

where $I_{RG,+}$ and $I_{C,+}$ are currents of the retarding grid and the collector, respectively, both measured when the sample is positively biased. Again, by measuring the sample current and by using the equivalent of Equation (3.11) for the positive biased sample and Equation (3.13), we derive the expression for the back-scattered electron coefficient ($BSEY$):

$$BSEY(E) = \frac{I_P - I_{S,+} - I_{RG,+} - I_{C,+}}{I_P} \tag{3.14}$$

with all the currents measured while the sample is positively biased. The reflective secondary electron coefficient (SEY) is then simply calculated by substitution of Equations (3.10) – (3.12) and (3.14) into:

$$SEY(E) = REY(E) - BSEY(E). \tag{3.15}$$

The "true" transmission secondary electron coefficient ($TSEY$) is expressed as:

$$TSEY(E) = TEY(E) - FSEY(E) = \frac{I_{RG,-} + I_{C,-}}{I_P} - \frac{I_{RG,+} + I_{C,+}}{I_P} \tag{3.16}$$

During the RSEY measurements of various materials, a conductive silver paint is applied on the side of the sample in order to improve the electrical contact between the silicon substrate and the copper sample holder. However, a major limitation of the conducted SEM measurements is the relatively low vacuum level. In such an environment, the formation of surface contamination is not excluded: even after a bakeout, water and hydrocarbon molecules will quickly attach to the surface, affecting its electron affinity. The effect of surface contamination (and surface termination) has to be investigated in an ultra-high vacuum (UHV) setup.

METHOD FOR THE MEASUREMENT OF SEY IN REFLECTION MODE

In addition to measurements of transmission SEY of the tynodes, DFC setup has the capability to analyze the SEY in reflection mode (recorded on the dynodes). This procedure, more straightforward than the above described method, is employed for the investigation of SEE performance of MgO deposited on Si substrate (presented in Section 5.5). During the measurement of RSEE, the sample is biased at 50 V, which ensures the repellence of all secondary electrons extracted from the sample surface. Two currents are monitored in the experiment: the one through sample (I_S) and the other through

primary beam current (I_P). The latter is measured with a Faraday cup placed inside the sample holder and varies from 20 to 160 pA depending on the chosen electron energy. Reflective SEY (RSEY) of the dynode (differs from identically noted coefficient introduced in the previous section!) is then given by:

$$RSEY = 1 - \frac{I_S}{I_P} \tag{3.17}$$

In order to avoid charge-up and reduce the electron dose per surface unit, we operated SEM in a scan mode with a horizontal-field width of 2.56 mm. To identify charge-up effects, we chose 20 s-long scans at each energy of the primary beam since the effect is evident after measuring the current change throughout this time frame.

3.4. RESULTS AND DISCUSSION

IN the following section the SiN tynode performance, in relation to the properties of interest for TiPC and other possible MEMS applications, is reported and discussed. In an attempt to reduce charge up effects after the escape of secondary electrons from the tynode film, we developed SiN layers with a higher Si amount to reduce their resistivity. This was achieved by controlling the composition of the gas mixture in the LPCVD process.

3.4.1. RESIDUAL STRESS

The stress of the SiN films grown by using different ratio of composition gasses (Table 3.1) is determined by measuring the wafer curvature. Films with a thickness of around 1000 nm, produced with deposition times between 140 and 162 min are tested. Figure 3.13a reveals that by increasing the DCS/ammonia ratio, layers with lower tensile stress are produced. Moreover, if the Si content is sufficiently enhanced, stress is converted from tensile to compressive, as in the case of "Type 3" SiN film. Such trend in stress behaviour, at similar deposition conditions, is reported by other groups [34] [15]. According to [35] the high tensile stress originates mainly from the shrinking of the film caused by the dissociation of Si-H and N-H bonds, and rearranging of dangling bonds to stable Si-N bonds. However, LPCVD SiN films contain a very small amount of hydrogen (in this study below detection level), and therefore the resulting stress is low, not exceeding 200 MPa.

3.4.2. THICKNESS AND OPTICAL PROPERTIES

The thickness and refractive index of SiN layers grown on top of a Si substrate in a 15 min long deposition process, while using different flows of gasses, was studied. As shown on Figure 3.13b, the growth rate (GR) of SiN films reduces with the increase of DCS/NH_3 ratio. The most efficient employed gas mixture, containing 340 sccm of NH_3 and 60 sccm of DCS, resulted in a deposition rate of 6.67 nm/min for "Type 1" SiN, whereas somewhat slower growth (5.83 nm/min) was observed for the highest investigated flow ("Type 3"). All films exhibit very good thickness uniformity, with standard deviations in the range of only 0.51 – 0.76 nm measured in 13 points across the wafer. Plot in Figure 3.13c shows

the significant influence of gas composition on the refractive index. Namely, higher flow of DCS caused the elevation of refractive index from 2.19 to 2.35, which typically indicates a higher Si content in the material.

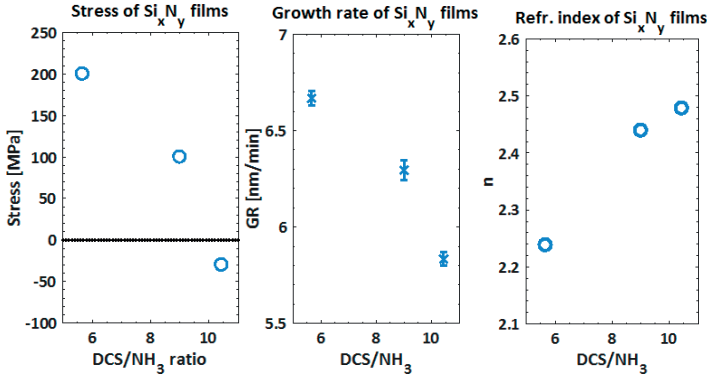

(a) (b) (c)

Figure 3.13: Stress of LPCVD SiN films prepared by using different ratio of composition gasses (a). Growth rate of Si_xN_y layers for different DCS/ammonia ratio (b) and their refractive index at the wavelength of 633 nm (c). Deposition time was set to 15 min, so that all films were approximately 100 nm thick.

3.4.3. SURFACE MORPHOLOGY

AFM analysis of LPCVD SiN films shows that the surface of these films is very smooth, uniform and without hillocks formation. We observed a negligible increase of surface roughness when a gas mixture with a higher DCS content is employed, as shown in Figure 3.14.

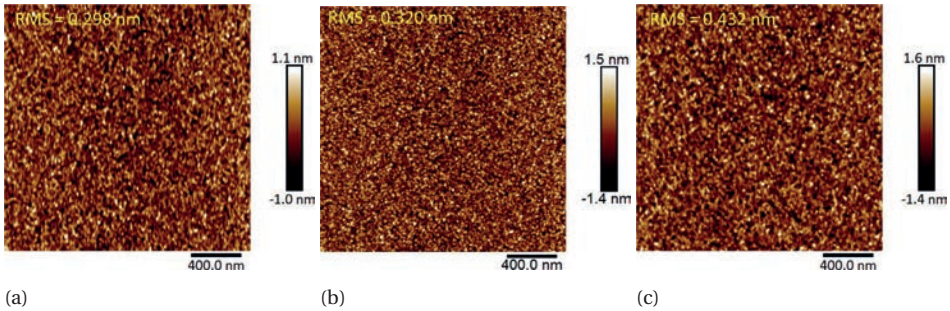

(a) (b) (c)

Figure 3.14: AFM images of $2 \times 2\ \mu m^2$ area of 40 nm-thick SiN deposited using gas mixture with DCS:NH_3 ratio of "Type 1" (a) and "Type 2" (b) and "Type 3" (c).

3.4.4. ELEMENTAL COMPOSITION AND RESISTIVITY

For the evaluation of the elemental composition of the deposited films, we performed XPS measurements by ion beam etching to eliminate the contribution of surface impurities in films "Type 1" and "Type 2". (Figure 3.15). From a high resolution acquisition around Si 2p and N 1s peaks we calculated the atomic percentage of silicon to be only slightly higher for the "Type 2" SiN film (Table 3.2). Namely, silicon to nitrogen ratio increased from 0.96 to 1.01 after the flow of ammonia in the gas mixture was decreased by 20 sccm ("Type 2"), and that of DCS increased by the same amount. Oxygen portion in the bulk is found to be around 4.5% for both films. In contrast, it increases to 20.5% on the surface, which implies a strong oxidation and formation of silicon oxynitride (Figure 3.16). However, it should be emphasized that samples were not subjected to any cleaning procedure prior to the XPS investigation in order to reduce the oxygen content from the surface.

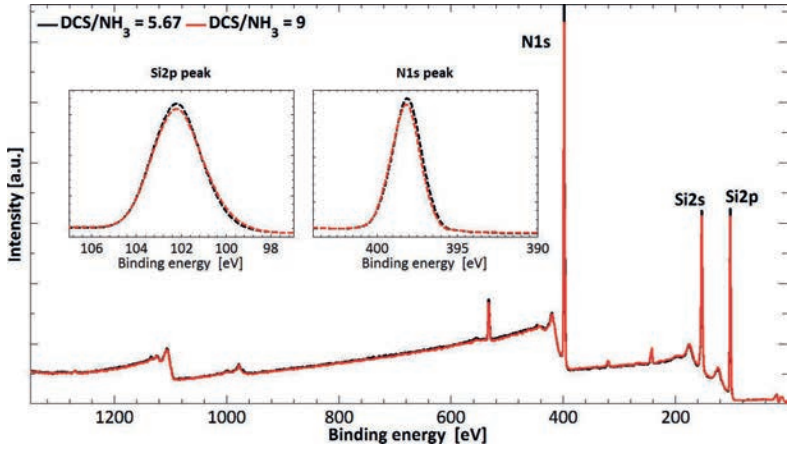

Figure 3.15: XPS spectrum obtained from "Type 1" (black plot) and "Type 2" (red plot) SiN films.

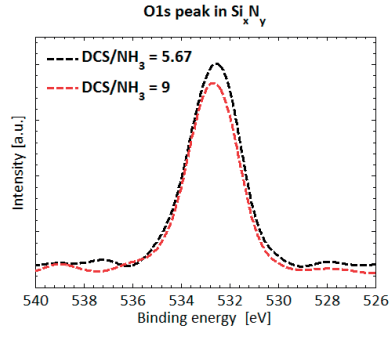

Figure 3.16: In-bulk XPS spectra of O 1s peaks in "Type 1" and "Type 2" SiN films (black and red plot, respectively).

SiN film	Si 2p (%)	N 1s (%)	O 1s (%)	Peak position (eV) / FWHM (eV)		
				Si 2p	N 1s	O 1s
"Type 1"	46.21	47.85	4.53	102.12 / 2.88	398.10 / 2.55	532.49 / 1.63
"Type 2"	47.21	46.88	4.45	102.10 / 2.95	398.15 / 2.52	532.83 / 2.70

Table 3.2: Information on relevant peaks and atomic content of the studied Si_xN_y films, obtained from in-depth XPS analysis. The remaining portion, usually around 1.45%, origins from the Ar used in the ion beam etching of the material. For this characterization we used 40 nm-thick silicon nitride layers, both deposited on top of Si substrate. Since carbon was not present in any of prepared samples, plots were not normalized to C 1s or any other peak.

Typically, LPCVD SiN films contain up to 2 – 10 at% of hydrogen, with much higher concentration of N – H bonds compared to Si – H bonds [36]. Because of the limitations of XPS, Rutherford backscattering spectroscopy (RBS) has been conducted for "Type 1" and "Type 2" SiN films to quantify the incorporation of hydrogen. Results summarized in Table 3.3 indicate very low hydrogen levels of approximately 0.5 at%. Moreover, the Si/N ratio deducted from RBS data does not differ for the two SiN films, and is somewhat lower than the XPS results. Both analysis conducted to investigate the elemental composition (XPS and RBS) showed no significant change of the Si/N ratio. Micromegas-based measurements conducted on 1 µm-thick SiN films "Type 1, 2 and 3" revealed that the resistivity of these films were 1.4×10^{13}, 0.8×10^{11} and 2.0×10^{10} Ω m. Only a few studies available on electrical properties of this material, stoichiometric LPCVD Si_3N_4 in specific, report on resistivity values in the range from 10^{13} to 10^{15} Ω m [37] [38]. Due to a higher Si content, our films have lower resistivity than that.

SiN film	Si (%)	N (%)	H (%)
"Type 1"	47.334 ± 1.420	52.163 ± 2.086	0.503 ± 0.035
"Type 2"	47.393 ± 1.422	52.316 ± 2.093	0.504 ± 0.035

Table 3.3: Elemental composition of "Type 1" and "Type 2" SiN layers, obtained from RBS investigation.

3.4.5. SECONDARY ELECTRON EMISSION

Primary electrons travelling through the tynode material interact with it and lose energy, in the process described in Section 2.2. The low- and high-energetic electrons can be separated by using a negatively and positively biased sample, respectively. At first, the total transmission yield (TEY) and total reflection yield (REY) that contains both type of electrons are measured. In the second measurement, the positively biased sample retracts the low-energetic electrons, so only the back-scattered- and forward-scattered electron yields (BSEY and FSEY, respectively) are measured. By subtracting the values of these two measurements, the true secondary electron emission is obtained. Currents used for calculations of electron emission coefficients of the tynodes are shown in Figure 3.12b.

Two 40 nm-thick Si_xN_y tynodes, produced with different DCS/ammonia ratios: 5.67 ("Type 1") and 9 ("Type 2"), were subjected to SEE analysis. SEE coefficients extracted from these measurements are plotted in Figure 3.17. Energy of primary electrons in the

SEM was increased from 0.3 to 10 keV, with fine steps of 100 eV for energies below 3.4 keV and coarse steps of 1 keV in the tail of the curves. A slightly better response is observed for the tynode "Type 1", with a maximum TEY of 1.57 corresponding to the energy of 2.85 keV. The TEY peak of 1.49 occurred at the same position for the "Type 2" sample, which proves that these two tynodes have the same thickness. This implies that a charge required for triggering the pixel circuitry of TimePix3 chip can be produced with a stack of 14 or more tynodes. Due to their poor SEE performance, we conclude that SiN tynodes are inadequate for the application in TiPC. Similar to studies on diamond, hydrogen termination of SiN is predicted to provide NEA (simulation results presented in [32]). Even though an effort in this direction could be made to increase its SEE, in our further research we discarded SiN. Instead, we explored other materials that are more efficient emitters of secondary electrons and can be produced in films even thinner than here presented LPCVD SiN.

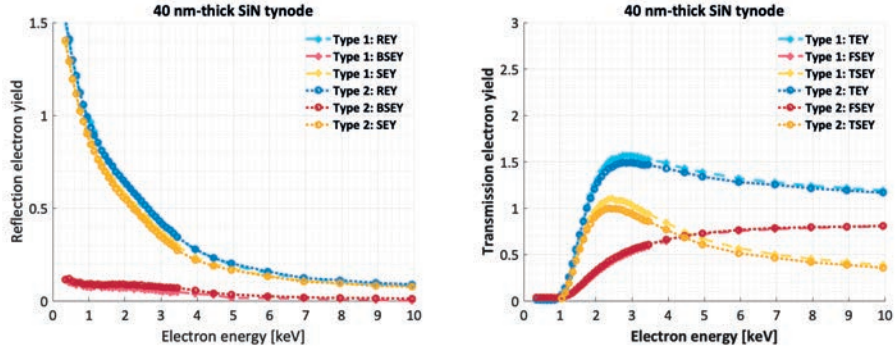

(a) (b)

Figure 3.17: Reflection (a) and transmission (b) electron emission coefficients of 40 nm-thick SiN tynodes. "Type 1" and "Type 2" stand for SiN films deposited by using DCS/NH_3 ratio of 5.67 and 9, respectively. Definitions of plotted coefficients are given in Section 3.3.7.

3.5. CONCLUSIONS

This study presents the manufacturing of LPCVD Si_xN_y tynodes and their physical properties relevant for the applicability in TiPC. However, studied features and presented fabrication methods may be of interest for other silicon nitride MEMS-based devices, especially in applications where ultra-thin membranes are required. Investigated materials exhibit very low tensile stress, high uniformity in thickness, absence of impurities and remarkably smooth surface. However, the LPCVD method has two major disadvantages: high processing temperature and inability to obtain good quality, continuous films with thicknesses lower than 10 nm (the minimum thickness of the membranes fabricated by using the same LPCVD reactor as in this work was 15 nm [6]).Thinner tynodes are required for the detection of low energetic photoelectrons in the TiPC, whereas the low-temperature deposition is generally desired since they provide higher degree of freedom in MEMS processing. Finally, with a dedicated multi-electrode setup in SEM, we demon-

strated that Si_xN_y is not an efficient secondary electron emitter, with a TEY of around 1.5 for the 40 nm-thick tynode. Further improvement of SEY can be achieved by investigating more promising tynode materials, such as alumina and magnesium oxide, which will be addressed in the next two chapters.

REFERENCES

[1] A.E. Kaloyeros, F.A. Jové, J. Goff, and B. Arkles. Silicon nitride and silicon nitride-rich thin film technologies: trends in deposition techniques and related applications. *ECS Journal of Solid State Science and Technology*, 6(10):P691–P714, 2017.

[2] P. Ekkels, R.W. Tjerkstra, G.J.M. Krijnen, J.W. Berenschot, J. Brugger, and M.C. Elwenspoek. Fabrication of functional structures on thin silicon nitride membranes. *Microelectronic engineering*, 67:422–429, 2003.

[3] S.C. Ko, Y.C. Kim, S.S. Lee, S.H. Choi, and S.R. Kim. Micromachined piezoelectric membrane acoustic device. *Sensors and Actuators A: Physical*, 103(1-2):130–134, 2003.

[4] R. Ramachandra, H. Demers, and N. de Jonge. Atomic-resolution scanning transmission electron microscopy through 50-nm-thick silicon nitride membranes. *Applied physics letters*, 98(9):093109, 2011.

[5] M.M. Leivo and J.P. Pekola. Thermal characteristics of silicon nitride membranes at sub-kelvin temperatures. *Applied Physics Letters*, 72(11):1305–1307, 1998.

[6] T. Alan, T. Yokosawa, J. Gaspar, G. Pandraud, O. Paul, F. Creemer, P.M. Sarro, and H.W. Zandbergen. Micro-fabricated channel with ultra-thin yet ultra-strong windows enables electron microscopy under 4-bar pressure. *Applied Physics Letters*, 100(8):081903, 2012.

[7] G. Suchaneck, V. Norkus, and G. Gerlach. Low-temperature PECVD-deposited silicon nitride thin films for sensor applications. *Surface and Coatings Technology*, 142:808–812, 2001.

[8] L. Liu, W-G. Liu, N. Cao, and C-L. Cai. Study on the performance of PECVD silicon nitride thin films. *Defence Technology*, 9(2):121–126, 2013.

[9] H. Goto, K. Shibahara, and S. Yokoyama. Atomic layer controlled deposition of silicon nitride with self-limiting mechanism. *Applied physics letters*, 68(23):3257–3259, 1996.

[10] A. Nakajima, T. Yoshimoto, T. Kidera, and S. Yokoyama. Low-temperature formation of silicon nitride gate dielectrics by atomic layer deposition. *Applied Physics Letters*, 79(5):665–667, 2001.

[11] X. Meng, Y-C. Byun, H.S. Kim, J.S. Lee, A.T. Lucero, L. Cheng, and J. Kim. Atomic layer deposition of silicon nitride thin films: A review of recent progress, challenges, and outlooks. *Materials*, 9(12), 2016.

[12] K.L. Choy. Chemical vapour deposition of coatings. *Progress in materials science*, 48(2):57–170, 2003.

[13] S. Wolf and R.N. Tauber. *Silicon Processing for the VLSI Era: Process technology*. Silicon Processing for the VLSI Era. Lattice Press, 2000.

[14] B. Morana. *Silicon carbide thin films for MEMS nanoreactors for in-situ transmission electron microscopy*. PhD thesis, Delft University of Technology, 2015.

[15] P. Temple-Boyer, C. Rossi, E. Saint-Etienne, and E. Scheid. Residual stress in low pressure chemical vapor deposition SiNx films deposited from silane and ammonia. *Journal of Vacuum Science & Technology A*, 16(4):2003–2007, 1998.

[16] K. Nishimura, T. Itotani, and K. Ohya. Influence of surface roughness on secondary electron emission and electron backscattering from metal surface. *Japanese Journal of Applied Physics*, 33(Part 1, No. 8):4727–4734, 1994.

[17] J.E. Yater and A. Shih. Secondary electron emission characteristics of single-crystal and polycrystalline diamond. *Journal of Applied Physics*, 87(11):8103–8112, 2000.

[18] W. Lang, G. Muk, E. Rose, J. Bausells, K. Kuhl, N. Moldovan, and J. Suski. Stress compensation techniques in thin layers applied to silicon micromachining. *MRS Online Proceedings Library Archive*, 284, 1992.

[19] J.W. Hutchinson. *Stresses and failure modes in thin films and multilayers*. 1996.

[20] A.M. Engwall, Z. Rao, and E. Chason. Origins of residual stress in thin films: Interaction between microstructure and growth kinetics. *Materials & Design*, 110:616–623, 2016.

[21] G.G. Stoney. The tension of metallic films deposited by electrolysis. *Proceedings of the Royal Society of London. Series A, Containing Papers of a Mathematical and Physical Character*, 82(553):172–175, 1909.

[22] http://www.tohotechnology.com/images/flx-specs.pdf.

[23] H. Fujiwara. *Spectroscopic ellipsometry: principles and applications*. John Wiley & Sons, Ltd, 2007.

[24] http://commons.wikimedia.org/wiki/File:AFM_schematic_(EN).svg.

[25] G. Haugstad. *Atomic force microscopy: understanding basic modes and advanced applications*. John Wiley & Sons, Inc., 2012.

[26] J. Epp. *X-ray diffraction (XRD) techniques for materials characterization*. Woodhead Publishing, 2016.

[27] P. van der Heide. *X-Ray Photoelectron Spectroscopy*. John Wiley & Sons, Inc., 2011.

[28] G. Charpak, J. Derre, Y. Giomataris, and P. Rebourgeard. Micromegas, a multipurpose gaseous detector. *Nuclear Instruments and Methods in Physics Research Section A: Accelerators, Spectrometers, Detectors and Associated Equipment*, 478(1-2):26–36, 2002.

[29] H. van der Graaf. Measurement of the specific resistivity of potential protection layers. To be submitted in *Nuclear Instruments and Methods in Physics Research Section B*.

[30] K. van t' Veer. Development of the QUAD focus GridPix gaseous tracking detector, 2015. HBO Bachelor Graduation Report.

[31] C.D. Thomson. *Measurements of the secondary electron emission properties of insulators*. PhD thesis, Utah State University, 2005.

[32] H. van der Graaf, H. Akhtar, N. Budko, H.W. Chan, C.W. Hagen, Conny C.T. Hansson, G. Nützel, S.D. Pinto, V. Prodanović, B. Raftari, and et. al. The tynode: A new vacuum electron multiplier. *Nuclear Instruments and Methods in Physics Research Section A: Accelerators, Spectrometers, Detectors and Associated Equipment*, 847:148–161, 2017.

[33] H.W. Chan. Transmission secondary electron emission of sub-10-kev electrons from ultra-thin layered alumina/titanium nitride composite membranes. To be submitted in *Nuclear Instruments and Methods in Physics Research Section B*.

[34] K.D. Mackenzie, D.J. Johnson, M.W. Devre, R. Westerman, and B.R. Reelfs. Stress control of Si-based PECVD dielectrics. *Proceedings - Electrochemical Society*, pages 148 – 159, 01 2005.

[35] A.G. Noskov, E.B. Gorokhov, G.A. Sokolova, E.M. Trukhanov, and S.I. Stenin. Correlation between stress and structure in chemically vapour deposited silicon nitride films. *Thin Solid Films*, 162:129 – 143, 1988.

[36] A.W.M. Bik, R.N.H. Linssen, F.H.P.M. Habraken, W.F. van der Weg, and A.E.T. Kuiper. Diffusion of hydrogen in low-pressure chemical vapor deposited silicon nitride films. *Applied physics letters*, 56(25):2530–2532, 1990.

[37] B.C. Joshi, G. Eranna, D.P. Runthala, B.B. Dixit, O.P. Wadhawan, and P.D. Vyas. LPCVD and PECVD silicon nitride for microelectronics technology. *Indian journal of engineering and material sciences*, pages 303–309, 2000.

[38] M.J. Madou. *Fundamentals of microfabrication: the science of miniaturization*. CRC press, 2002.

4

Atomic Layer Deposited Alumina Tynodes

Aluminium oxide (alumina) has been a material of choice in devices where efficient electron multiplication is demanded, such as in microchannel plate-based photodetectors where it provided RSEY of around 3. For the preparation of alumina tynodes, we employed atomic layer deposition (ALD) due to its excellent control over thickness and conformality. Alumina films, produced in the temperature range from 100 to 300 °C, have been subjected to investigation of various material properties. Tynodes with thicknesses from 5 to 50 nm have been fabricated and characterized in terms of SEE.

Parts of this Chapter have been published in: "Ultra-thin alumina and silicon nitride MEMS fabricated membranes for the electron multiplication", *Nanotechnology*, 29(15):155703, 2018.

4.1. ALD

ATOMIC layer deposition (ALD) is a gas-phase method for growing ultra-thin films based on sequential self-limiting surface reactions. Initially known as atomic layer epitaxy, this technology was developed in 1970s to produce improved ZnS layers for thin film electroluminescent (TFEL) flat panel displays [1]. Precise thickness control on large area substrates and conformal covering of challenging structures, such as high aspect ratio (up to $1:10^5$) trenches, grooves and pores with continuous pinhole-free films, are some of most outstanding merits of ALD [2] [3]. ALD process temperatures can exceed 500 °C, though by far most depositions are conducted around 300 °C. The lower range limit, however, can be even room temperature, and for this reason ALD is utilized for coating thermally sensitive substrates such as polymers, biomolecules and various electronic devices [4] [5]. ALD processes have been developed for oxides, nitrides, carbides, fluorides, certain metals, II–VI and III–V compounds, and recently also for organic materials. This deposition method can be performed on a wide range of substrates, which enables realization of complex nanolaminates and stacking of ultra-thin films for different applications [6]. Numerous high quality metallic and ceramic ALD films have been applied in nanotechnology, photovoltaics, organic and flexible electronics.

Unlike continuous CVD growth, ALD growth is carried out through cycles in which sequential, self-saturating reactions are taking place. Each cycle consists of four steps (a - d), as illustrated in Figure 4.1:

(a) Introduction of the first gaseous precursor and its chemisorption onto the substrate;

(b) Inert gas purge for removal of gaseous by-products;

(c) Introduction of the second precursor and surface reaction to produce a monolayer of a film;

(d) Another inert gas purge for removal of gaseous by-products.

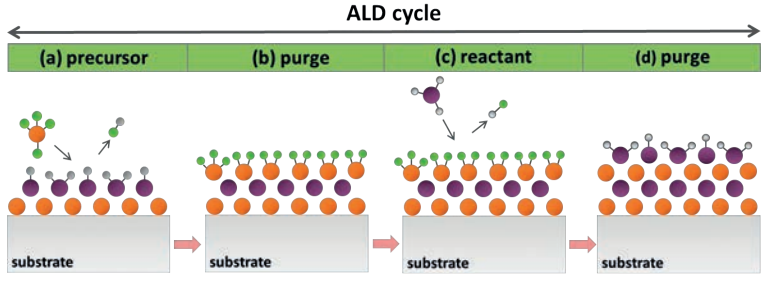

Figure 4.1: Diagram of a typical ALD cycle, consisting of pulses of precursor (a) and reactant (c), and purging steps in between (b, d).

ALD growth requires typically two or more chemical precursors, each providing different elements in the produced film. For the growth of pure films, precursors must pro-

vide reactions with complete ligand exchange, at moderate temperatures. Incomplete reactions lead to the incorporation of impurities into the films (such as carbon originating from the organic precursors). Additionally, chemisorption of precursors on the substrate and their reaction with surface groups must be completed rapidly (in 1 sec or less), so that the growth at a reasonable speed rate is attained. Even though ALD by nature is a vapour-based technique, it is considered to be particularly convenient choice for growth of very thin and conformal films. This asset is a consequence of the described deposition mechanism - namely, precursor molecules react only with the substrate (not with each other). Moreover, reactants are not present together in the same phase – they are being sequentially introduced in the chamber, with an inert gas purging step in between.

Activation of surface chemical reaction in ALD can be achieved by heating of the substrate (thermal ALD), or by using plasma excitation to create reactive vapour species (plasma enhanced ALD, PEALD). Enhanced energy offers several advantages, the main being a higher growth rate and a possibility to conduct the deposition even at the room temperature. The drawbacks, however, may include plasma damage by ions and UV radiation in the vacuum interacting on the surface, known as plasma-induced damage [7].

4.2. ALD ALUMINA

GROWTH of Al_2O_3 (alumina) is one of the most extensively studied ALD processes. Being a high-k material with excellent dielectric properties, alumina has a great potential to replace SiO_2 as gate dielectric in CMOS and MOSFET transistors [8]. ALD alumina is known to be thermally and chemically stable, with a good adhesion to many surfaces in a wide temperature range, and a minor change of growth rate [9] [10]. This material has been successfully grown on a variety of substrates, including metals, oxides, nitrides and heat sensitive polymers [5]. Furthermore, Groner et al. [4] provided extensive study on ALD alumina growth on polyethylene terephthalate (PET) substrate in the temperature range 33 – 177 °C.

ALD alumina is employed as a passivation layer for plastic substrates and optical devices, mainly OLEDs [11] [12] [13] and has multiple applications in the PV industry, for passivation, diffusion and encapsulation [14]. In addition, very thin alumina may be used as a very efficient masking MEMS material in a deep reactive ion Si etching at cryogenic temperatures, with Si to Al_2O_3 selectivity of 70000:1 [15]. In the area of photodetectors, ALD alumina is used to tailor resistance and SEE properties of large-area borosilicate glass capillary arrays for microchannel plats (MCP) based detectors with high gain and low noise (see Section 2.2.1). With micrometer-level spatial imaging and time resolutions below 10 ps MCPs offer a powerful replacement for PMTs.

ALD alumina is an attractive material for fabrication of large suspended membranes, and thus of high relevance for the application in tynodes. Chemical inertness of alumina to some common cleanroom etchants (dry etching chemistry in particular) is of great importance during the release of membranes. Nanocorrugated suspended alumina membranes have been fabricated on top of Si nanograss and a monolayer of self-aligned polymeric nanobeads [16]. Realization of smooth rectangular membranes in

sizes up to a cm in edge length is reported in the same study. Recently, a formation of large free-standing 25 nm-thick ALD alumina plates consisting of honey-comb cells is described in [17].

4.2.1. DEPOSITION METHOD

In this study, alumina layers are deposited using a thermal process in an ASM F-120 flow-type reactor. Trimethylaluminium ($Al(CH_3)_3$, TMA), supplied by Sigma Aldrich and kept in a stainless steel container was used as reactant, whereas water was employed as oxidizer. Both precursors are kept at 22 °C. Growing of film is carried out at the pressure of 1 Torr, with a constant nitrogen flow of 500 sccm. Temperature of the ALD growth is varied in the range from 100 to 300 °C. The schematic of the used ALD reactor is shown in Figure 4.2a, and a photo of ALD system employed in this work is shown in Figure 4.2b.

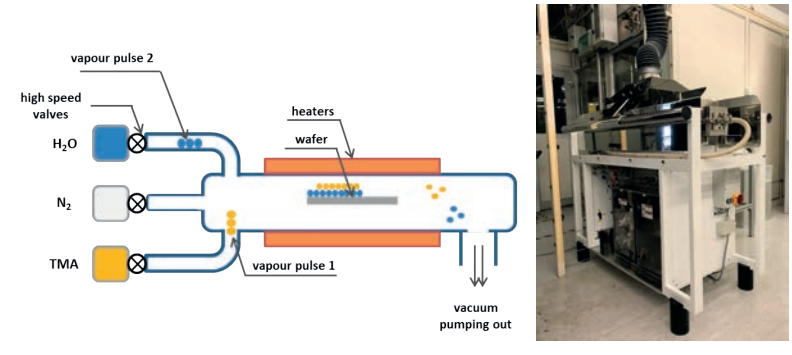

(a) (b)

Figure 4.2: A schematic diagram of a thermal ALD system and precursors used in the growth of alumina (a), and a photo of the in-house ASM F-120 ALD reactor used for the deposition of alumina layers in this study (b).

For thermal ALD of alumina TMA and water are used as metal and oxygen source, respectively. TMA is a thermally stable high vapour pressure liquid at room temperature which, after being introduced to the deposition chamber, easily reacts with hydroxyl groups. These groups must be present on the surface in order for the ALD growth to be initialized (Figures 4.3a and 4.3b). After this reaction is completed, unreacted precursor and methane as a by-product are purged away by nitrogen, in a 6 s long step (Figure 4.3c). Next, the reactant (water) is introduced in the chamber (1 s) and its reaction with methyl sites takes place (Figure 4.3d). The term “reactant” instead of “second precursor” is often used for the ALD agent that leads to oxidation. This is followed by another 6 s long purging step (Figures 4.3e). As a result, no mixing of the two precursors occurs in the gas phase, which eliminates incorporation of carbon impurities originating from TMA in ALD films. In each cycle one (sub)monolayer of ALD film is grown, where cycle is defined as a process of sequential pulsing of two precursor gasses and purging times in between (steps b – e in Figure 4.3) These reactions are widely studied and mapped out for different substrates in other reports [10] [18] [19].

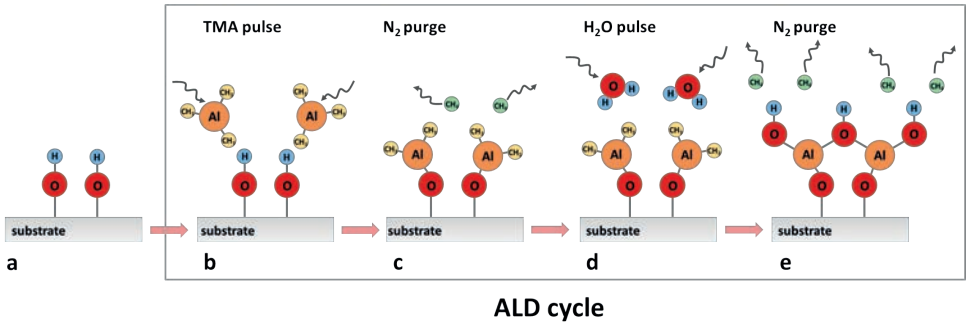

Figure 4.3: ALD of Al_2O_3 conducted in this study. For the initialization of the growth, the substrate must contain OH surface groups (a) which are reacting with TMA molecules (b). One ALD cycle is accomplished in a sequence 1 s – 6 s – 1 s – 6 s, with pulsing time of TMA (b), N_2 (c), H_2O (d) and N_2 (e), respectively.

4.2.2. FABRICATION OF ALUMINA TYNODES

The fabrication of alumina tynodes is conducted using the same set of photomasks as in previously described process flow for SiN tynodes (see the Section 3.2.2. Identical to the steps reported there, 500 nm of thermal oxide is grown on the silicon substrate wafers, on top of which the same thickness of low-stress SiN ("Type 1") is deposited (Figure 4.4a) to serve as a support grid for the array of tynodes. Wells in the SiN layer are formed in dry etching process (Figure 4.4b). The underlaying oxide film is partially consumed in this step. In order to reduce the surface roughness resulting from dry etching, wafers are immersed in BHF 1:7 solution for 15 sec. By smoothening the surface, we ensured a safer release of the tynodes in the later stage of the fabrication.

Next, the substrate patterned in this way is covered by a layer of ALD alumina, in the reactor and process described in the previous section. For the purpose of the tynode fabrication, the process temperature was kept at 300 °C, since for the chosen substrate we were not limited by a thermal budget. The number of cycles is varied from 55 to 500, for the deposition of layers with thicknesses from of 5 to 50 nm, respectively. In order to avoid any possible thinning down or degradation of the very thin alumina films during the remaining processing steps (e.g. to avoid the risk of consumption of the film in cleaning procedures or any potential scratching), the alumina layer was capped with 1 µm of PECVD oxide. 3 µm-thick PECVD oxide is added on the backside of wafer to serve as a hard mask material for the removal of Si substrate (Figure 4.4c).

Large windows on the backside of the wafers were then opened by etching the silicon substrate in a deep reactive ion etching (DRIE) process (Figure 4.4d). In parallel, additional lines are etched to facilitate manual dicing of the wafers into 2×2 cm^2 large chips. Final release of the tynodes was carried out by removing the sacrificial oxide layers in an HF vapour chamber (Figure 4.4e). For the removal of the oxide layer on both sides of the alumina tynodes we applied 4 to 5 etching cycles, each 10 min long, at 125 Torr, with

steps for chamber purging in between. Flows of HF and ethanol were 190 scccm and 210 sccm, respectively. For these conditions, the calculated selectivity between thermal and PECVD oxide was 1:35. Alumina is known for being an excellent protective layer during HF vapour etching. As a test, a wafer with a 5 nm-thick ALD alumina film deposited on top of 100 nm thermal oxide was exposed to 60 min-long etching, after which no change in the thickness or pinholes were observed. Figure 4.5 shows an SEM image of a 15 nm-thick alumina tynode after release and sputtering 2 nm of TiN as a conductive layer required to reduce charging up. Unlike the procedure conducted for SiN tynodes, a conductive layer in this process is applied on the opposite side of chip, in the cavity formed by DRIE.

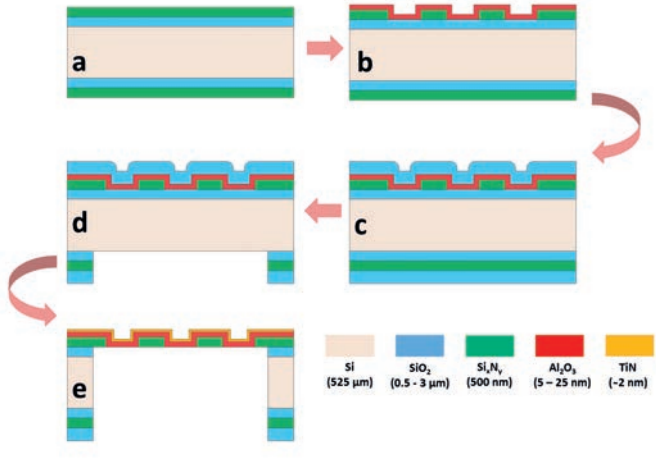

Figure 4.4: MEMS fabrication of alumina tynodes with assigned thicknesses of utilized films.

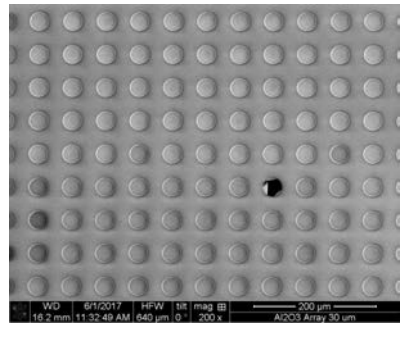

Figure 4.5: SEM image of 10 nm-thick alumina tynodes with a diameter of 30 µm. Only a few broken single membranes were observed in an array with a size 64 × 64.

4.3. RESULTS

In the following section the Al_2O_3 tynode performance, in relation to the properties of interest for TiPC and other possible MEMS applications, is compared and discussed. In the envisioned further optimization of the TiPC operation, focusing of secondary electrons along the stack of the tynodes is a desirable capability. This can be achieved using lens-shaped tynodes, which could be fabricated by using reflowed photoresist as a substrate for the growth of the tynode material. This requires a low temperature deposition process of the tynode material. Such a demand cannot be met by LPCVD, but the nature of ALD, in contrast, allows forming films of a high quality even at a room temperature. With this aim, attributes of ALD alumina grown at temperatures of down to 100 °C were explored. In addition, the thickness of the tynodes is varied, as one of the key factors in the secondary electron emission.

4.3.1. RESIDUAL STRESS

We evaluated the stress of alumina films grown during 1000 cycles in the temperature range from 100 to 300 °C (Figure 4.6). Longer depositions are performed for this investigation in order to avoid measurement error which could arise for very thin layers. The film present on the back side of the wafer was removed prior to the curvature measurement, either in BHF solution while the front side was protected with photoresist, or by a dry etching method using boron trichloride (BCl_3). The stress is calculated as averaged value out of five subsequent measurements at a fixed position of a wafer on the holder in Tencor FLX, whereas the vertical bars on Figure 4.6 represent the standard deviation. It was observed that tensile stress gradually increased from 125 to 565 MPa for decreasing temperature in the investigated domain. This result is in line with other reports on thermo-mechanical properties of ALD alumina [20] [21] [22]. Having this aspect in mind, we conclude that ALD alumina is a more advantageous choice than LPCVD Si_xN_y for the MEMS fabrication of tynodes, as stress of the same magnitude is obtained at significantly lower deposition temperatures (see results reported in Section 3.4.1). Due to this, manufacturing of membranes with much larger areas is allowed - namely, we successfully fabricated the 50 nm-thick alumina membrane with the size of entire 64×64 tynode array (around 3.5×3.5 mm^2).

The change of stress caused by the sputtering of the TiN layer is investigated on non-patterned alumina films deposited at 300 °C. The presence of 2 nm-thick TiN on top of 100 nm alumina film decreased the wafer curvature and the stress of this bi-layer was found to be 50 MPa lower than the stress of alumina only. Since much thinner alumina was used for the fabrication of tynodes, the same effect is investigated for the combination of 5 nm alumina covered with 2 nm of TiN. Here the induced change of curvature was much larger, and the stress of combination of layers was -225 ± 39 MPa, as opposed to compressive stress of alumina of 243 ± 32 MPa. The stress of TiN alone was found to be -1.7 ± 0.1 GPa. However, sputtering of TiN even on the thinnest produced alumina tynodes did not cause mechanical failure of the dynodes.

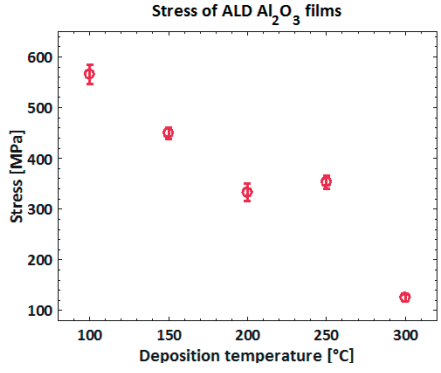

Figure 4.6: Stress of ALD Al_2O_3 films prepared at different process conditions. Stress is investigated for approximately 100 nm-thick layers grown in 1000 cycles. Vertical bars represent the standard deviation calculated out of five subsequent stress measurements for each wafer.

4.3.2. THICKNESS AND OPTICAL PROPERTIES

The growth per cycle (GPC) of ALD alumina in the temperature range 100 – 300 °C is plotted in Figure 4.7 We evaluated films deposited on top of silicon and calculated GPC as average thickness divided by the total number of cycles, which was set to 500 and 1000. The apex in the profile of GPC observed at 200 °C is in accordance with previous studies [23] [24] [25] [26] [27], which showed that at higher temperatures, due to the decrease of OH sites (dehydroxilation) on the surface, the growth is slowed down. At lower temperatures, on the other hand, mass transport drops and reactions between precursor gasses and surface become incomplete. Clearly, films deposited at higher temperatures have a better uniformity of thickness over a wafer, with standard deviation of only 0.347 nm measured after 500 cycles long deposition at 300 °C. Large variations of thickness in the process conducted at temperatures lower than 150 °C suggest that purging times should be longer than 6 s. Investigated growth per cycle values are very close to or slightly lower than for deposition processes reported elsewhere (see Table 4.1).

Deposition temperatures close to 200 °C provide the fastest growth, in agreement with all other studies on ALD of alumina with similar process parameters. Higher values of GPC obtained for longer depositions (1000 cycles) indicate a delay of a homogeneous growth. This incubation period is difficult to be evaluated by ex-situ ellipsometry analysis. Also, it should be discerned that as native oxide was not taken into account, the true thickness of ALD alumina is somewhat lower for the observed growth on Si substrate. In study by Groner et. al. [9] around 0.2 nm of interfacial SiO_2 was determined to be present in between Si and alumina.

The effect of deposition temperature on the refractive index at 633 nm is shown on Figure 4.8. The refractive index is around 1.65 at 300 °C and it drops with decreasing temperature. Its sharper reduction at temperatures below 200 °C may be caused by the presence of carbon and hydrogen impurities coming from TMA in these films, as suggested in [10].

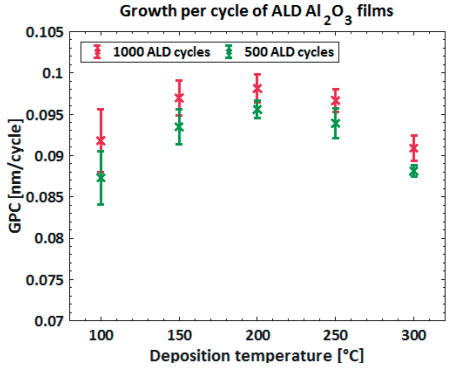

Figure 4.7: Growth per cycle (GPC) of ALD alumina films in the temperature range 100 – 300°C. Films were grown during 500 (green markers) and 1000 (red markers) ALD cycles. Vertical bars represent the standard deviation in GPC, calculated from 13 data points across 4-inch wafers.

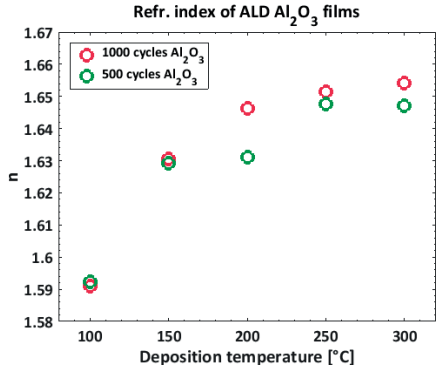

Figure 4.8: Refractive index of ALD alumina at the wavelength of 633 nm. Films, approximately 50 and 100 nm-thick, were grown in 500 and 1000 cycle-long processes, respectively.

4.3.3. ELEMENTAL COMPOSITION

Spectrum in the "bulk" of alumina films (thus, away from the surface) obtained by XPS (Figure 4.9) reveals the presence of aluminium and oxygen, as expected. Since the carbon peak (C 1s) was not detected in all of the prepared samples, we analysed data without normalization of XPS plots . Zoom-in of Al 2p region indicates symmetry in the shape of these peaks, but with a drop in the intensity of the film prepared at 100 °C, suggesting a somewhat lower aluminium amount. On the other hand, we observed broadening and displacement towards lower energies for O 1s peaks attributed to temperatures of 150 and 100 °C, which indicates the presence of hydroxyl and/or carbon related bonds in the material. This observation is in line with other reports on similarly conditioned ALD processes [24] [27] . Nevertheless, materials prepared at temperatures in the 150 – 300 °C range display a good stoichiometry, with "in-bulk" oxygen to aluminium elemental ratio of 1.49 – 1.50 (Figure 4.10). We determined this parameter from the narrow XPS acquisition around Al 2p and O 1s peaks and proved that these films are indeed stoichiometric

Number of cycles	GPC (nm/cycle)	Refractive index	Deposition temperature (°C)	Reference
2730	0.11	1.666	300	[2]
n.a.	0.09	n.a.	220	[15]
800	0.14	1.61 – 1.66	150	[24]
	0.15	1.63 – 1.69	175	
n.a.	0.08	n.a.	100	[25]
	0.10		200	
	0.09		300	
n.a.	0.09	1.60	100	[26]
	0.11	1.63	200	
	0.10	1.64	300	
n.a.	0.08	1.64	200	[27]
500	0.088	1.651	100	This work
	0.089	1.648	150	
	0.095	1.631	200	
	0.093	1.629	250	
	0.087	1.592	300	
1000	0.092	1.591	100	This work
	0.097	1.631	150	
	0.098	1.646	200	
	0.097	1.652	250	
	0.091	1.654	300	

Table 4.1: Overview of literature results on growth per cycle and refractive index of ALD alumina films prepared at different temperatures and data from films used in this study.

(Al_2O_3). On the other hand, O:Al ratio elevated to 1.60 for the growth temperature of 100 °C. Moreover, this is the only film containing carbon impurities, which also affected the profile of its O 1s peak (Table 4.2). For deposition of pure films below this temperature, PEALD with O_2 or O_3 [5] [28] [29] may be pursued. Namely, ALD in which water (or H_2O_2, alternatively [30]) is used as the oxidant is not adequate for the deposition of stoichiometric oxide films and the thickness uniformity is degraded due to the condensation of water vapour at temperatures much lower than 100 °C. Oxygen plasma, on the contrary, is sufficiently reactive with the surface methyl groups down to room temperatures [31].

4.3.4. SURFACE MORPHOLOGY

Atomic force microscopy analysis of ALD alumina shows that the surface of the films is very smooth, uniform and without hillocks formation. Scanning over $0.5 \times 0.5\ \mu m^2$ area of alumina samples reveals that lowering the deposition temperature does not affect the surface morphology. Root mean square (RMS) roughness of a film prepared at 100 °C (Figure 4.11a) is only 0.05 nm higher than the layer formed during the same number of reaction cycles at 300 °C (Figure 4.11b). The RMS roughness of 0.25 nm measured for our alumina layers is even lower than previous investigations where it was reported to be between 0.5 and 2 nm [4] [9]. The amorphous structure of alumina films was not confirmed by XRD analysis in this work, but according to other studies crystallization

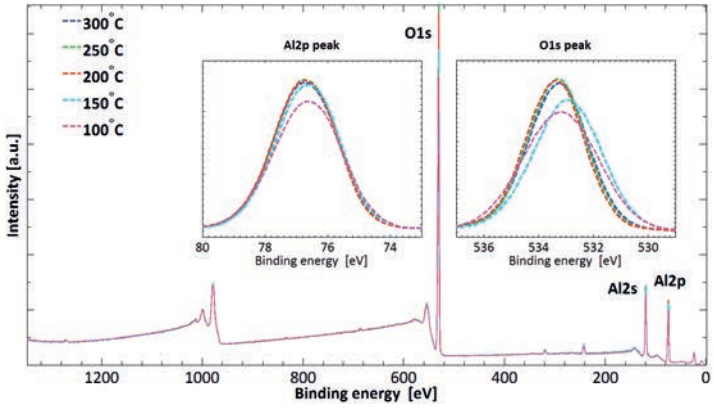

Figure 4.9: XPS survey spectra of alumina films deposited at temperatures in the range from 100 to 300 °C. Layers are grown on top of a Si substrate in a 1000 cycles long process. Detailed regions around Al 2p (left plot) and O 1s (right plot) peaks are not plotted in identical scaling.

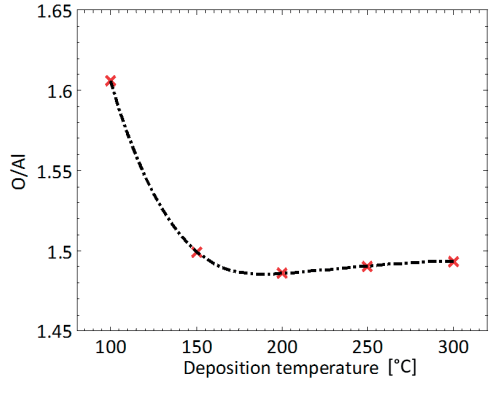

Figure 4.10: Oxygen-to-aluminium elemental ratio in ALD alumina films. Values are calculated using the total surface under Al 2p and O 1s peaks, including the contribution of C-O bonds for deposition temperature of 100°C.

of Al_2O_3 occurs only during thermal annealing at temperatures higher than 900 °C [32]. In conclusion, AFM investigation discloses adequacy of ALD alumina for the fabrication of smooth tynodes for the TiPC application. Furthermore, we observed that the previously described adjustment of deposition parameters has a marginal influence on surface roughness.

4.3.5. SECONDARY ELECTRON EMISSION

Atomic layer deposited alumina tynodes with thicknesses in the range 5 – 50 nm were subjected to SEY characterization by using the method described in Section 3.3.7. For

Deposition temperature (°C)	Al 2p (%)	O 1s (%)	C 1s (%)	Peak position (eV) / FWHM (eV) Al 2p	O 1s	C 1s
100	37.04	59.48	1.51	76.77 / 2.82	533.16 / 3.42	285.07 / 3.79
150	39.42	59.11	/	76.78 / 1.79	532.98 / 3.16	/
200	39.38	58.52	/	76.85 / 2.65	533.29 / 2.79	/
250	39.55	58.95	/	76.83 / 2.64	533.24 / 2.82	/
300	39.54	59.05	/	76.83 / 2.67	533.21 / 2.88	/

Table 4.2: Information on relevant peaks and atomic content of the studied films, obtained from in-depth XPS survey. The remaining portion, usually around 1.45%, origins from Ar used in the ion beam etching of the material. For this characterization we used alumina films deposited during 1000 cycles on top of bare silicon. Since carbon was not present in all of prepared samples, plots were not normalized.

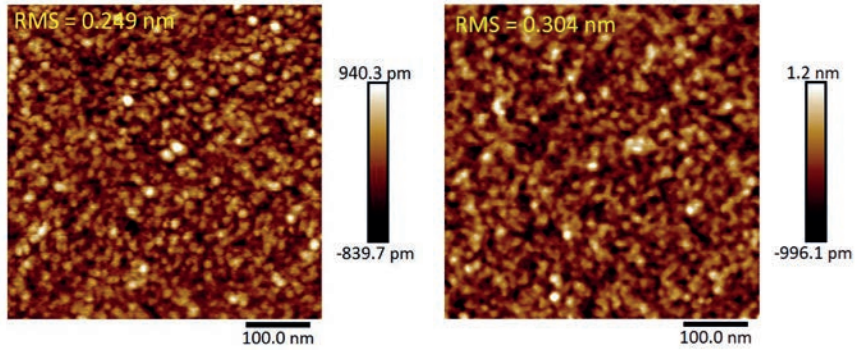

(a) (b)

Figure 4.11: AFM images revealing the smooth surface of the deposited aluminum layers. Micrographs are recorded over a 0.5×0.5 µm^2 region of 50 nm-thick ALD alumina layers grown at 300 (a) and 100 °C (b). Both films were deposited on top of bare Si substrate.

this characterization we used rectangular test ALD alumina tynodes with sizes up to 200×200 µm^2. The fabrication of these membranes is simpler than the process illustrated in Figure 4.4, as it requires only one photomask for the backside opening on the wafer and excludes a deposition and patterning of the SiN support mesh (see Figures 12 and 13 in reference [33]). Outcome of this analysis is presented in Figure 4.12 and includes only the total reflection and transmission yields (REY and TEY). The survey confirmed that TiPC may benefit more from the alumina as material than the previously investigated Si_xN_y. The sample with the best performance was a 10 nm-thick alumina tynode with TEY of 2.6. Moreover, these samples were more sensitive at lower energies, which is of a great importance for our application. Next, we detected that TEY peak drops and shifts towards higher energies for the thicker alumina tynodes. Still, even 50 nm-thick alumina membranes are a more efficient secondary electron source than silicon nitride samples with thicknesses of 40 nm. Furthermore, we succeded in the release of a very large (3.5×3.5 mm^2) 50 nm-thick alumina membrane without suspending SiN mesh, which greatly simplifies the fabrication flowchart. Further optimization is required to determine the minimum thickness of alumina which allows fabrication of such

large free-standing membranes. The low emission obtained for 5 nm-thick alumina tynode suggests that the yield in this case is predominantly governed by forward scattered electrons and that a somewhat thicker film is required for a more productive generation of secondary electrons.

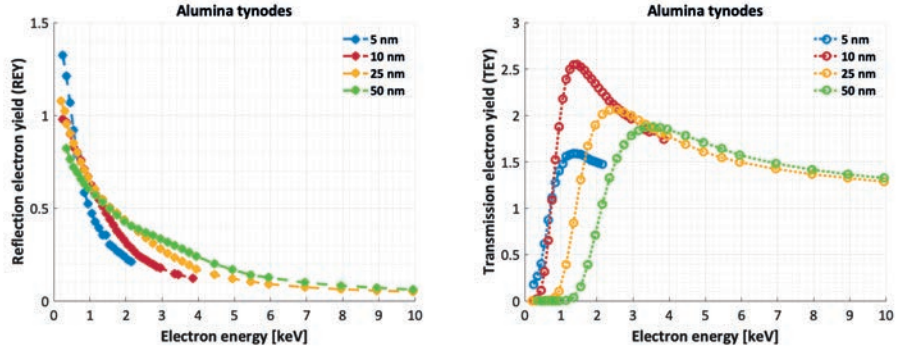

(a) (b)

Figure 4.12: Total reflection (a) and transmission (b) electron yields of ALD alumina tynodes with thicknesses in the range from 5 to 50 nm. A conductive 5 nm-thick TiN film was sputtered on the backside of the membranes to prevent charging up.

4.4. CONCLUSIONS

MECHANICAL and structural properties of the studied ALD alumina films showed that they are a good candidate for the fabrication of strong, homogenous membranes. All films, grown in the temperature range from 100 to 300 °C, exhibit low tensile stress, high uniformity in thickness, absence of impurities and remarkably smooth surface. In light of the results obtained in the study on LPCVD SiN films, ALD method proved to have two outstanding advantages – it allows formation of high quality films that are even thinner than those obtained with LPCVD procedure, and at much lower temperatures. Thinner tynodes are required for the detection of low energetic photoelectrons in the TiPC, whereas the low-temperature deposition is generally desired since it provides a higher degree of freedom in MEMS processing. Finally, with a dedicated multi-electrode setup in SEM, we demonstrated that alumina is a more efficient secondary electron emitter, with a TEY of 2.6 for the 10 nm-thick tynode, in contrast to the value of around 1.6 obtained for 40 nm-thick silicon nitride tynode. Further improvement of SEY can be achieved by investigating proper surface termination which may introduce negative electron affinity, in situ surface cleaning of tynodes during the measurement procedure, and by adjusting the shape of the membranes for the focusing of secondary electrons. As demonstrated in this Chapter, ALD has the ability to provide good-quality films with thicknesses of only a few nanometers, and at a reasonably low temperatures which allows coating of thermally sensitive substrates. Due to these features, ALD is a more convenient deposition technique for the tynodes than previously assessed LPCVD. Therefore, ALD will remain the choice of deposition for the following

tynode material being investigated - magnesium oxide (MgO).

REFERENCES

[1] T. Suntola and J. Antson. Method for producing compound thin films, November 15 1977. US Patent 4,058,430.

[2] M. Ritala, M. Leskelä, J-P. Dekker, C. Mutsaers, P.J. Soininen, and J. Skarp. Perfectly conformal TiN and Al_2O_3 films deposited by atomic layer deposition. *Chemical Vapor Deposition*, 5(1):7–9, 1999.

[3] K. Grigoras, V-M. Airaksinen, and S. Franssila. Coating of nanoporous membranes: atomic layer deposition versus sputtering. *Journal of nanoscience and nanotechnology*, 9(6):3763–3770, 2009.

[4] M.D. Groner, F.H. Fabreguette, J.W. Elam, and S.M. George. Low-temperature Al_2O_3 atomic layer deposition. *Chemistry of materials*, 16(4):639–645, 2004.

[5] A. Niskanen, K. Arstila, M. Ritala, and M. Leskelä. Low-temperature deposition of aluminum oxide by radical enhanced atomic layer deposition. *Journal of The Electrochemical Society*, 152(7):F90–F93, 2005.

[6] O.M.E. Ylivaara, L. Kilpi, X. Liu, S. Sintonen, S. Ali, M. Laitinen, J. Julin, E. Haimi, T. Sajavaara, H. Lipsanen, and et. al. Aluminum oxide/titanium dioxide nanolaminates grown by atomic layer deposition: Growth and mechanical properties. *Journal of Vacuum Science & Technology A: Vacuum, Surfaces, and Films*, 35(1):01B105, 2017.

[7] H.B. Profijt, S.E. Potts, M.C.M. Van de Sanden, and W.M.M. Kessels. Plasma-assisted atomic layer deposition: basics, opportunities, and challenges. *Journal of Vacuum Science & Technology A: Vacuum, Surfaces, and Films*, 29(5):050801, 2011.

[8] M.S. Oh, K. Lee, J.H. Song, B.H. Lee, M.M. Sung, D.K. Hwang, and S. Im. Improving the gate stability of ZnO thin-film transistors with aluminum oxide dielectric layers. *Journal of the Electrochemical Society*, 155(12):H1009–H1014, 2008.

[9] M.D. Groner, J.W. Elam, F.H. Fabreguette, and S.M. George. Electrical characterization of thin Al_2O_3 films grown by atomic layer deposition on silicon and various metal substrates. *Thin Solid Films*, 413(1-2):186–197, June 2002.

[10] O.M.E. Ylivaara, X. Liu, L. Kilpi, J. Lyytinen, D. Schneider, M. Laitinen, J. Julin, S. Ali, S. Sintonen, M. Berdova, and et. al. Aluminum oxide from trimethylaluminum and water by atomic layer deposition: The temperature dependence of residual stress, elastic modulus, hardness and adhesion. *Thin Solid Films*, 552:124–135, February 2014.

[11] H. Klumbies, P. Schmidt, M. Hähnel, A. Singh, U. Schroeder, and et. al. Thickness dependent barrier performance of permeation barriers made from atomic layer deposited alumina for organic devices. *Organic Electronics*, 17:138–143, February 2015.

[12] S. J. Yun, Y-W. Ko, and J.W. Lim. Passivation of organic light-emitting diodes with aluminum oxide thin films grown by plasma-enhanced atomic layer deposition. *Applied Physics Letters*, 85(21):4896–4898, November 2004.

[13] J.A. van Delft, D. Garcia-Alonso, and W.M.M. Kessels. Atomic layer deposition for photovoltaics: applications and prospects for solar cell manufacturing. *Semiconductor Science and Technology*, 27(7):074002, June 2012.

[14] T. M. Mayer, J. W. Elam, S. M. George, P. G. Kotula, and R. S. Goeke. Atomic-layer deposition of wear-resistant coatings for microelectromechanical devices. *Applied Physics Letters*, 82(17):2883–2885, April 2003.

[15] K. Grigoras, L. Sainiemi, J. Tiilikainen, A. Säynätjoki, V-M. Airaksinen, and S. Franssila. Application of ultra-thin aluminum oxide etch mask made by atomic layer deposition technique. *Journal of Physics: Conference Series*, 61:369–373, March 2007.

[16] L. Sainiemi, K. Grigoras, and S. Franssila. Suspended nanostructured alumina membranes. *Nanotechnology*, 20(7):075306, January 2009.

[17] K. Davami, L. Zhao, E. Lu, J. Cortes, C. Lin, D.E. Lilley, P.K. Purohit, and I. Bargatin. Ultralight shape-recovering plate mechanical metamaterials. *Nature Communications*, 6(1), December 2015.

[18] H.M.T. Nguyen, H-Y. Tang, W-F. Huang, and M.C. Lin. Mechanisms for reactions of trimethylaluminum with molecular oxygen and water. *Computational and Theoretical Chemistry*, 1035:39–43, May 2014.

[19] A.C. Dillon, A.W. Ott, J.D. Way, and S.M. George. Surface chemistry of Al_2O_3 deposition using $Al(CH_3)_3$ and H_2O in a binary reaction sequence. *Surface Science*, 322(1-3):230–242, January 1995.

[20] A.U. Mane, Q. Peng, J.W. Elam, D.C. Bennis, C.A. Craven, M.A. Detarando, J.R. Escolas, H.J. Frisch, S.J. Jokela, J. McPhate, M.J. Minot, and et. al. An atomic layer deposition method to fabricate economical and robust large area microchannel plates for photodetectors. *Physics Procedia*, 37:722–732, 2012.

[21] M.K. Tripp, C. Stampfer, D.C. Miller, T. Helbling, C.F. Herrmann, C. Hierold, K. Gall, S.M. George, and V.M. Bright. The mechanical properties of atomic layer deposited alumina for use in micro- and nano-electromechanical systems. *Sensors and Actuators A: Physical*, 130-131:419–429, August 2006.

[22] D.C. Miller, R.R. Foster, S-H. Jen, J.A. Bertrand, S.J. Cunningham, A.S. Morris, Y-C. Lee, S.M. George, and M.L. Dunn. Thermo-mechanical properties of alumina films created using the atomic layer deposition technique. *Sensors and Actuators A: Physical*, 164(1-2):58–67, November 2010.

[23] R.L. Puurunen, J. Saarilahti, and H. Kattelus. Implementing ALD layers in MEMS processing. *ECS Transactions*, 11(7):3–14, 2007.

[24] M.T. Aguilar-Gama, E. Ramírez-Morales, Z. Montiel-González, A. Mendoza-Galván, M. Sotelo-Lerma, P.K. Nair, and H. Hu. Structure and refractive index of thin alumina films grown by atomic layer deposition. *Journal of Materials Science: Materials in Electronics*, 26(8):5546–5552, June 2014.

[25] J.L. van Hemmen, S.B.S. Heil, J.H. Klootwijk, F. Roozeboom, C.J. Hodson, M.C.M. van de Sanden, and W.M.M. Kessels. Plasma and thermal ALD of Al_2O_3 in a commercial 200 mm ALD reactor. *Journal of The Electrochemical Society*, 154(7):G165, 2007.

[26] J.M. Rafi, M. Zabala, O. Beldarrain, and F. Campabadal. Deposition temperature and thermal annealing effects on the electrical characteristics of atomic layer deposited Al_2O_3 films on silicon. *Journal of The Electrochemical Society*, 158(5):G108, 2011.

[27] J. Haeberle, K. Henkel, H. Gargouri, F. Naumann, B. Gruska, M. Arens, M. Tallarida, and D. Schmeißer. Ellipsometry and XPS comparative studies of thermal and plasma enhanced atomic layer deposited Al_2O_3 films. *Beilstein Journal of Nanotechnology*, 4:732–742, November 2013.

[28] S.K. Kim, S.W. Lee, C.S. Hwang, Y-S. Min, J.Y. Won, and J. Jeong. Low temperature (100 °C) deposition of aluminum oxide thin films by ALD with O_3 as oxidant. *Journal of The Electrochemical Society*, 153(5):F69, 2006.

[29] J.B. Kim, D.R. Kwon, K. Chakrabarti, C. Lee, K.Y. Oh, and J.H. Lee. Improvement in Al_2O_3 dielectric behavior by using ozone as an oxidant for the atomic layer deposition technique. *Journal of Applied Physics*, 92(11):6739–6742, December 2002.

[30] J. Fa Fan and K. Toyoda. Growth-temperature dependence of the quality of Al_2O_3 prepared by sequential surface chemical reaction of trimethylaluminum and H_2O_2. *Japanese Journal of Applied Physics*, 32(Part 2, No. 9B):L1349–L1351, September 1993.

[31] S.E. Potts, W. Keuning, E. Langereis, G. Dingemans, M.C.M. van de Sanden, and W.M.M. Kessels. Low temperature plasma-enhanced atomic layer deposition of metal oxide thin films. *Journal of The Electrochemical Society*, 157(7):P66, 2010.

[32] S. Jakschik, U. Schroeder, T. Hecht, M. Gutsche, H. Seidl, and J.W. Bartha. Crystallization behavior of thin ALD-Al_2O_3 films. *Thin Solid Films*, 425(1-2):216–220, February 2003.

[33] H. van der Graaf, H. Akhtar, N. Budko, H.W. Chan, C.W. Hagen, C.C.T. Hansson, G. Nützel, S.D. Pinto, V. Prodanović, B. Raftari, and et. al. The tynode: A new vacuum electron multiplier. *Nuclear Instruments and Methods in Physics Research Section A: Accelerators, Spectrometers, Detectors and Associated Equipment*, 847:148–161, 2017.

5

ATOMIC LAYER DEPOSITED MAGNESIUM OXIDE TYNODES

As indicated in Chapter 4, ALD provides accurate control over film thickness, which is one of main demands in the realization of tynodes with thicknesses in the range of a few nanometers. Magnesium oxide (MgO) has been extensively investigated for its efficient SEE properties, and in this chapter we report on the applicability of ALD MgO as a tynode material and a potential replacement of the previously analysed ALD Al_2O_3. After introducing growth of MgO by ALD, we illustrate the process steps used for the fabrication of the tynodes. Large-area arrays of tynodes with thicknesses in the range of 5 – 25 nm are manufactured and characterized in terms of chemical, mechanical and structural properties. SEE analysis is performed in order to determine the optimal thickness for application of these films in TiPC.

In order to determine how the applied MEMS technology reflects on the SEE, the final steps in the fabrication of the tynodes are replicated on ALD MgO films deposited on a Si substrate, after which their reflective SEE (RSEE) is evaluated. Clearly, this approach only indicates if the transmission SEE (TSEE) of the tynodes is improved or reduced, but does not directly provide a quantification of TSEE. Apart from the deposition and subsequent removal of the protection oxide layers, as-deposited MgO films are subjected to thermal treatments in the temperature range from 700 to 1100 °C. Here also, the structural, chemical and morphological characterization of MgO films is presented and brought into relation with their SEE properties.

Parts of this Chapter have been published in: "Effect of thermal annealing and chemical treatments on secondary electron emission properties of atomic layer deposited MgO", *Journal of Vacuum Science Technology A*, 36, 06A102, 2018, and "Ultra-thin ALD MgO membranes as MEMS transmission dynodes in a TImed Photon Counter", *Proceedings of the 2017 IEEE 30th International Conference on Micro Electro Mechnanical Systems (MEMS)*, p. 740 – 743, 2017.

5.1. MAGNESIUM OXIDE (MGO)

DUE to its wide band gap (Eg ~ 7.8 eV), dielectric properties, as well as chemical and thermodynamic stability, MgO has been used in diverse applications, such as spintronics, where it proved to be a very efficient tunnel barrier in magnetic tunnel junctions [1]. MgO is employed as a stable buffer layer in high-temperature superconductors [2] and as an excellent substrate for waveguides made from ferroelectric thin films (barium titanate, $BaTiO_3$, in particular), where its relatively low refractive index (n = 1.72 at 1 μm) minimizes the optical losses [3]. Recent work reports an excellent barrier performance of this material for OLED encapsulation [4]. A notable role of MgO as a protective layer in plasma display panels (PDPs) [5] is ascribed to its high ion-induced SEE coefficient, which reduces the firing voltage and power consumption, accordingly. In parallel, the low sputtering yield of MgO in the presence of glow discharge plasma provides longer lifetime of PDPs (sputtered Mg and O atoms have a great influence on discharge properties when incorporated in plasma as impurities). The SEE mechanism of MgO has been investigated for its applicability in other vacuum electronic devices where electron multiplication is required [6], such as in compact imaging detectors based on microchannel plate photomultiplier tubes (MCP-PMTs). In addition, MgO-based materials are known for their efficient adsorption of CO_2, by which they reduce the emission of greenhouse gasses [7], and can also be used as a part of multicomponent oxides in thin-film gas sensors [8].

5.2. ALD MAGNESIUM OXIDE

MAGNESIUM oxide has been deposited by various physical methods: sputtering, electron beam evaporation, molecular beam epitaxy (MBE), pulsed laser deposition (PLD) and ion-beam assisted deposition (IBAD), as well as chemical processes including spray pyrolysis, chemical vapour deposition (CVD) and liquid phase sol-gel depositions. A detailed overview of procedures to prepare MgO films is given in reference [9]. Atomic layer deposition (ALD), introduced in Section 4.1, is a thin film coating method which offers a high control over thickness and a conformal growth, and has also been explored for the growth of MgO.

ALD of MgO has been demonstrated by using different precursors, and in a large temperature range. Parameters of established ALD processes for the growth of MgO are listed in Table 5.1 together with commonly investigated film characteristics. The first attempts are conducted in the temperature range from 600 to 900 °C, with a metal-organic compound bis(cyclopentadienyl)magnesium ($Mg(Cp)_2$) as Mg source and H_2O as an oxygen source [10]. Later experiments with the same combination of reactants demonstrated the self-limiting ALD process at much lower temperatures [11] [12], down to only 80 °C [13]. Another study [14] reports on MgO growth by sequential exposures of H_2O and bis(ethylcyclopentadienyl)magnesium ($Mg(CpEt)_2$) which is known for the higher volatility compared to $Mg(Cp)_2$. ALD MgO can also be obtained by employing β-diketonate ($Mg(thd)_2$, thd = 2,2,6,6-tetramethyl-3,5-heptadione) as precursor. However, this bulky Mg precursor has a lower reactivity toward H_2O and O_2, as confirmed by significantly lower growth per cycle (GPC) (see Table 5.1), and is usually used together with

ozone (O_3) or hydrogen peroxide (H_2O_2) as oxidizing agents [15] [16].

The most commonly used combination of precursors, $Mg(Cp)_2$ and H_2O, has been employed in this study too. Therefore, the surface reactions in the growth of ALD MgO will be illustrated for this case. As discussed by Putkonen et al. [11], $Mg(Cp)_2$ reacts with hydroxyl groups on Si substrate by forming Si–O–$Mg(Cp)_2$ (Figure 5.1a). Oxidizing reaction after H_2O pulse (Figure 5.1b) results in new OH surface groups. Water is considered to be a mild oxidizer and as such does not decompose the cyclopentadienyl ring, as opposed to O_2 which may break the metal-carbon bond and cause undesirable incorporation of carbon species in the MgO film.

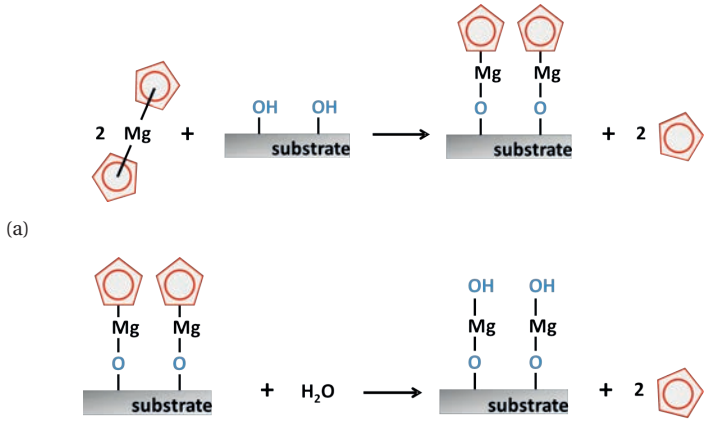

Figure 5.1: Surface reactions in ALD of MgO induced by pulses of $Mg(Cp)_2$ (a) and H_2O (b). Figure adapted from [11].

Precursors	Temperature (°C)	GPC (nm/cycle)	Roughness RMS roughness (nm)	Reference
$Mg(Cp)_2 + H_2O$	600 – 900	0.181 – 0.244	n.a.	[10]
$Mg(Cp)_2 + H_2O$	250	0.156	n.a.	[12]
$Mg(Cp)_2 + H_2O$	200 – 300	0.116	< 250 °C: 2 – 4 nm 250 – 300 °C: 8 – 10 nm	[11]
$Mg(CpEt)_2 + H_2O$	125 – 400	0.07 – 0.142	n.a.	[14]
$Mg(thd)_2 + O_3$	180 – 450	0.022	0.51 – 1.33	[15]
$Mg(thd)_2 + H_2O_2$	325 – 425	0.01	n.a.	[16]
$Mg(Cp)_2 + H_2O$	80 – 350	< 125 °C: 0.11 125 – 225 °C: 0.13	0.3 – 0.86	[13]
$Mg(Cp)_2 + H_2O$	200	0.165	0.38 – 0.42	This work

Table 5.1: ALD of MgO: process conditions and film characteristics versus various types of precursors.

5.3. FABRICATION OF ALD MGO TYNODES

SEVERAL thicknesses were considered to determine the optimal value for the MgO membranes and to investigate its influence on the magnitude and energy dependence of the SEY in the TiPC application. As substrate in the MEMS manufacturing of MgO tynodes, we used 4-inch Si <100> Si wafers, phosphorus-doped (5 – 10 Ω cm) and with a thickness of 525 ± 15 µm. The fabrication procedure of the new tynodes is identical to the one applied for ALD alumina (see Section 4.2.2), the only difference being the applied ALD material. For that reason, the Figure 5.2 gives a simplified version of the flow illustrated in Figure 4.4. An array of 64 × 64 free standing MgO membranes with thicknesses of 5, 15 and 25 nm, diameter of 10 – 30 µm and a center-to-center pitch of 55 µm is embedded in a 500 nm-thick LPCVD SiN and a 500 nm-thick thermal oxide mesh. After dry etching of wells in SiN, the wafers are ready for deposition of the tynode material (Figure 5.2a) on top of silicon oxide. $Mg(Cp)_2$ and H_2O are used as reactants for synthesizing MgO films in a hot wall ALD reactor at 200 °C. The $Mg(Cp)_2$ (purchased from Sigma-Aldrich) was maintained at 80 °C, and deionized H_2O precursor at room temperature. Ultrahigh purity (99.999%) N_2carrier gas flow was set to 300 sccm, providing a background pressure of 1.0 Torr in the reaction chamber, as measured by a MKS Baratron pressure gauge. For the MgO ALD, the precursors $Mg(Cp)_2$ and H_2O were alternately pulsed in the continuous nitrogen carrier flow with the timing sequence: 3 s $Mg(Cp)_2$ dose – 15 s N_2 purge – 1 s H_2O dose – 15 s N_2 purge. As a measure against formation of magnesium-hydroxide during longer exposures to the moist in the air, MgO is encapsulated by 1 µm-thick PECVD oxide (Figure 5.2a). The DRIE of the Si bulk from the wafer backside is applied to define the membranes, and final release of membrane arrays (removal of the top PECVD oxide and bottom thermal oxide layers) is then achieved by utilizing HF vapour with a flow of 190 sccm at 125 Torr (Figure 5.2b). To avoid charging up of the membranes, which would have a negative impact on the precision of SEY characterization, a very thin conductive layer is applied on top of the MgO membranes. In this experiment a 1.8 – 2 nm-thick TiN layer is sputtered on the MgO membranes prior to the SEY measurement. Most of the individual membranes in a tynode remained intact after the final release. In a 64 × 64 array of 5 nm-thick MgO tynode, less than 10 broken membranes were observed (Figure 5.3a), which indicates a remarkable yield in the fabrication process. Moreover, the surface of membranes appears to be flat, with a narrow wrinkled ring located around the edge (less than 2 µm in width), as shown in Figure 5.3b. According to calculations and experimental data on buckling of circular membranes performed by other groups [17], this rim is indeed the region of highest stress in membranes with geometry similar to ours.

5.4. CHARACTERIZATION OF ALD MGO FILMS

5.4.1. THICKNESS, OPTICAL PROPERTIES AND RESIDUAL STRESS

The layer uniformity is evaluated by ellipsometry considering 13 data points across the wafer. The thickness of MgO on Si substrate is (25.53 ± 0.41) nm, with a growth per cycle of 0.165 nm, whereas the refractive index obtained at 633 nm was 1.73. From wafer bow measurements we calculated the residual stress of a 50 nm-thick MgO film to be compressive and equal to (-194.5 ± 10.3) MP, thus with the absolute value very close to data

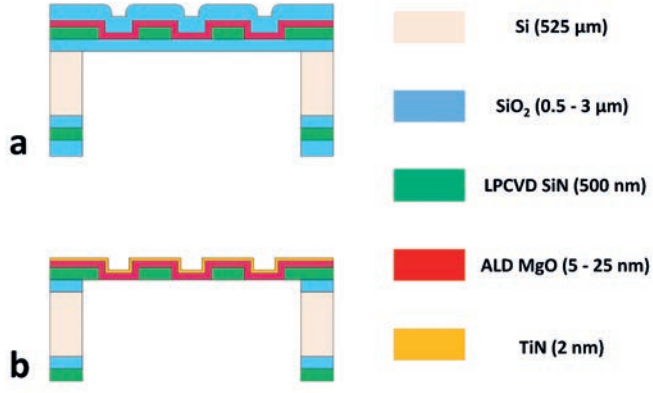

Figure 5.2: Process steps for the fabrication of ALD MgO tynodes: the very thin ALD film is deposited on LPCVD SiN/SiO_2 template and protected additionally by a SiO_2 layer on top. After removal of the Si substrate on the backside by DRIE (a), the capping oxide is gently removed by HF vapour to release the ultra-thin membranes sandwiched between thermal (bottom) and PECVD (top) SiO_2 (b).

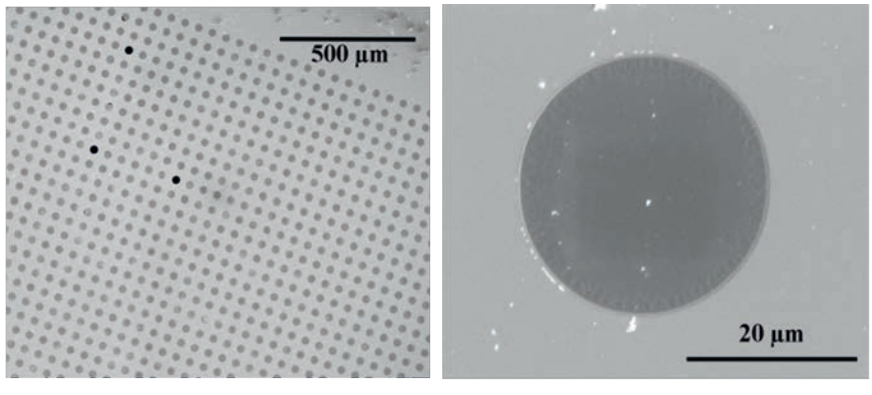

(a) (b)

Figure 5.3: SEM images of 5 nm-thick MgO membranes in 64×64 array (a) and a close-up of a single membrane (b), with a center-to-center distance of 55 µm. Most tynodes remained intact after release, with only couple of ruptured membranes (black spots in image (a)).

measured for ALD Al_2O_3.

5.4.2. ELEMENTAL COMPOSITION

Aging mechanism of MgO films at room temperature has been a subject of numerous studies [18] [19] [20] [21]. This process involves water adsorption on the surface, while MgO is kept at atmospheric conditions, and is less pronounced for materials with (100) crystalline orientation, where less defects are prone to react with water vapor and form

hydroxyl groups. According to Altieri et al. [21], this phenomenon is observed for ultra-thin MgO films in less than an hour after the deposition and saturates in a few hours. As shown in [22], water adsorption is more pronounced for non-stoichiometric MgO films which are oxygen deficient. Storing of MgO films under vacuum conditions is suggested to inhibit the material aging. In this work, however, an encapsulating layer on top of MgO film is applied as a countermeasure against the degradation of its surface. Moreover, this solution contributed to the safe final release of the tynodes (as mentioned in Section 5.3).

MgO films employed in the XPS investigation are grown on Si substrate and, for the abovementioned reason, coated by 1 µm of PECVD oxide. The encapsulation of the samples was performed approximately within a week after the MgO growth, due to shipping time from ALD facilities (Argonne National Laboratory, IL, USA) to the site of further processing (TU Delft, NL). Prior to the analysis, the capping film was removed in HF vapour (details on this procedure will follow in Section 5.5). Due to the exposure of MgO to HF vapour, XPS survey confirmed the presence of a strong F 1s peak, in addition to the expected Mg and O signals (Figure 5.4). As shown in Figure 5.4a , the XPS scan of Mg 2p region conducted for a 25 nm-thick MgO film consists of two signals. The main peak positioned at 50.08 eV corresponds to Mg–O bonds, whereas the satellite peak at 51.38 eV most likely indicates the formation of $Mg(OH)_{2-x}F_x$. From this result solely, it is not clear whether the adsorption of moisture has already occurred prior to encapsulation or in between the removal of capping layer and XPS analysis. The O 1s peak can be resolved into two components positioned at 530.38 and 532.28 eV, assigned to the oxygen atoms in MgO and the fluorine compound (Figure 5.4b). In-depth XPS spectra of the same regions are presented in Figure 5.4c and Figure 5.4d and witness a significant decrease in the intensity of the fluorine containing fraction. Moreover, we observe a shift in the position of these peaks, which probably implies a change in the concentration of hydroxyl groups and fluorine, as shown in a study by Prescott et al. [23].

In-depth XPS survey during the etch of MgO by ion-sputtering showed that fluorine signal (Figure 5.5a) rapidly vanishes. In parallel, Mg 2p peak (Figure 5.5b) becomes less pronounced and shifts towards lower binding energies. At the etch level where F 1s is no longer detected, the profile of Mg 2p suggests the presence of a low-intensity component in its high-energy tail, which we attribute to Mg-OH bonds only. This leads us to the conclusion that "aging" of MgO is more pronounced than the formation of fluorine compound, at least for the time of exposure to HF vapour (2 – 3 min).

5.4.3. SURFACE MORPHOLOGY

Smoothness of MgO surface is investigated by AFM on released tynodes with a thickness of 25 nm. This measurement too concerns the film which has been treated by HF vapour. The AFM scan is conducted over 0.5×0.5 µm^2 large areas: the supporting grid of the tynode (MgO on top of LPCVD SiN, Figure 5.6a) and the active (free-standing) part (MgO only, as shown in Figure 5.6b). Both regions exhibit very low surface roughness with RMS roughness of around 0.4 nm. In addition, AFM measurements were done on MgO films deposited on top of the Si substrate without encapsulation and revealed RMS roughness of 0.37 nm (Figure 5.14a and Table 5.3) is included in the following section). Hence, the HF vapour step did not affect the height fluctuations of MgO surface features. Putkonen

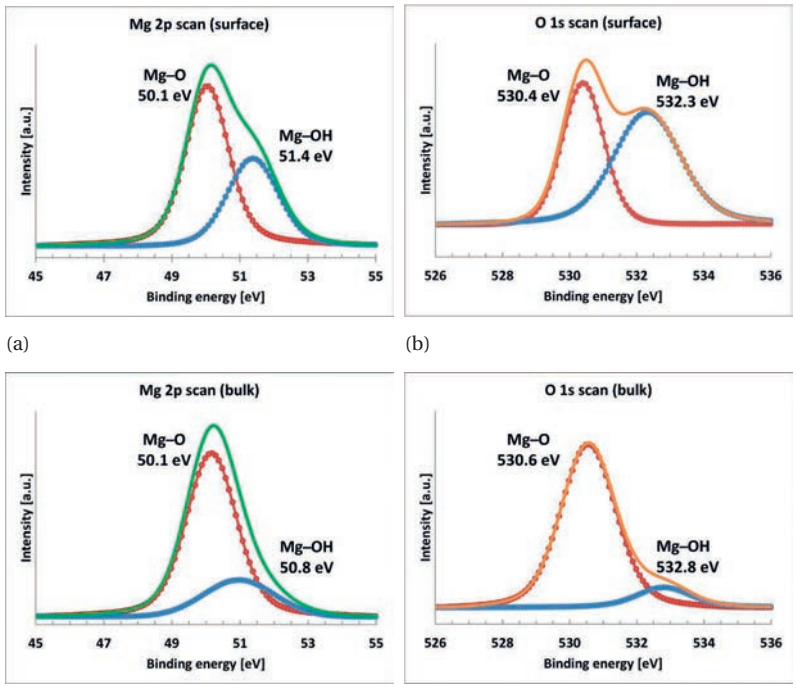

Figure 5.4: XPS surface scans of Mg 2p (a) and O 1s (b) peaks recorded for 25 nm-thick ALD MgO film after the removal of the encapsulating layer. In-bulk spectra of the same regions are plotted in (c) and (d).

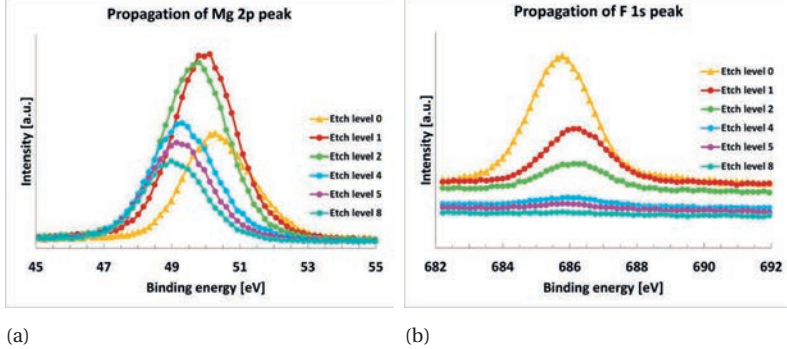

Figure 5.5: F 1s (a) and Mg 2p (b) spectra of ALD MgO films from Figure 5.4, obtained at different level of etching by ion-sputtering.

et al. [11] recorded a surface roughness of 2.4 nm for amorphous MgO grown at 200 °C, which can be attributed to the significantly higher thicknesses of their films (170 nm) in comparison with this study. The drastic increase in roughness (8.2 nm) obtained from layers deposited at 300 °C is ascribed to the emerging crystalline orientations. On the

other hand, our results are in good agreement with the ALD process conducted under similar conditions by Vangelista et al. [13] (see the data summarized in Table 5.1).

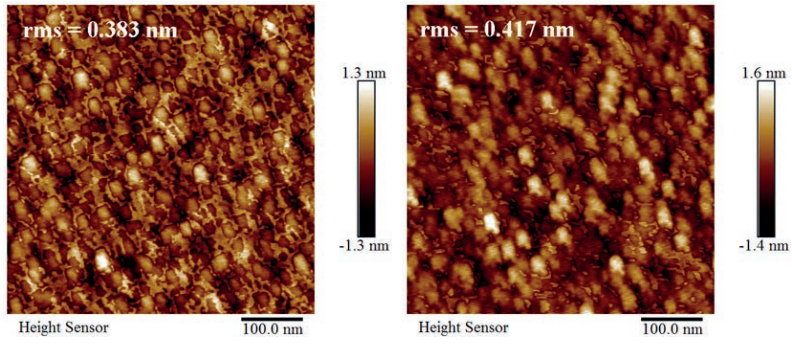

Figure 5.6: AFM images of released 25 nm-thick MgO tynode (a) and MgO on top of the support mesh (b). The size of the scanned area is $0.5 \times 0.5\ \mu m^2$.

5

5.4.4. SECONDARY ELECTRON EMISSION

RSEE

A set of 5, 15 and 25 nm-thick MgO films prepared by ALD is subjected to the RSEE measurements by using the sample-biasing method described in Section 3.3.7. Samples were kept for up to 2 days in ambient conditions prior to this investigation after the removal of the encapsulating film. SEY strongly depends, among other properties, on the thickness of the material. As illustrated in Figure 5.7, the 5 and 15 nm-thick MgO films exhibit a maximum RSEY of 3.3 and 4, respectively, whereas the highest value of 4.8 is recorded for the 25 nm-thick layer. As expected, the energy of primary electrons at which the RSEY peak occurs shifts towards higher values ($E_{PE,max}$ = 350, 500 and 600 eV) as the film thickness increases from 5 to 15 and 25 nm, respectively. Further improvement of the RSEE performance by increasing the thickness is expected, up to the point when it reaches the maximum escape depth. This quantity is a material property, which strongly depends on the film preparation, but the value of 41 nm reported in [24] is indeed higher than the thicknesses investigated here. However, due to the charging up, the method presented here is not suitable for the SEE measurements of thicker films. This limitation is a consequence of the continuous electron beam used in our SEM measurement setup. Another study on ALD MgO films prepared in identical manner reveals similar effect of the thickness on SEE behavior, but with slightly higher values than this work (5 nm-thick MgO displays SEY of around 5) [25]. Such divergence proves a strong dependence of SEY results on the measurement method.

TSEE

The TEY of MgO tynodes of three thicknesses (5, 15 and 25 nm) was also investigated, and its dependence on the thickness is plotted in Figure 5.8. The 5 nm-thick MgO tynode has a TEY of almost 3, higher than for ALD Al_2O_3, which was the best preforming among

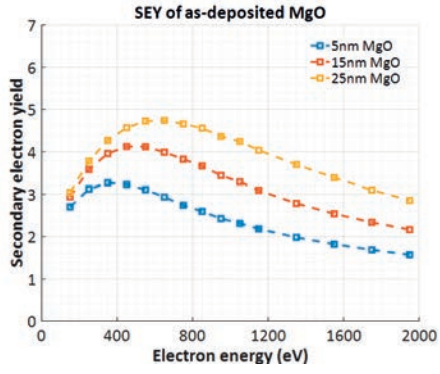

Figure 5.7: Reflective secondary electron yield (RSEY) of MgO films with thicknesses of 5, 15 and 25 nm, deposited on Si.

the previously considered candidates for the TiPC application with a TEY of 2.6 recorded with 10 nm-thick membranes. Charge-up effects were observed after prolonged irradiation of the surface. Therefore, each data point is collected from a different membrane inside the array when the electron energy is increased. Due to such recording the electron yield curve is not as smooth as the measurement of a single large Al_2O_3 membrane (Figure 4.12).

As mentioned before, SEY of investigated material greatly depends on the measurement method. Data set preseneted in Figure 5.8 is obtained by using the DFC setup described in Section 3.3.7. In addition to this standard method, 5 nm-thick MgO tynodes have been subjected to a modified SEY investigation in which semi-spherical collecting grid is replaced by a flat electrode. The distance between the tynode and collector is reduced from a few cm to only 50 µm. Also, we doubled the potential difference between sample and collector by connecting them to -50 and + 50 V, respectively. With these conditions, the resulting TEY was significantly higher, in the range from 4.5 to 5.5, measured for 16 single tynodes at the primary electron energy of 1.2 keV. Larger voltages between the sample and collector (up to 300 V) did not result with even higher values of TEY, which suggests that E-field near the sample surface is not the only factor affecting the measured emission. Most likely, the geometry of the setup plays a more significant role. Namely, flat collector does not capture forward-scattered electrons as efficiently as dome-shaped collector. Thus, forward-scattered electrons are reflected back to the tynode, due to which additional secondary electrons are created. Other strategies in the data collection have been explored as a research within our group, but they are not within the scope of this study.

5.5. ENHANCEMENT OF SEY OF ALD MGO TYNODES

In order to determine how the applied MEMS technology reflects on the SEE, the final steps in the fabrication of the tynodes (Section 5.3) are replicated and tuned on ALD MgO films deposited directly on the Si substrate, after which their reflective SEE (RSEE) is evaluated. Such an approach only indicates if the transmission SEE (TSEE) of the tyn-

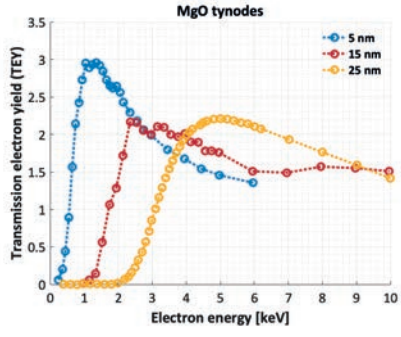

Figure 5.8: Total transmission secondary electron yield of ALD MgO tynodes with different thicknesses versus energy of incoming electrons.

odes is improved or reduced, but does not directly provide a quantification of TSEE. This section reports on four experiments:

5

1. **Experiment 1.** First, we study the effect of two types of oxide used as capping layer to prevent water chemisorption of the MgO layer when exposed to air. The oxide film also protects MgO from dissolving during unavoidable cleaning procedures in the MEMS processing.

2. **Experiment 2.** The etching of this capping layer is performed in HF vapour, to mimic the final tynode release step.

3. **Experiment 3.** As-deposited MgO films are subjected to thermal treatments in the temperature range from 700 to 1100 °C, with the goal to improve SEE by potential crystallization of the films.

4. **Experiment 4.** Thermal treatments are conducted on MgO layers after the deposition and subsequent removal of the capping layer.

In addition to results on the SEE, the structural, chemical and morphological characterization of MgO films is presented and brought into relation with their SEE properties.

5.5.1. PREPARATION OF MGO FILMS

The MgO films with thicknesses of 5, 15 and 25 nm are deposited on 525 ± 15 µm thick Si (100) substrates. $Mg(Cp)_2$ and H_2O are used as reactants for synthesizing MgO films, under process conditions described in Section 5.3. The wafers are stored under vacuum conditions, in order to prevent aging of material, 5 – 7 days after the film growth (due to shipping from a deposition site to the location for further analysis). Unless stated otherwise, longer exposure of films to air is avoided prior to the following post-processing and/or characterization. The first step in a set of experiments was the measurement of SEE of as-deposited films (experiment 1, Figure 5.9). Next, two types of silicon oxide PECVD layers , with the thickness of 1 µm, are employed for the encapsulation of MgO: SiO_x based on silane and on tetraethylorthosilicate (TEOS), both deposited in a multi-chamber Concept One system (Novellus Inc.), at conditions listed in Table 5.2. Deposition times are chosen to to reach the fixed thickness of 1 µm of both oxide films. These

layers are chosen because of their easy removal in HF vapour, which, at the same time, maintains high selectivity towards MgO. In experiment 2, SEE of MgO film is quantified after the top film is removed in HF vapour, by applying etching times of 10 and 40 min for silane and TEOS based layers, respectively. The over-etch (time interval in which MgO film is exposed to HF vapour), was not longer than 2 – 3 min in either case. Next, MgO films are subjected to an annealing step in a furnace under N_2 ambient at 700, 900 or 1100 °C (experiment 3). The samples are heated up from a starting point of 600 °C, with a rate of 10 °C/min, and annealed at the set temperature for 2 hours. After cooling down to 600 °C, the samples are unloaded from the furnace. In addition to experiments 1 – 3, the effect of thermal annealing alone on the properties of MgO films is investigated in experiment 4, under the same conditions applied in experiment 3. This series of steps is illustrated in Figure 5.9, where the points at which SEE analysis is performed, are indicated.

Capping film	Composition gasses	Thickness (µm)	Deposition temperature (°C)	Deposition time (s)
SiO_x	$SiH_4 + N_2O$	1.0	400	120
TEOS	TEOS + O_2	1.0	350	288

Table 5.2: Process parameters for the deposition of films used for the encapsulation of MgO.

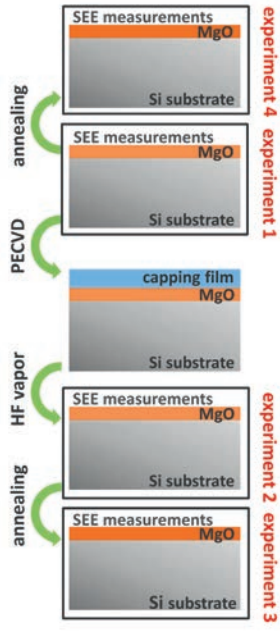

Figure 5.9: Outline of the treatment and SEE characterization steps conducted to investigate influence of various chemical and thermal treatments on MgO properties.

5.5.2. RESULTS AND DISCUSSION

ELEMENTAL COMPOSITION

MgO films subjected to XPS analysis were stored under ambient conditions for about 8 weeks after the deposition and/or conducted treatments. First, we will evaluate the effect of HF vapour on the surface composition, after which the XPS data collected from the annealed MgO films will follow. Mg 2p spectra of a 5 nm-thick MgO film which was encapsulated by silane-based oxide and subsequently released in HF vapour is presented in Figure 5.10a. The signal can be resolved into a major component from MgO at 50.0 eV and a peak at 51.4 eV, which indicates the formation of a fluorine compound during the overetch time in HF vapour. Similar XPS profile is given in a report on MgO microspheres [26], where the binding of fluorine and magnesium atoms is confirmed by a Mg 2p component at 51.7 eV. Prominent F 1s signal in our study is present not only on the film surface, but also in the bulk, as shown in Figure 5.10b.

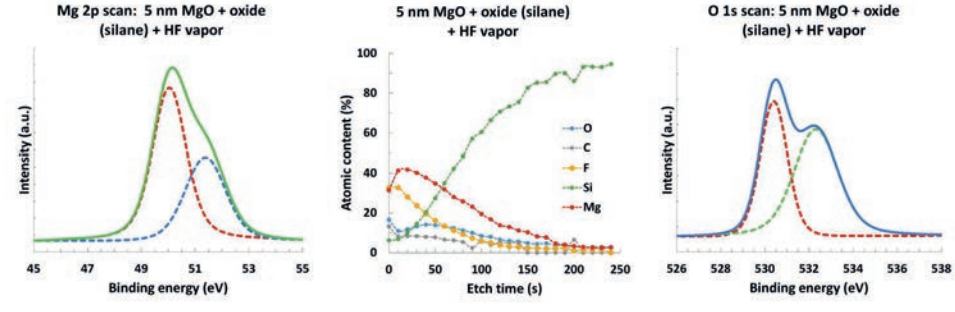

(a) (b) (c)

Figure 5.10: XPS analysis of a 5 nm-thick MgO film after encapsulation by silane-based oxide and its removal by HF vapour: (a) fitted Mg 2p spectra on the surface; (b) in-depth atomic content calculated after the etching of film by ion-sputtering and (c) O1s spectra on the surface.

The XPS analysis of as-deposited and thermally treated MgO films at 700 and 900 °C showed that the O 1s peak consists of two components (Figure 5.10c and Figure 5.11a – 5.11c). A major one occurs in the range from 531.1 to 532.3 eV and is attributed to atoms of oxygen bonded to magnesium. The peak at higher binding energies (533.1 – 533.7 eV) originates from adsorbed hydroxyl groups, indicating that these samples were "aged" at the moment of XPS investigation. Different studies showed that a satellite peak in O 1s signal arises already 1 – 2 hours after the film deposition [21] [18].

It can be noted that the contribution of the Mg(OH) peak is less pronounced in the film after the thermal treatment at 900 °C (Figure 5.11c), whereas the annealing of MgO layer at 1100 °C eliminated the Mg(OH) signal and produced a non-hygroscopic surface (Figure 5.11d). Survey of Si 2p spectra in the bulk of the latter film (Figure 5.12d) revealed an additional signal at 103.3 eV, which demonstrates the oxidation of the Si substrate, as also reported for MgO films subjected to a rapid thermal annealing [27]. Growth of the interfacial layer caused by annealing at 1100 °C can also be confirmed by the change of the film colour. Initially, the colour of MgO could not be distinguished from the polished Si substrate, whereas the annealing produced a blue-shaded surface.

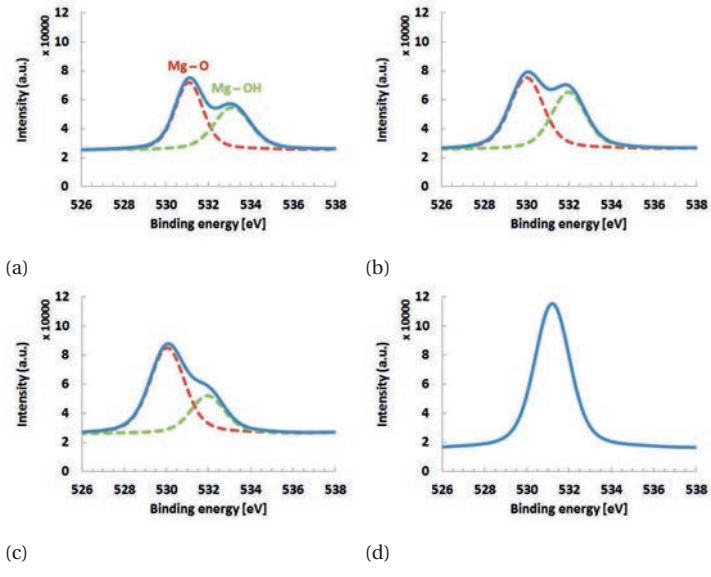

Figure 5.11: Fitted O 1s peak recorded on the surface of 25 nm-thick MgO films on top of Si: (a) as-deposited; annealed at (b) 700; (c) 900 and (d) 1100 °C.

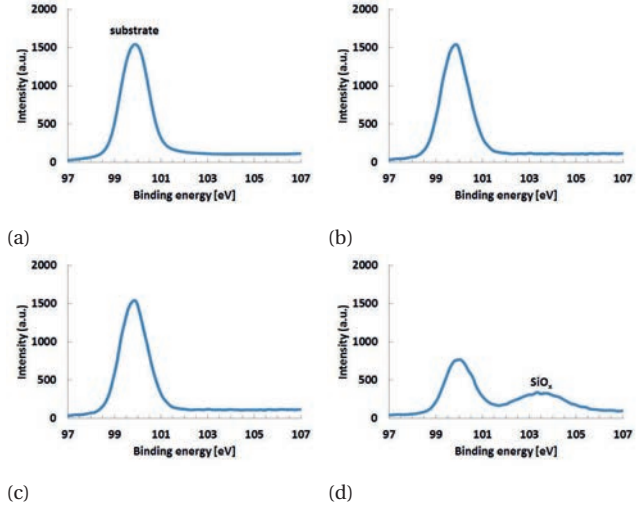

Figure 5.12: Fitted in-depth Si 2p signal recorded for 25 nm-thick MgO films on Si substrate: (a) as-deposited; annealed at (b) 700; (c) 900 and (d) 1100 °C. All peaks are recorded at the same etch level (285 s after the ion-sputtering started).

From the depth profiles of relevant peaks, the atomic content in the same set of MgO films is calculated and plotted in Figure 5.14. A rise of oxygen concentration in Figure 5.13b and 5.13c suggests oxidation of the Si substrate at annealing temperatures of 700 and 900 °C. Apart from the high carbon contamination level on the surface (15 – 20 at%),

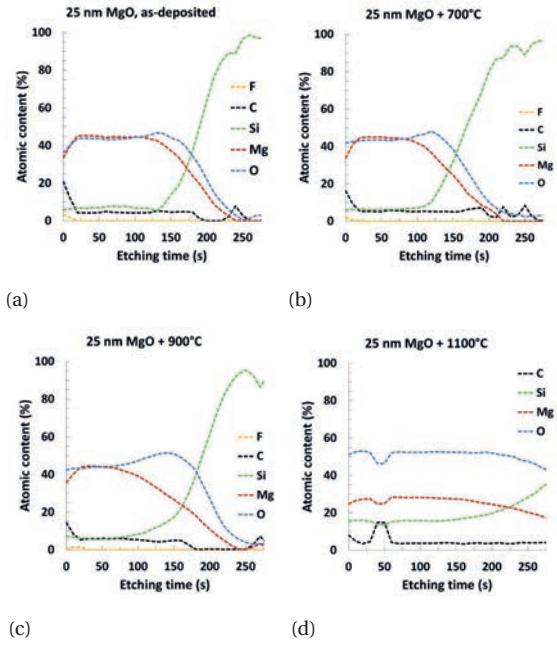

Figure 5.13: In-depth atomic content of 25 nm- thick MgO films (a) as-deposited and annealed at (b) 700, (c) 900 and (d) 1100 °C.

an amount of 5 at% of carbon is present in the bulk, most likely due to incomplete reaction with H_2O which leaves some of the ligands on the surface. In this case, longer H_2O exposure times or a higher deposition temperature would reduce the carbon content. Alternatively, the carbon may result from a thermal decomposition of the $Mg(Cp)_2$ precursor employed for the ALD of MgO, which can be prevented by a lower deposition temperature or shorter $Mg(Cp)_2$ exposure times. Due to the abovementioned oxidation of the Si substrate and increase in thickness of the film annealed at 1100 °C, a stronger Si signal is present near the surface, and its rise is delayed in comparison with other samples. Additional XPS analysis, performed on films treated with HF vapour prior to thermal annealing (experiment 2), showed that fluorine content was eliminated by exposure to high temperatures.

SURFACE MORPHOLOGY

The AFM measurements of as-deposited 25 nm-thick MgO films reveal a smooth and uniform surface. Root mean square (RMS) roughness extracted from the area shown on Figure 5.14a is only 0.37 nm. Due to a long exposure to atmospheric conditions (1 – 2 months), this sample already had $Mg(OH)_2$ and $MgCO_3$ formed on the surface, but that does not seem to affect its smoothness. Deposition of a capping layer followed by its removal in HF vapour did not change the surface roughness either, as shown in Figure 5.6. The surface roughness of MgO films annealed at 700 °C is similar to the one for as-deposited films, with a value of 0.56 nm (Figure 5.14b), whereas the annealing tem-

perature of 900 °C increased the RMS roughness to 1.30 nm. The sample treated at 1100 °C exhibits a drastically changed surface morphology, with RMS roughness of 9.15 nm and a grain size of 45 nm. The effect of annealing at 700 °C on the surface morphology of HF-treated MgO film is presented in Figure 5.14e. The extracted RMS roughness value of 0.49 nm is similar to the as-deposited film subjected to annealing under the same conditions, but with more than two times smaller grains. Data on RMS roughness and grain size is summarized in Table 5.3. For a better insight into the surface features, height profiles of films captured by AFM are presented in Figure 5.14b, 5.14d, 5.14f, 5.14h, and 5.14j. Plotted data is recorded over the center of $1 \times 1\ \mu m^2$ scanned areas in the x-direction from Figure 5.14a, 5.14c, 5.14e, 5.14g and 5.14i, respectively.

MgO film	RMS roughness (nm)	Grain size (nm)
As-deposited	0.37	6.5
Annealing at 700 °C	0.56	13.8
Annealing at 900 °C	1.30	28
Annealing at 1100 °C	9.15	45
10 min HF vapour + annealing at 700 °C	0.49	6.2

Table 5.3: Morphology data obtained from AFM analysis of different MgO films with a thickness of 25 nm.

CRYSTALLINITY

XRD data analysis was conducted on 50 nm-thick MgO grown on silicon. At first, measurements were performed on as-deposited film. Peak detected at 36.7° matches well the (111) peak from the Powder Diffraction File (PDF) 02-1207 for periclase (cubic MgO phase), positioned at 2θ of 36.95 (black plot in Figure 5.15a). Peaks (200) and (220), typically corresponding to 2θ of 42.87 and 62.2°, were not observed. This finding is in line with another report on MgO obtained by using the same combination of precursors, at deposition temperature in the range from 200 to 300 °C [11]. In contrast to that, studies [12] and [13] report on presence of all three abovementioned orientations in ALD MgO films (deposition parameters listed in Table 5.1). To investigate the effect of annealing on crystallinity of MgO, we performed XRD analysis with in-situ heating. To match the conditions from experiment 4 conducted in our work, the heating was performed in N_2 ambient, with a rate of 10 °C. However, due to limitations of the used XRD system, the maximum temperature could not exceed 960 °C. As shown in Figures 5.15a (red plot) and 5.15b, peak (111) becomes more pronounced throughout the thermal treatment, and shifts towards slightly higher 2θ value (36.95°), closer to the value tabulated in the PDF database.

SECONDARY ELECTRON EMISSION

Experiment 1: As-deposited and "aged" MgO films. RSEE measurements on as-deposited 5, 15 and 25 nm-thick MgO films have already been reported in Section 5.4.3. In addition to this, a 25 nm-thick MgO layer is re-measured approximately two months after the first SEE examination, after being stored under ambient conditions. As shown in Figure 5.7 , the maximum SEY of the "aged" film dropped to around 3.3, possibly due to the chemisorption of water and CO_2 from the air.

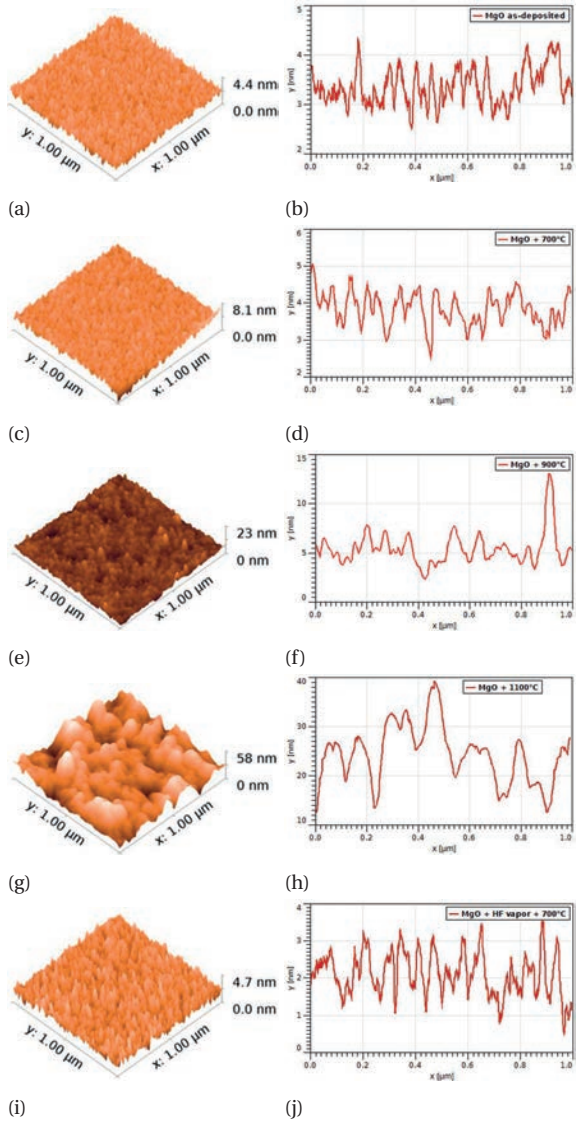

Figure 5.14: AFM images of 25 nm-thick MgO films and corresponding height profiles over the center (y = 0.5 µm) of the scanned area, in the x-direction: as-deposited (a, b) and annealed at 700 °C (c, d); 900 °C (e, f); 1100 °C (g, h); HF vapour-treated and annealed at 700 °C (i, j). Surface investigation was performed 1 – 2 months after the deposition and/or thermal treatment. Samples were kept in the CR 100 environment prior to AFM analysis.

Experiment 2: Chemical treatments. The two types of oxides coated on top of as-deposited MgO films are removed after 2 month-long storage by using HF vapour (experiment 2 in Figure 5.9). SEE performances of 25 nm-thick MgO films after these treatments are shown in Figure 5.17. In addition, we present a result from a film exposed

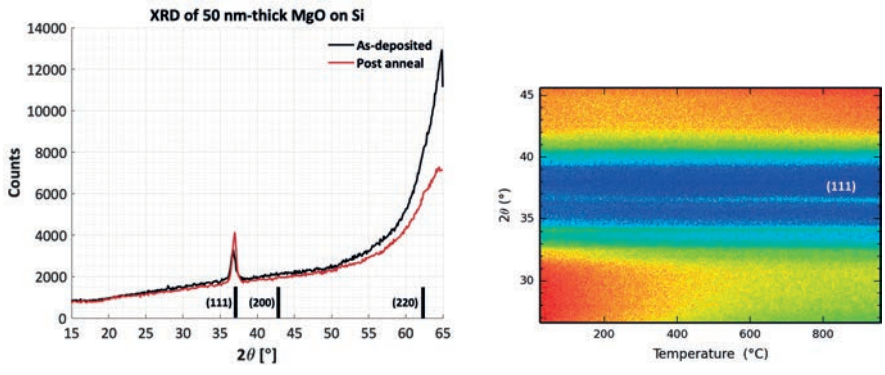

(a) (b)

Figure 5.15: XRD data obtained from the 50 nm-thick MgO deposited on Si substrate. XRD spectra is recorded for as-deposited film at room temperature (black plot) and at 960 °C in N_2 environment (a). 2θ vs. temperature plot reveals that annealing slightly intensifies the MgO (111) peak (b).

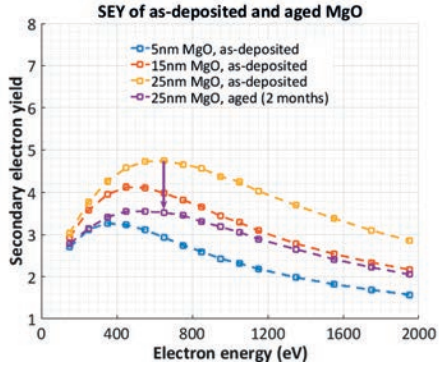

Figure 5.16: RSEY curves of as-deposited MgO films with different thicknesses, and a re-measurement of a 25 nm-thick layer 2 months after the first investigation. Energy of primary electrons is varied from 0.3 to 2 keV.

only to HF vapour for 10 min, without the preceding capping step. All performed surface modifications increased the SEY compared to the as-deposited layer, in the range from 5.6 to 6.6. The surface morphology of HF-treated MgO has not significantly changed in comparison to as-deposited film [28]. Since the only verified difference in chemical composition is the presence of a fluorine peak (Figure 5.10a and 5.10b), the improvement of SEY is attributed to this factor. Etching time of the as-deposited MgO in HF vapour seems not to affect the SEE, and the same result is obtained after 5 and 10 min long cycle (only one curve is plotted in Figure 5.17). Results obtained from films with a thickness of 5 and 15 nm display the same trend: deposition and removal of the capping layer provide higher SEY than HF vapour etching solely. Furthermore, the TEOS-based oxide proved to be a better choice for the capping of MgO. The reason behind this is not clear to this date, but one of the influencing factors may be the soak time of the wafer at the temperature of 350 °C, prior to the PECVD of TEOS-based oxide. This 2 min-long

step, involving gas-purging, is introduced in the chamber of the system to reduce defects in the growing film. In our case it probably removes the contamination from the MgO film, producing a "cleaner" surface after the removal of PECVD material. Finally, these results show that the encapsulation provides SEY two times greater than a film stored in air for the same amount of time (re-measured MgO film in Figure 5.7).

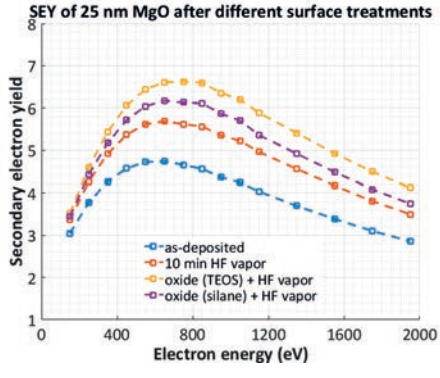

Figure 5.17: RSEY curves of as-deposited MgO films with different thicknesses, and a re-measurement of a 25 nm-thick layer 2 months after the first investigation. Energy of primary electrons is varied from 0.3 to 2 keV.

Experiments 3 and 4: Thermal annealing. The SEE behaviour of MgO films with different thicknesses after annealing at 700 °C is presented in Figure 5.18. For a better visual guidance, results from the as-deposited films are included in the same graph. Improvement of the SEY is confirmed for all films, with the highest yield of 6.4 recorded for the 25 nm-thick MgO layers. Next, the set of samples presented in Figure 5.17 has too undergone the thermal treatment at 700 °C. The outcome, as illustrated in Figure 5.19, is almost identical curves of all three films that have been exposed to HF vapour. These samples exhibit somewhat lower SEY of around 5.8, as compared to 6.4 obtained after annealing of the as-deposited sample. XPS data of these films (not included here) show the absence of the fluorine signal. Most likely, these films sustained a different modification in morphology due to the initial presence of the fluorine compound on the surface, as shown in Figure 5.14b and 5.14e. Emission of secondary electrons is less efficient from the equally rough surface with smaller grains, with the SEY of 5.8 and 6.4 for the grain size of 6.2 and 13.8 nm, respectively. Opposite trend is reported by Vaz [29], where diamond surfaces with a (several orders of magnitude) reduced grain size exhibited higher SEY. Therefore, a further analysis on chemical composition of HF-vapour treated and annealed MgO films is required to interpret this result.

Impact of annealing at higher temperatures (900 and 1100 °C) on the SEE performance of for 25 nm-thick MgO films is shown in Figure 5.19. The maximum yield of 7.25 is measured from the film annealed at 900 °C, which is the highest SEY value in this study. However, a deviation in the tail of this curve is an evidence of a charge-up occurring in the film during the measurement. This is probably the side effect of initialized growth of interfacial silicon-suboxides (as suggested by the increase of O 1s signal in Figure 5.13c) which increased the thickness of investigated film and hindered the electron supply from Si substrate to the electron-emitting surface. The effect of thickness of MgO

film on its SEE properties is discussed in the study by Lee et al [30]. Charge-up is even more severe for the sample annealed at 1100 °C, for which the abrupt increase of thickness is demonstrated both by presence of SiO_x peak (Figure 5.12d) and a higher oxygen content at the surface (Figure 5.13d). Therefore, the SEYs of films annealed at 900 and 1100 °C could not be accurately established and are expected to differ from the values plotted in Figure 5.20.

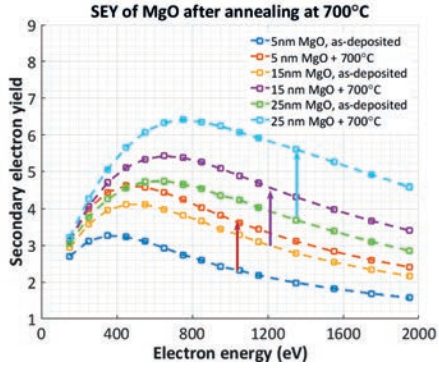

Figure 5.18: Effect of annealing at 700 °C on RSEE properties of MgO films with different thicknesses.

Comparison of SEY of as-deposited MgO to films annealed at 700 and 900 °C only in terms of morphology parameters suggests the increase of SEY to be related to the grain size. This result is not in line with a reports by Dzhanoev [31] and Burton [32], where the presence of larger grains on the flat surface and increased roughness induced degradation of SEE. However, to attribute SEY increase to grain size increase alone would be a misleading conclusion, because of the varying composition of materials investigated in this work.

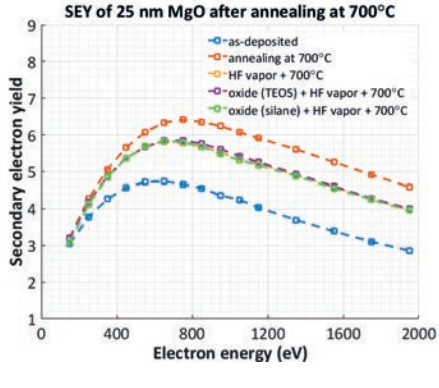

Figure 5.19: RSEY of 25 nm-thick MgO films submitted to different chemical treatments and subsequent annealing at 700 °C.

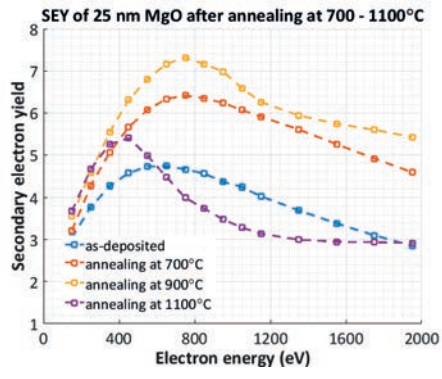

Figure 5.20: RSEY of 25 nm-thick MgO films after annealing in the temperature range from 700 to 1100 °C.

5.6. CONCLUSIONS

Large-area arrays of ultra-thin (5 – 25 nm) free-standing MgO membranes are successfully fabricated and characterized. The optimal film thickness for the secondary emissive ALD MgO membranes was found to be 5 nm, with the TEY of around 3, which was elevated to 5.5 under certain measurement conditions. ALD provides a superior and simple way to ensure thickness and conformality control, which is necessary for a reliable production process of smooth ultra-thin membranes. We demonstrated that for TiPC application MgO is better suited than LPCVD SiN and ALD Al_2O_3, due to its better results in terms of TSEY. Performance of MgO membranes can be further improved by lowering electron affinity through a convenient surface termination. MgO films grown on silicon by ALD, with thicknesses in the range from 5 to 25 nm, have been subjected to different chemical and temperature treatments to improve the SEE performance, for their application in the Timed Photon Counter. A study on crystallinity, morphology and chemical composition of various MgO films is carried out in order to relate the measured SEE to material properties. First, MgO films underwent treatments which mimic the final steps in the fabrication of ultra-thin membranes (tynodes) for electron multiplication. As a protection against processing steps in the release of the tynodes, we applied two types of PECVD materials as encapsulation layers, silane and TEOS based-oxide, which are then removed by HF vapour etching. After the release, MgO, now with a modified surface, is analysed in terms of SEE, by using a sample-biasing method inside the SEM. Increased SEY of the treated MgO, compared to as-deposited films, is demonstrated. TEOS-based oxide turned out to be a more beneficial capping film, providing the elevation of the maximum SEY from 4.8 to 6.6 for 25 nm-thick films. This improvement is ascribed to the presence of magnesium fluoride on the surface. Moreover, the capping of films proved to prevent the aging of MgO, which negatively affects the SEE. In addition, we performed annealing of MgO at high temperatures and validated that this also improved the SEE performance. In this set of samples, the highest SEY of 7.2 was recorded after annealing of 25 nm-thick MgO at 900 °C. Annealing at 1100 °C is expected to provide an even better result, but the charge-up obstructed the quantification of SEY for those films. Nevertheless, temperature treatments are suggested for the boost of SEY of free-standing tynodes

if a more efficient electron supply is provided. AFM scanning revealed a drastic change of surface morphology after the annealing steps, whereas XPS data suggests the formation of complex magnesium silicates and silicides already in the close-to-surface area. As future work, an examination of the electron affinity (or other properties related to the energy band of material) is suggested for a better understanding on how surface and composition modifications affect the SEE of thin MgO films.

REFERENCES

[1] Z. Diao, A. Panchula, Y. Ding, M. Pakala, S. Wang, Z. Li, D. Apalkov, H. Nagai, and et. al. Spin transfer switching in dual MgO magnetic tunnel junctions. *Applied Physics Letters*, 90(13):132508, March 2007.

[2] M.I. Faley, S.B. Mi, A. Petraru, C.L. Jia, U. Poppe, and K. Urban. Multilayer buffer for high-temperature superconductor devices on MgO. *Applied Physics Letters*, 89(8):082507, August 2006.

[3] L. Beckers, J. Schubert, W. Zander, J. Ziesmann, A. Eckau, P. Leinenbach, and C. Buchal. Structural and optical characterization of epitaxial waveguiding BaTiO3 thin films on MgO. *Journal of Applied Physics*, 83(6):3305–3310, March 1998.

[4] M. Li, M. Xu, J. Zou, H. Tao, L. Wang, Z. Zhou, and J. Peng. Realization of Al_2O_3/MgO laminated structure at low temperature for thin film encapsulation in organic light-emitting diodes. *Nanotechnology*, 27(49):494003, November 2016.

[5] J.P. Boeuf. Plasma display panels: physics, recent developments and key issues. *Journal of Physics D: Applied Physics*, 36(6):R53–R79, February 2003.

[6] S. Tao, H.W. Chan, and H. van der Graaf. Secondary electron emission materials for transmission dynodes in novel photomultipliers: A review. *Materials*, 9(12):1017, December 2016.

[7] T. Harada, F. Simeon, E.Z. Hamad, and T.A. Hatton. Alkali metal nitrate-promoted high-capacity MgO adsorbents for regenerable CO2 capture at moderate temperatures. *Chemistry of Materials*, 27(6):1943–1949, March 2015.

[8] T. Miyata. New materials consisting of multicomponent oxides for thin-film gas sensors. *Journal of The Electrochemical Society*, 144(7):2432, 1997.

[9] A.M.E. Raj, M. Jayachandran, and C. Sanjeeviraja. Fabrication techniques and material properties of dielectric MgO thin films—a status review. *CIRP Journal of Manufacturing Science and Technology*, 2(2):92–113, January 2010.

[10] R. Huang and A.H. Kitai. Temperature-dependence of the growth orientation of atomic layer growth MgO. *Applied Physics Letters*, 61(12):1450–1452, September 1992.

[11] M. Putkonen, T. Sajavaara, and L. Niinistö. Enhanced growth rate in atomic layer epitaxy deposition of magnesium oxide thin films. *Journal of Materials Chemistry*, 10(8):1857–1861, 2000.

[12] H. Wang and K. Fu. Nucleation and growth of MgO atomic layer deposition: A real-time spectroscopic ellipsometry study. *Journal of Vacuum Science & Technology A: Vacuum, Surfaces, and Films*, 31(6):06F101, 2013.

[13] S. Vangelista, R. Mantovan, A. Lamperti, G. Tallarida, B. Kutrzeba-Kotowska, S. Spiga, and M. Fanciulli. Low-temperature atomic layer deposition of MgO thin films on Si. *Journal of Physics D: Applied Physics*, 46(48):485304, November 2013.

[14] B.B. Burton, D.N. Goldstein, and S.M. George. Atomic layer deposition of MgO using bis(ethylcyclopentadienyl)magnesium and H_2O. *The Journal of Physical Chemistry C*, 113(5):1939–1946, January 2009.

[15] M. Putkonen, L-S. Johansson, E. Rauhala, and L. Niinistö. Surface-controlled growth of magnesium oxide thin films by atomic layer epitaxy. *Journal of Materials Chemistry*, 9(10):2449–2452, 1999.

[16] T. Hatanpää, J. Ihanus, J. Kansikas, I. Mutikainen, M. Ritala, and M. Leskelä. Properties of $Mg_2(thd)_4$ as a precursor for atomic layer deposition of MgO thin films and crystal structures of $Mg_2(thd)_4$ and $Mg(thd)_2(EtOH)_2$. *Chemistry of Materials*, 11(7):1846–1852, July 1999.

[17] J.D. Baek, Y-J. Yoon, W. Lee, and P-C. Su. A circular membrane for nano thin film micro solid oxide fuel cells with enhanced mechanical stability. *Energy & Environmental Science*, 8(11):3374–3380, 2015.

[18] L. Savio, E. Celasco, L. Vattuone, and M. Rocca. Enhanced reactivity at metal-oxide interface: water interaction with MgO ultrathin films. *The Journal of Physical Chemistry B*, 108(23):7771–7778, June 2004.

[19] J. Carrasco, F. Illas, and N. Lopez. Dynamic ion pairs in the adsorption of isolated water molecules on alkaline-earth oxide (001) surfaces. *Physical Review Letters*, 100(1), January 2008.

[20] L. Giordano, J. Goniakowski, and J. Suzanne. Partial dissociation of water molecules in the (3×2) water monolayer deposited on the MgO (100) surface. *Physical Review Letters*, 81(6):1271–1273, August 1998.

[21] S. Altieri, L.H. Tjeng, and G.A. Sawatzky. Electronic structure and chemical reactivity of oxide-metal interfaces: MgO(100)/Ag(100). *Physical Review B*, 61(24):16948–16955, June 2000.

[22] G. Cabailh, R. Lazzari, H. Cruguel, J. Jupille, L. Savio, M. Smerieri, A. Orzelli, L. Vattuone, and M. Rocca. Stoichiometry-dependent chemical activity of supported MgO(100) films. *The Journal of Physical Chemistry A*, 115(25):7161–7168, June 2011.

[23] H.A. Prescott, Z-J. Li, E. Kemnitz, J. Deutsch, and H. Lieske. New magnesium oxide fluorides with hydroxy groups as catalysts for Michael additions. *Journal of Materials Chemistry*, 15(43):4616, 2005.

[24] N.R. Rajopadhye and S.V. Bhoraskar. Secondary electron emission of sputtered alumina films. *Pramana*, 25(3):327–334, September 1985.

[25] S.J. Jokela, I.V. Veryovkin, A.V. Zinovev, J.W. Elam, A.U. Mane, Q. Peng, and Z. Insepov. Secondary electron yield of emissive materials for large-area micro-channel plate detectors: Surface composition and film thickness dependencies. *Physics Procedia*, 37:740–747, 2012.

[26] L-X. Li, D. Xu, X-Q. Li, W-C. Liu, and Y. Jia. Excellent fluoride removal properties of porous hollow MgO microspheres. *New Journal of Chemistry*, 38(11):5445–5452, 2014.

[27] H.-L. Lu, S-J. Ding, and D.W. Zhang. Investigation of thermal stability of atomic-layer-deposited MgO thin films on Si (100) using X-ray photoelectron spectroscopy. *Electrochemical and Solid-State Letters*, 13(3):G25–G28, 2010.

[28] V. Prodanovic, H.W. Chan, A.U. Mane, J.W. Elam, H. van der Graaf, and P.M. Sarro. Ultra-thin ALD MgO membranes as MEMS transmission dynodes in a timed photon counter. In *2017 IEEE 30th International Conference on Micro Electro Mechanical Systems (MEMS)*, pages 740–743. IEEE, 2017.

[29] R. Vaz, P.W. May, N.A. Fox, C.J. Harwood, V. Chatterjee, J.A. Smith, C.J. Horsfield, J.S. Lapington, and S. Osbourne. Measurement of the secondary electron emission from CVD diamond films using phosphor screen detectors. *Journal of Instrumentation*, 10(03):P03004, 2015.

[30] J. Lee, T. Jeong, S. Yu, S. Jin, J. Heo, W. Yi, D. Jeon, and J.M. Kim. Thickness effect on secondary electron emission of MgO layers. *Applied surface science*, 174(1):62–69, 2001.

[31] A.R. Dzhanoev, F. Spahn, V. Yaroshenko, H. Lühr, and J. Schmidt. Secondary electron emission from surfaces with small structure. *Physical Review B*, 92(12):125430, 2015.

[32] T.S. Burton, T.C. Back, S.B. Fairchild, and G.B. Thompson. Influence of surface roughness on secondary electron emission from graphite. *Journal of Vacuum Science & Technology A: Vacuum, Surfaces, and Films*, 35(4):041404, 2017.

6

TOWARDS IMPROVED DESIGN OF THE TYNODES

In this chapter we give the SEE analysis of a few other materials investigated in a search for the best tynode material. After that, a design and fabrication procedure of a tynode with a novel geometry is presented. The new design enables better focusing of the tynodes, eliminates charging up and allows vertical stacking of the layers for the final application in the TiPC.

6.1. OTHER CANDIDATES FOR THE TYNODE MATERIALS

BESIDES LPCVD SiN, ALD Al_2O_3 and ALD MgO (Chapters 3 – 5), four additional materials have been investigated for the electron multiplication in the TiPC: LPCVD silicon carbide (SiC), ALD aluminium nitride (AlN), ultrananocrystalline diamond (UNCD) grown by microwave plasma-enhanced chemical vapour deposition (MPCVD) and monocrystalline silicon. In this section we present the analysis on RSEY of all four materials, and preliminary TEY results for UNCD and Si.

6.1.1. LPCVD SiC

Electron-induced secondary electron emission of silicon carbide films are not reported in literature, but we decided to investigate it because of the possibility to tune its resistivity in the LPCVD process. A 200 nm-thick SiC film was deposited by LPCVD on top of a Si substrate in a hot-wall LPCVD reactor (Tempress Systems). Dichlorosilane (SiH_2Cl_2, DCS) and 5% acetylene (C_2H_2) diluted in hydrogen (H_2) were employed as precursor gasses. The amounts of DCS and C_2H_2 were set to 65 and 435 sccm, respectively. Deposition temperature and pressure were kept at 760 °C and 0.6 mbar, resulting in a deposition rate of around 11.8 nm/min. Extensive characterization of this film can be found in a study by Morana et. al. [1]. As shown in Figure 6.1, SiC displays a poor electron multiplication, providing a maximum SEY of only 2.1. Therefore, we discarded this material for the TiPC application and did not proceed with the fabrication of SiC tynodes.

6.1.2. ALD AlN

Aluminium nitride is a wide-bandgap material which is reported to exhibit RSEY higher than 6 with after cesiation of its surface [2]. Aluminium nitride films were grown by plasma enhanced ALD (PEALD), by applying 0.1 s and 8 s-long pulses of TMA and NH_3 plasma . Transport gasses for TMA and ammonia were nitrogen and argon, respectively. In between these pulses, a 4 s-long purging with N_2 was performed, in order to remove the excess reactants and volatile products from the chamber. The deposition temperature was 350°C, whereas the reactor pressure was maintained at 1 mbar and the plasma power at 2 kW. AlN films were deposited directly on the Si substrate, with a growth rate of approximately 0.1 nm/cycle. The thickness uniformity over the wafer, as evaluated by spectroscopic ellipsometry, was ± 2.3 nm. The average surface roughness (RMS), measured on a 100 nm-thick film by atomic force microscopy (AFM), was 2.4 nm. More details on the preparation and characterization of ALD AlN can be found in a study by a group which provided the AlN films for our experiments [3]. The RSEE analysis of this film confirmed the yield of 2.8 (Figure 6.1), which is similar to the value reported in [2], where AlN films prepared by molecular beam epitaxy (MBE) are investigated. However, that study shows that the rather low RSEY produced by a non-treated surface can be multiplied almost three times by cesium adsorption which introduces negative electron affinity (NEA) at the surface. Therefore, AlN films with a suitable termination might still be an adequate substitute for previously analysed tynode materials. Fabrication of AlN membranes has already been reported for their application in nanomechanical resonators [4] and for mass sensing [5]. Moreover, a production of large ALD AlN membranes with thicknesses down to 40 nm demonstrated in [6] indicates the mechanical aptness of this material for the TiPC. However, since this film provided only a slightly

higher yield than previously investigated LPCVD SiN, and we are currently not able to perform Cs adsorption on AlN surface, it was not used in the fabrication of the tynodes.

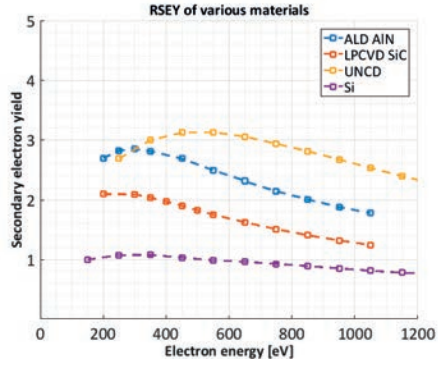

Figure 6.1: RSEY of the four additional materials investigated for the electron emission in the TiPC. Measurement method is described in Section 3.3.7.

6.1.3. ULTRANANOCRYSTALLINE DIAMOND (UNCD)

Ultrananocrystalline diamond film is a type of nanostructured carbon developed in 1990s in Argonne National Laboratory (ANL). This material consists of pure sp^3 carbon-bonded grains with sizes of only 3 – 5 nm, whereas the grain boundaries present a mixture of high-energy sp^2 and sp^3 diamond phases. Due to its nanoscale morphology and electronic structure, UNCD displays excellent mechanical, tribological, electrical, chemical, thermal and electron emission properties which make it an attractive candidate for various applications. UNCD is enabling a wide range of macro- and nanoscale devices, such as: RF MEMS/NEMS resonators and switches, biosensors, field-emission cathodes and wear-resistant coatings for mechanical pumps. A detailed status review of numerous UNCD applications is given in a publication by a research group at ANL which developed and patented the synthesis of this material [7]. The growth process of UNCD uses microwave plasma-enhanced chemical vapour deposition (MPCVD) with argon-rich chemistry to which methane (CH_4) is added, usually in a percentage ratio of Ar/CH_4 = 99/1. Opposed to the methods for deposition of diamond films with larger crystallites (microcrystalline and nanocrystalline diamonds), hydrogen is not added to this mixture. At elevated substrate temperatures CH4 decomposes into various hydrocarbon species and carbon dimers (C_2). The latter component has a critical role in the nucleation of UNCD. Namely, C_2 has a low activation energy for the insertion into the substrate, which makes UNCD the only form of diamond which can be grown at temperatures as low as 400 °C [8]. The described deposition method results in smooth, dense and phase-pure films over large surfaces (diamond-on-Si and diamond-on-insulator wafers with diameter of 200 mm are already commercially available). In the light of the application for TiPC, UNCD is a good choice for the tynode material because, like all diamond materials, it exhibits high SEY [9]. Moreover, addition of nitrogen (N_2) into the Ar/CH_4 mixture provides a semi-metallic conductivity for UNCD films [10]. As a consequence, no charging up would occur during the secondary electron emission. So far the growth of good-

quality UNCD films has been demonstrated for thicknesses down to 100 nm [11]. Thus, in the fabrication of the tynodes this thickness must be further decreased, or a way to controllably thinning down UNCD films established. The material utilized in this work is nitrogen-doped UNCD (N-UNCD). Films with thicknesses of 130 nm are deposited in a microwave cavity plasma reactor (MCPR) supplied by Lambda Technologies, at a fixed frequency of 915 MHz and a power of 10 kW, with a deposition rate of 0.3 µm/h. For this initial deposition run the substrate temperature was 850 °C, with an objective to decrease it in the future tests, and employed plasma consisted of Ar (79%)/CH4 (1%)/N2 (20%). Supplier of UNCD (ANL) guaranteed the following film characteristics: resistivity of 0.0448 Ωcm, relatively smooth surface with RMS roughness values of 15 – 25 nm and a tensile stress in the range from 50 to 100 MPa [12] [13] [14]. UNCD membranes have a great potential in a variety of applications, such as photonics, bio-sensing, capacitive micromachined ultrasonic transducers (CMUTs) and membrane-sealed vacuum cavities. However, in the majority of reports, employed UNCD films have a much larger thickness, in the range of micrometers. Somewhat thinner membranes were utilized for the investigation of their fracture strength (600 – 800 nm-thick) [15], whereas Kim et al. [16] demonstrated the production of 100 nm-thick boron-doped UNCD membranes with a goal to employ them for mass spectrometry detection of large proteins. For the TSEE investigation of UNCD, we fabricated test membranes with the size of 350 × 500 µm^2. A 130 nm–thick layer of UNCD was deposited on top of a Si substrate covered with 300 nm-thick thermal oxide (Figure 6.2a). PECVD oxide is used as a mask material for the backside DRIE of the Si substrate, after which the oxide is removed in HF vapour (Figure 6.2b). An optical microscope image of a 130 nm-thick UNCD membrane after the release is shown in Figure 6.2c.

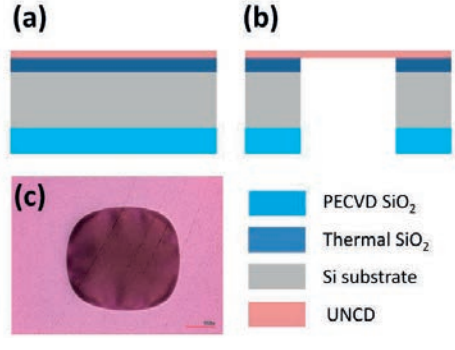

Figure 6.2: Main steps of the fabrication process of test UNCD membranes for the TSEE analysis. UNCD was deposited on top of thermal oxide (a), followed by removal of Si bulk by DRIE. Final release of the UNCD membrane is performed in HF vapour (b). Optical micrograph of a 130 nm-thick released UNCD membrane, with a surface of 350 × 375 µm^2 (c).

These UNCD membranes displayed a TEY of 1.8 (at the energy of 5 keV), whereas REY had a value of 3.2 (Figure 6.3a). We initially ascribed these low coefficients to non-treated emission surface. As an attempt to improve the electron multiplication, a bake out step was performed. The samples were kept for 2 hours in N_2 environment at the temperature of 150 °C, but after this procedure the SEE curve was unaltered (Figure 6.3b). Emission

properties of UNCD were measured in two different configurations in which the distance between the membrane and the holder in the DFC setup is varied. TEY is almost 65% higher when the membrane is facing the holder (as shown in Figure 3.12). In future work, more effort should be put in functionalization and/or cleaning of the UNCD surface and in developing a method to produce thinner membranes (with thicknesses below 20 nm) with TEY peak corresponding to primary energy lower than 1 keV.

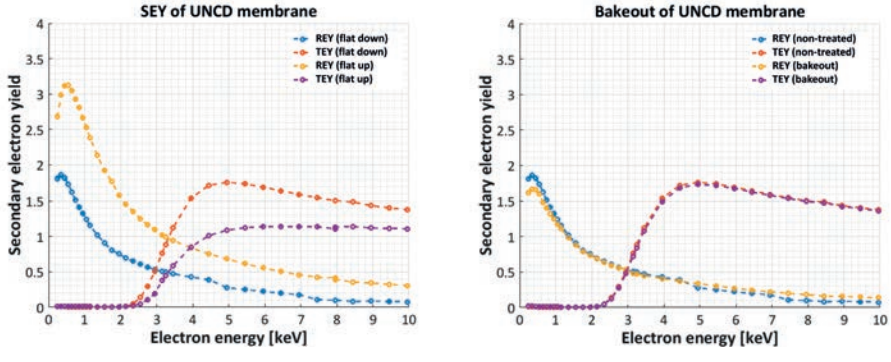

(a) (b)

Figure 6.3: Total transmission and reflection secondary electron coefficients colected from 130 nm-thick UNCD membrane in two different configurations: with the membrane touching the holder in DFC (''flat down") and with Si substrate touching the holder (''flat up") (a). Bake-out of the membrane did not change its SEE properties (measurement conducted in the ''flat down" configuration) (b).

6

6.1.4. SINGLE CRYSTALLINE SILICON

Studies from the '70s report extremely high RSEY provided by cesium- and oxygen treated silicon films with thicknesses in the range of 3 to 10 µm. These surfaces, activated to a state of negative electron affinity, exhibit a RSEY of up to 1800 [17] [18]. The maximum SEE for non-treated Si surface, as reported in [19]and [20], is between 1.2 and 1.5. We measured RSEY on a 525 µm-thick Si wafer with (100) crystalline orientation, p-type doping (5 – 10 Ω cm). Results are compared for samples with a native oxide on top (usually with a thickness of 1.5 – 2 nm) and samples subjected to 5 min-long etching in HF and subsequent Marangoni drying in isopropanol (IPA), which reportedly blocks formation of native oxide for two days after the cleaning procedure . As shown in Figure 6.4a, removal of native oxide almost doubled the RSEY achieved with a non-treated Si surface. Suspended Si membranes with submicron thicknesses have been utilized for various applications, such as UV and X-ray spectrometry and as an efficient extreme ultraviolet (EUV) diffraction grating [21]. Membranes with thicknesses down to only 8 nm have been fabricated and used as model systems to test phonon confinement [22], similar to the work by Chávez-Ángel et al. which discusses the thermal conductivity of these 2D suspended structures [23]. Si membranes used for the TSEE analysis in this work were fabricated from silicon on insulator (SOI) wafers with 400 nm-thick buried oxide and 340 nm-thick top Si layer (Figure 6.4a). The Si layer was thinned down to 40 nm by thermal oxidation (around 680 nm of oxide are grown consuming 300 nm of silicon),

after which DRIE was used to etch the Si substrate (Figure 6.4b). Finally, the release of the Si membranes was done by etching the SiO_2 films on both sides in HF vapour (Figure 6.4c). An optical micrograph of a released membrane (Figure 6.4d) reveals a buckled surface, typical for Si membranes fabricated using a similar process [22] [23] [24]. The strain in these membranes can be compensated by integrating a SiN frame on their top side, as suggested in [25]. The TEY recorded for the fabricated membranes, most likely including the contribution of native oxide formed on both sides of the Si, is 1.3 (Figure 6.4b), and as such does not meet the requirements for the tynode application. Nevertheless, in future work, an effort should be made to attain a stable Cs-termination of these structures and employ them for the TiPC application.

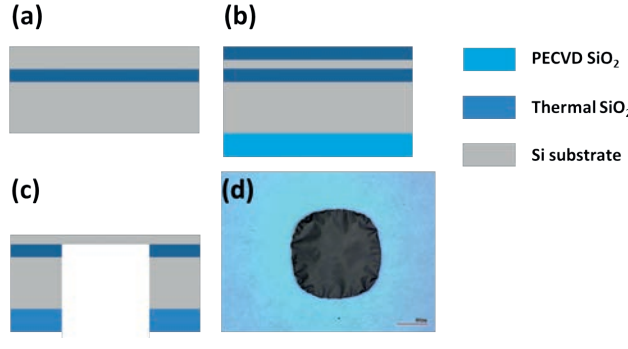

Figure 6.4: Fabrication flow of Si membranes by using SOI wafer as a substrate (a). The top Si film is thinned down to the desired thickness of 40 nm during thermal oxidation (b), after which the newly grown oxide is removed together with the buried oxide in HF vapour (c). Optical micrograph of a 40 nm-thick, 580 × 580 μm^2 Si membrane.

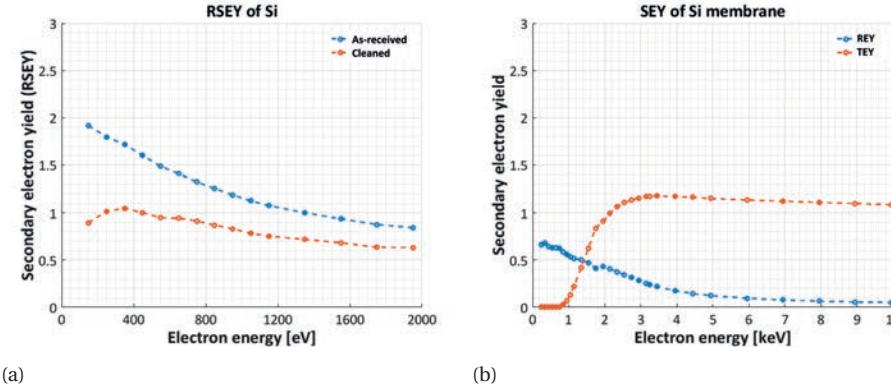

(a) (b)

Figure 6.5: SEY in reflection mode measured for non-treated p-type Si and for Si subjected to HF-cleaning combined with Marangoni drying (a). Total reflection and transmission coefficients measured for 40 nm-thick Si membrane (b).

6.2. CURVED TYNODES

IN the final application, TiPC will utilize vertically-stacked arrays of tynodes. Besides enabling the stacking by adding special features in the design of the final devices, we also investigate a new geometry, replacing flat tynodes with curved ones. This feature provides better performance of the multiplication unit in terms of electron focusing.

6.2.1. FABRICATION OF CURVED TYNODES

As mentioned in Chapter 2, better focusing of electrons within a vertical stack of tynodes can be achieved by fabricating bell-shaped emission surfaces instead of flat ones. Simulations are run in Comsol Multiphysics 5.3, under conditions previously described in Section . Curvature radius of the tynodes is varied in the range from 2.5 to 12.5 µm, and a base diameter is 30 µm. Vertical distance and potential difference between two subsequent tynodes are 100 µm and 500 V, with the detecting chip put to ground. As shown in Figure 6.6, simulations predict the least dissipation of electrons when the top-to-bottom height is around 5 µm. Therefore, the fabrication process for these new tynodes is optimized to achieve this curvature.

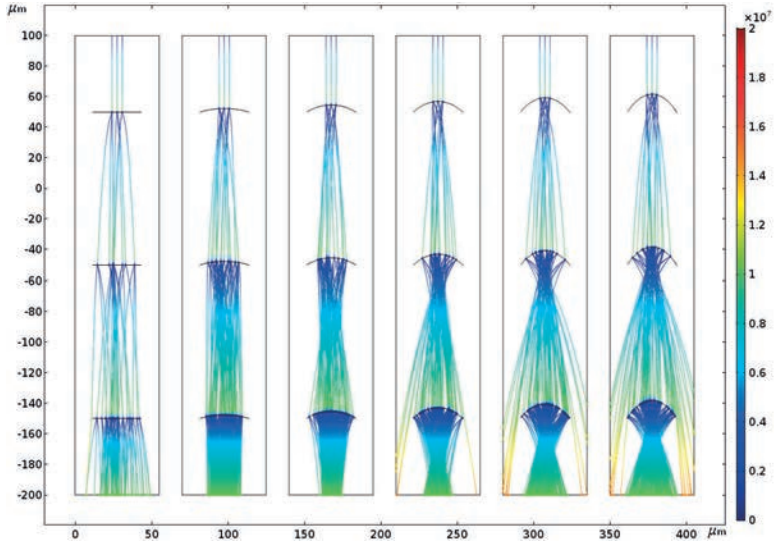

Figure 6.6: Trajectories of electrons in sets of three vertically stacked tynodes with different top-to-bottom heights: flat tynodes, $0.5h$, h, $1.5h$, $2h$, $2.5h$ (from left to right), where h is 5 µm. Simulations were run by using a finite element method in Comsol. The vertical distance between two subsequent tynodes was 100 µm, and the TSEY of the tynode material is 3. Coloured bar on the side quantifes the speed of electrons in m/s.

Thermal reflow of photoresist is a technique proposed by Popovic et al. [26] in 1988, and since then has been widely employed for the fabrication of microlenses [27]. This method was here used to prepare Si spherical caps which later served for moulding of tynodes with better focusing. To our knowledge, this is the first time such method served for the manufacturing of ultra-thin, free standing, curved membranes. To establish the process parameters in the fabrication of Si micro-hemispheres suitable for the

tynode application, we investigated reflow of photoresist patterned by standard lithography steps (coating, UV exposure, developing). In this way cylinders of 8 µm-thick positive photoresist AZ 9260 (supplied by Micro Chemicals) with a base-widths of 20 and 50 µm, are patterned on Si wafers (schematically presented in Figure 6.7a). This step is followed by bake-out of the photoresist cylinders in vacuum at 160 °C, during which the residual solvent evaporates and the surface tension remoulds the melted photoresist into a corresponding spherical shape (Figure 6.7b). The radius of curvature of the reshaped photoresist depends on the diameter of the circular openings on the photomask. In order to determine the optimal bake-out time, wafers are kept in the oven for 30, 60 or 90 min. As plotted in Figure 6.8a, the profiles of photoresist islands with a diameter of 20 µm are almost identical, independently of the bake-out time, with a bottom-to-top dimension of 4.8 µm. Preservation of the shape suggests that the reflow process saturated already within the 30 min-long thermal treatment. For a larger volume of photoresist, with initial diameter of 50 µm, the profile remained the same during 30 and 60 min of thermal reflow (bottom-to-top height equals 5.2 µm), whereas a slight decrease of 0.18 µm in the height was observed after the longest bake-out period (Figure 6.8b).

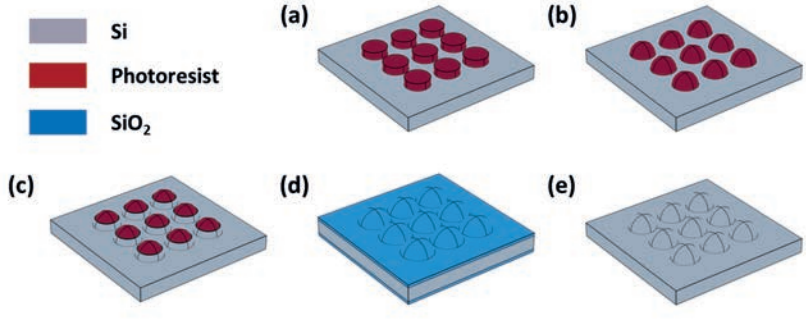

Figure 6.7: Fabrication of Si hemispherical moulds as starting point in the fabrication of curved tynodes and consists of: patterning of photoresist pillars by photolithography (a); thermal reflow during which cylinders are reshaped into spherical droplets (b); transfer of the photoresist features into Si by ICP etching (c) thermal oxidation is employed to reduce the roughness of Si surface (d); after removal of SiO_2 (e), moulded Si substrate is ready for the next steps in the fabrication of tynodes.

Next, inductively coupled plasma (ICP) etching is conducted to transfer the photoresist patterns into the Si substrate (Figure 6.7c). In this process a mixture of SF_6 and O_2 is employed, with volumetric flows of 20 and 50 sccm, respectively. The remaining parameters are identical to the etching procedure reported in a referenced study [28]. Progression of the etch process is monitored by stylus profilometer, and cross sectional profiles of the etched structures are plotted in Figure 6.9. The structure formed after 10.5 min-long etch clearly consists of two parts with different radii of curvature: the upper photoresist cap and a lower silicon part. The calculated etch rate of photoresist was 390 nm/min, whereas for Si was 120 nm/min. These values are almost identical for both chosen geometries of photoresist droplets. Hence, the etch time needed to imprint photoresist droplets as those prepared here is around 30 min. After conducting the etching test, the same processing steps are applied for two different dimensions of final tynode

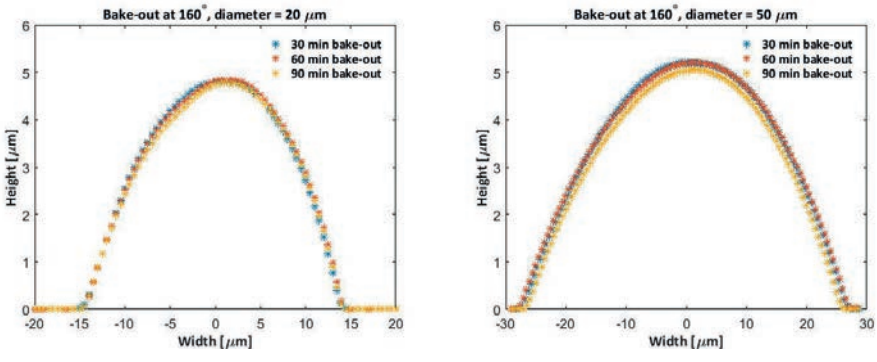

(a) (b)

Figure 6.8: Profile of photoresist after three different bake-out periods for cylinders with a diameter of 20 µm (a) and 50 µm (b). Data was recorded with Vecco stylus profilometer.

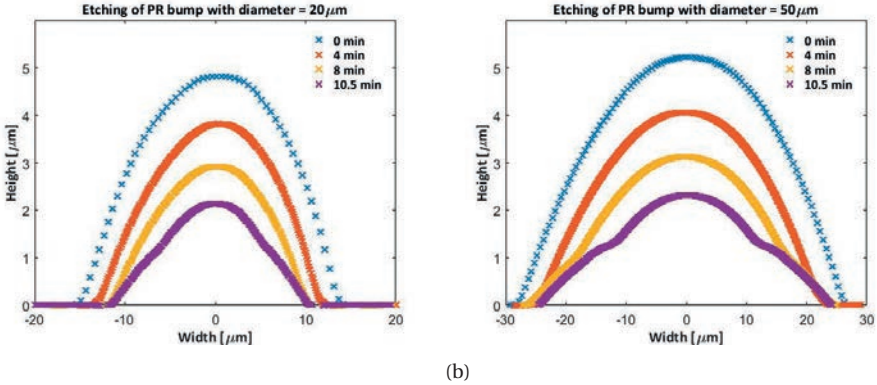

(a) (b)

Figure 6.9: Cross section profiles of structures obtained after 4-, 8-, and 10.5 min-long ICP etching, compared to profiles recorded immediately after thermal reflow. Plot (a) and (b) correspond to an initial diameter of photoresist pillars of 20 and 50 µm, respectively.

arrays (64 × 64 and 128 × 128). The diameter of individual membranes in some tynodes is increased to 45 µm, as opposed to to 10 – 30 µm in the former layout (Chapters 3 – 5). Namely, the base-width of a single active element of the tynode was varied in the range from 30 to 45 µm. The etched Si surface exhibits high surface roughness, with a root mean square (RMS) roughness of 71 nm, as obtained by laser scanning microscope (Keyence VK X250) in a region between Si domes (Figure 6.10a). To reduce the roughness of the Si substrate and provide a smooth surface for the later deposition of the tynode material, wafers are thermally oxidized for 15 hours in a wet environment at 1100 °C (Figure 6.7d). After wet removal of the formed 2.72 µm-thick SiO_2 (Figure 6.7e) in a buffered hydrofluoric acid (HF:NH_4F = 1:7), the Si surface exhibited a significantly reduced roughness (RMS of 12 nm) as shown in Figure 6.10b. By repeating the sequence oxidation – oxide strip, the RMS roughness is further decreased to 4 nm (Figure 6.10c). However, additional smoothening of Si surface closer to the values guaranteed by man-

ufacturer of polished wafers, typically < 1 nm, is not necessary at this moment, since the growth of an ultra-thin tynode film will be preceded by another oxidation and LPCVD of SiN which form the support mesh (as showed earlier in process flow in Figure 3.3). After the release, the 15 nm-thick ALD alumina tynodes with a base diameter of 35 µm have a profile as given in Figure 6.11.

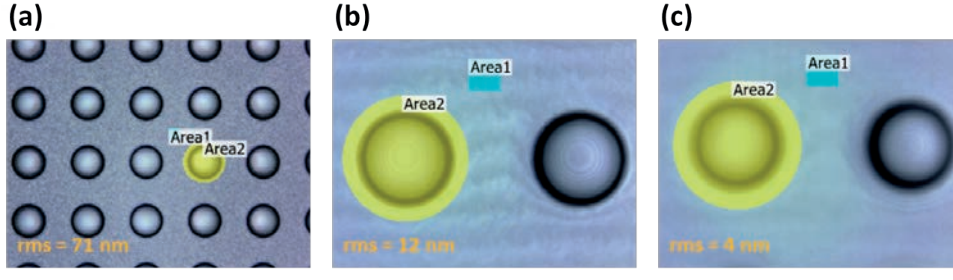

Figure 6.10: Images of tynodes at different fabrication stages, obtained by white light interferometry (WLI), where Area 1 is plain Si surface which was not covered by photoresist prior to dry etching, and Area 2 is a mould. Rough surface after formation of Si hemispheres by ICP etching (a) was significantly smoothened by thermal oxidation and subsequent removal of SiO_2 (b). After being subjected to another thermal oxidation, Si substrate exhibited even lower roughness (c).

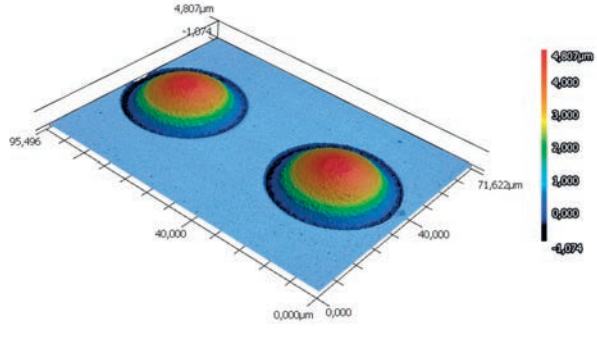

Figure 6.11: Profile of released ALD alumina tynode obtained by white light interferometer.

6.2.2. STACKING OF TYNODES

Next, we developed a method to enable vertical stacking of the tynode chips. With that goal, V-grooves are fabricated on each side of the tynode chip. Tynodes are supported and aligned by Glass rods inserted in these grooves. After moulding the Si substrate into hemispheres (as described in the previous section), follows the oxidation and deposition of LPCVD SiN, which was the starting point in the fabrication of flat tynodes (Figures 3.3 and 4.4). The grooves with dimensions $174.2 \times 12570\ \mu m^2$ are formed on the front side of the tynode chip, by using a KOH (33%) solution and SiN as a masking layer. A mirrored set of openings is made on the back side of the wafers, which are then immersed in KOH

solution, to form grooves on the backside in the same etching step. Using well known etching rates for a given concentration of KOH (33%), temperature of the solution (85 °C) and orientation of Si substrate (100) [29], the etching process is stopped when the depth of the channels reaches 60 µm. These grooves are used as a support for Glass rods with the diameter of 200 µm are placed in the grooves and inserted between two consecutive tynode chips. In this way they provide a precise alignment of the tynodes, which are cut to the size of 15 × 16 mm^2 (to match the exact size of TimePix chip). Different views of the stack are illustrated in Figure 6.12 (drawings not-to-scale), and a preliminary result on the stacking of alumina tynodes is presented in Figure 6.13. Alumina is employed as in-house available material for the proof of concept, and MgO will be used in the final assembling of the TiPC, as it is a more efficient emitter of secondary electrons.

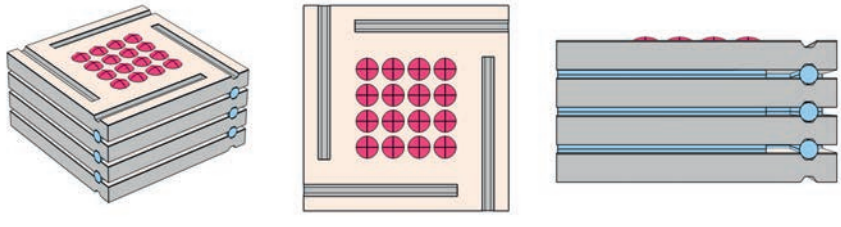

Figure 6.12: A method for the vertical stacking of tynodes. Glass rods inserted in the V-grooves etched on both sides of the chips provide alignment of the arrays of free standing membranes.

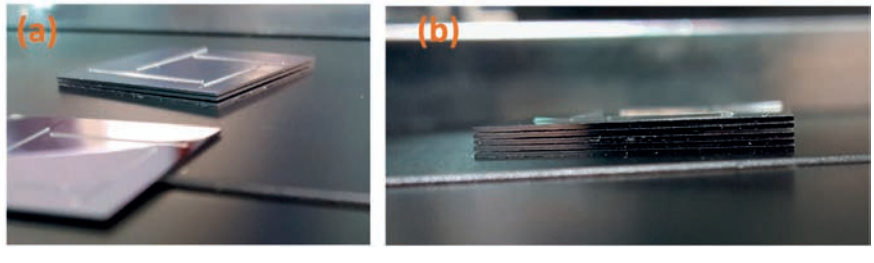

Figure 6.13: First attempts of stacking three (a) and five (b) 15 nm – thick ALD alumina tynodes (courtesy of B. van Loon).

6.2.3. METAL MESH BETWEEN ACTIVE TYNODE AREAS

The hole conductivity of the tynode, and the “horizontal” conductivity should be sufficient to replenish vacancies in order to limit charge-up effects. As described in Section 4.2, this is enabled by TiN sputtered on the emission side of tynodes. However, a thicker metal grid in direct contact with the emission material is desired for a more efficient electron supply. With the same goal, Au film was employed in the fabrication of SiN tynodes (Chapter 3). In the new process, Au is replaced by Al (with 1% of Si content) due to the contamination restrictions in the cleanroom environment used in this work. A 100 nm-

thick Al film is sputtered on the top of SiN layer, followed by patterning of both films and landing on thermal oxide. After this, substrate is ready for the deposition of the tynode material, after which follows opening of contact pads on the chips, outside of the array of membranes. This is performed as a precaution step to connect the metal grid and compensate for the loss of electrons in very thin TiN film which will be deposited on the tynodes. Further steps in the fabrication are identical to the process described in Sections 3.2.2 and 4.2.2. Image of released tynodes with included Al grid are given in Figure 6.14, and detailed fabrication process of the tynodes with these three novel functionalities (moulded silicon substrate, V-grooves and aluminium grid), with ALD alumina as the tynode film, is given in Appendix C.

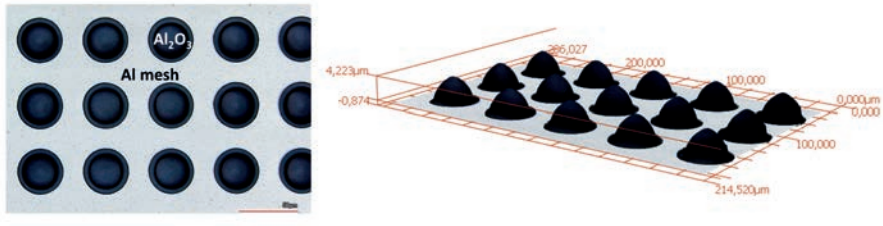

Figure 6.14: Released ALD alumina tynodes with incorporated Al grid for better replenishment of emitted secondary electrons.

6

6.3. CONCLUSIONS

IN this chapter we analysed the SEE properties of four more different films: ALD AlN, LPCVD SiC, monocrystalline Si and UNCD. These materials are chosen on their ability to provide thin free standing membranes, and/or for being efficient emitters of secondary electrons. AlN and SiC provided very low RSEY, and for that reason only UNCD and Si were employed for the fabrication of test membranes for the evaluation of their TSEE. With the yield of 1.3 and 1.8 obtained from Si and UNCD, respectively, these materials proved to be inferior to alumina and magnesium oxide. However, these films should not be discarded as once subjected to surface treatments, significant improvement of their SEE performance could be achieved. Finally, a modified design of the tynodes is presented in this chapter. It contains three major novelties added to the initial design to improve performance and enable the vertical stacking in the TiPC:

- By using a thermal reflow of photoresist, we fabricated Si micro-hemispheres to be used as mould for the tynode grid. This resulted in a dome-shaped surface of individual membranes which can provide better focusing of electrons in a vertical stack of tynodes, as indicated by here presented simulations.

- An embedded alignment structure is implemented in the wafers containing the tynode chips. A set of four elongated pockets is formed on both sides of tynode chips. These grooves will serve as a support for glass rods and will therefore enable the vertical stacking and alignment of tynodes.

- An aluminium grid is implemented in order to eliminate severe charging of underlying SiN film , which negatively affected the TSEE measurements.

REFERENCES

[1] B. Morana, G. Pandraud, J.F. Creemer, and P.M. Sarro. Characterization of LPCVD amorphous silicon carbide (a-SiC) as material for electron transparent windows. *Materials Chemistry and Physics*, 139(2-3):654–662, 2013.

[2] C.I. Wu and A. Kahn. Negative electron affinity and electron emission at cesiated GaN and AlN surfaces. *Applied Surface Science*, 162:250–255, 2000.

[3] S. Banerjee, A.A.I. Aarnink, R. van de Kruijs, A.Y. Kovalgin, and J. Schmitz. PEALD AlN: Controlling growth and film crystallinity. *Physica status solidi (c)*, 12(7):1036–1042, 2015.

[4] A.N. Cleland, M. Pophristic, and I. Ferguson. Single-crystal aluminum nitride nanomechanical resonators. *Applied Physics Letters*, 79(13):2070–2072, 2001.

[5] A. Heidari, Y-J. Yoon, M.I. Lee, L. Khine, M.K. Park, and J.M.L. Tsai. A novel checker-patterned AlN MEMS resonator as gravimetric sensor. *Sensors and Actuators A: Physical*, 189:298–306, 2013.

[6] S. Goerke, M. Ziegler, A. Ihring, J. Dellith, A. Undisz, M. Diegel, S. Anders, U. Huebner, M. Rettenmayr, and H-G. Meyer. Atomic layer deposition of AlN for thin membranes using trimethylaluminum and H_2/N_2 plasma. *Applied Surface Science*, 338:35–41, 2015.

[7] O.A. Shenderova and D.M. Gruen. *Ultrananocrystalline diamond: synthesis, properties and applications*. William Andrew, 2012.

[8] R. Narayan. *Diamond-based materials for biomedical applications*. Elsevier, 2013.

[9] R.M.A. Vaz. *Studies of the secondary electron emission from diamond films*. PhD thesis, University of Bristol, 2013.

[10] Y. Tzeng, S. Yeh, W.C. Fang, and Y. Chu. Nitrogen-incorporated ultrananocrystalline diamond and multi-layer-graphene-like hybrid carbon films. *Scientific reports*, 4:4531, 2014.

[11] A.R. Krauss, O. Auciello, M.Q. Ding, D.M. Gruen, Y. Huang, V.V. Zhirnov, E.I. Givargizov, A. Breskin, R. Chechen, E. Shefer, and et. al. Electron field emission for ultrananocrystalline diamond films. *Journal of Applied Physics*, 89(5):2958–2967, 2001.

[12] B. Bayram and H.S. Altinoluk. Microfabrication of vacuum-sealed cavities with nanocrystalline and ultrananocrystalline diamond membranes and their characteristics. *Diamond and Related Materials*, 20(8):1149–1154, 2011.

[13] O. Auciello, J. Birrell, J.A. Carlisle, Jennifer E. Gerbi, X. Xiao, B. Peng, and H.D. Espinosa. Materials science and fabrication processes for a new MEMS technology based on ultrananocrystalline diamond thin films. *Journal of Physics: Condensed Matter*, 16(16):R539, 2004.

[14] D.K. Reinhard, T.A. Grotjohn, M. Becker, M.K. Yaran, T. Schuelke, and J. Asmussen. Fabrication and properties of ultranano, nano, and microcrystalline diamond membranes and sheets. *Journal of Vacuum Science & Technology B: Microelectronics and Nanometer Structures Processing, Measurement, and Phenomena*, 22(6):2811–2817, 2004.

[15] H.D. Espinosa, B. Peng, B.C. Prorok, N. Moldovan, O. Auciello, J.A. Carlisle, D.M. Gruen, and D.C. Mancini. Fracture strength of ultrananocrystalline diamond thin films—identification of Weibull parameters. *Journal of Applied Physics*, 94(9):6076–6084, 2003.

[16] H. Kim, J. Park, Z. Aksamija, M. Arbulu, and R.H. Blick. Ultrananocrystalline diamond membranes for detection of high-mass proteins. *Physical Review Applied*, 6(6):064031, 2016.

[17] R.U. Martinelli, M.L. Schultz, and H.F. Gossenberger. Reflection and transmission secondary emission from GaAs. *Journal of Applied Physics*, 43(11):4803–4804, 1972.

[18] J.R. Howorth, J.R. Folkes, and I.C. Palmer. Transmission silicon photoemitters and electron multipliers. *Journal of Physics D: Applied Physics*, 9(5):785, 1976.

[19] S. Kobayashi and Y. Saito. Secondary electron emission (SEE) measurements on materials under stress (preliminary measurements of SEE under high temperature (condition). Technical report, Saitama University, Dept. of Electrical and Electronic Systems, 2003.

[20] K. Goto and K. Ishikawa. Method for detecting fine structure in the secondary electron emission yield and the application to Si (111). *Journal of Applied Physics*, 43(4):1559–1562, 1972.

[21] C. Constancias, B. Dalzotto, P. Michallon, J. Wallace, and M. Saib. Fabrication of large area ultrathin silicon membrane: application for high efficiency extreme ultraviolet diffraction gratings. *Journal of Vacuum Science & Technology B, Nanotechnology and Microelectronics: Materials, Processing, Measurement, and Phenomena*, 28(1):194–197, 2010.

[22] J. Cuffe, E. Chavez, A. Shchepetov, P-O. Chapuis, E. H. El Boudouti, F. Alzina, T. Kehoe, J. Gomis-Bresco, D. Dudek, Y. Pennec, and et. al. Phonons in slow motion: dispersion relations in ultrathin Si membranes. *Nano letters*, 12(7):3569–3573, 2012.

[23] E. Chávez-Ángel, J.S. Reparaz, J. Gomis-Bresco, M.R. Wagner, J. Cuffe, B. Graczykowski, A. Shchepetov, H. Jiang, M. Prunnila, J. Ahopelto, and et. al. Reduction of the thermal conductivity in free-standing silicon nano-membranes investigated by non-invasive Raman thermometry. *APL Materials*, 2(1):012113, 2014.

[24] Z.Y. Dang, M. Motapothula, Y.S. Ow, T. Venkatesan, M.B.H. Breese, M.A. Rana, and A. Osman. Fabrication of large-area ultra-thin single crystal silicon membranes. *Applied Physics Letters*, 99(22):223105, 2011.

[25] A. Shchepetov, M. Prunnila, F. Alzina, L. Schneider, J. Cuffe, H. Jiang, E.I. Kauppinen, Sotomayor T.C.M., and J. Ahopelto. Ultra-thin free-standing single crystalline silicon membranes with strain control. *Applied Physics Letters*, 102(19):192108, 2013.

[26] Z.D. Popovic, R.A. Sprague, and N.G.A. Connell. Technique for monolithic fabrication of microlens arrays. *Applied optics*, 27(7):1281–1284, 1988.

[27] D. Daly. *Microlens arrays*. CRC Press, 2002.

[28] A. Jovic, G. Pandraud, K. Zinoviev, J.L. Rubio, E. Margallo, and P.M. Sarro. Fabrication process of Si microlenses for OCT systems. In *Micro-Optics 2016*, volume 9888, page 98880C. International Society for Optics and Photonics, 2016.

[29] K.R. Williams, K. Gupta, and M. Wasilik. Etch rates for micromachining processing-part II. *Journal of microelectromechanical systems*, 12(6):761–778, 2003.

7

CONCLUSION

This study demonstrates the fabrication of various transmission dynodes (tynodes) designed as a large-area arrays of free-standing membranes. The viability of the tynodes produced out of various materials is investigated for the application in a novel photomultiplier - the Timed Photon Counter (TiPC). The results reported in this work are encouraging and, to our knowledge, pioneering in the production of ultra-thin membranes for the electron multiplication. Finally, suggestions for additional to further improve the design and SEE performance of the tynodes are given.

7.1. CONCLUSIONS

This study demonstrates the fabrication of transmission dynodes (tynodes) designed as a large-area arrays of free-standing membranes. The viability of the tynodes produced out of various materials is investigated for the application in a novel photomultiplier - the Timed Photon Counter (TiPC).

This study explored first the applicability of LPCVD Si_xN_y tynode material in the TiPC. Mechanical and structural properties of the films showed that they are qualified for the fabrication of large arrays of strong, homogenous membranes. These SiN membranes exhibit very low tensile stress, high uniformity in thickness, absence of impurities and remarkably smooth surface. However, the LPCVD method proved to have a disadvantage regarding the lower limit in the thickness of the layer, namely the inability to produce good quality, continuous films with thicknesses lower than 20 nm. Thinner tynodes are required for the detection of low-energetic photoelectrons in the TiPC. Also, lower temperature deposition is generally desired since it provides a higher degree of freedom in processing. With the growth temperature of 850 °C, LPCVD of SiN is not suitable for coating temperature sensitive substrates which may be used in reshaping of the tynodes. Finally, we demonstrated that Si_xN_y, with a TEY of app. 1.6 for the 40 nm-thick tynode, is not an efficient secondary electron emitter.

Mechanical and structural properties of the investigated ALD alumina (Al_2O_3) films showed that this material is a good candidate for the fabrication of tynodes with thicknesses down to only 5 nm. All films, grown in the temperature range from 100 to 300 °C, exhibit low tensile stress, high uniformity in thickness, absence of impurities and a very smooth surface (typical for ALD layers). Compared to the LPCVD employed for SiN, the ALD method has two outstanding advantages – it allows growth of high quality films that are even thinner than those obtained by LPCVD technique, and at much lower temperatures. SEE analysis showed that alumina is a more efficient secondary electron emitter, with a TEY of 2.6 for the 10 nm-thick tynode. Further improvement of SEY can be achieved by investigating proper surface termination which may introduce negative electron affinity, in situ surface cleaning of tynodes during the measurement procedure, and by adjusting the shape of the membranes for focusing of secondary electrons.

Large area arrays of ultra-thin (5 –25 nm) free-standing MgO membranes are successfully fabricated and characterized. The optimal film thickness for the secondary emissive ALD MgO membranes was found to be 5 nm, which provided a TEY of 3. This value was further increased to 5.5 after modifying the DFC setup, i.e. by reducing the separation between the sample and collecting grid, and by applying an E-field near the tynode surface. With this, we proved that for TiPC application MgO is better suited than LPCVD SiN and ALD Al_2O_3, due to its better performance in terms of TSEY. Effect of various chemical and thermal treatments on the reflective SEE properties were investigated on MgO, as the best candidate for the TiPC application among the studied materials. A set of experiments is performed to mimic some steps to which the tynode film is exposed throughout the MEMS fabrication. Increased SEY of the treated MgO, compared to as-deposited films, is demonstrated. We explored the effect of two different capping films which were added to prevent the aging of MgO films and their degradation/dissolving

during the fabrication. TEOS-based oxide turned out to be a more beneficial capping film (compared to silane-based oxide), providing the elevation of the maximum RSEY from 4.8 to 6.6 for 25 nm-thick MgO. In addition, we performed annealing of MgO at high temperatures and validated that this also improved the SEE performance. In this set of samples, the highest SEY of 7.2 was recorded after annealing of 25 nm thick MgO at 900°C. AFM scanning revealed a drastic change of surface morphology after the annealing steps, whereas XPS data suggests the formation of complex magnesium silicates and silicides already in the close-to-surface area. As future work, an examination of the electron affinity (or other properties related to the energy band of material) is suggested for a better understanding on how surface and composition modifications affect the SEE of thin MgO films.

SEE properties of four more different films were investigated, namely, ALD AlN, LPCVD SiC, monocrystalline Si and ultrananocrystalline diamond (UNCD). These materials were chosen on their ability to provide thin free standing membranes, and/or for being efficient emitters of secondary electrons. AlN and SiC provided very low RSEY, and for that reason only UNCD and Si were employed for the fabrication of test membranes for the evaluation of their TSEE. With the yield of 1.5 and 1.2 obtained from Si and UNCD, respectively, these materials proved to be inferior to alumina and magnesium oxide. However, in the future work, these films should be subjected to surface treatments conducted in order to improve their SEE performance.

The design and fabrication of the tynodes presented in this chapter consists of three major novelties added to improve their performance and enable the vertical stacking in the TiPC:

- By using a thermal reflow of photoresist, we demonstrated the fabrication of silicon hemispherical islands which served as a substrate for the tynode grid. This resulted in a dome-shaped surface of individual membranes, predicted to provide better focusing of electrons in a vertical stack of tynodes;
- A set of four elongated pockets was formed on both sides of the tynode chips. These grooves will serve as a support for glass rods and will therefore enable the vertical stacking and alignment of tynodes;
- Aluminium grid in between active tynode parts was implemented in order to eliminate severe charging of the underlying SiN film, which obstructed the TSEE measurements. The gold layer initially applied for the SiN tynodes was replaced by aluminium. This modification simplified the fabrication of novel tynodes due to the higher compatibility of Al in the cleanroom processing.

7.2. RECOMMENDATIONS FOR FUTURE WORK

Even though the results reported in this work are encouraging and, to our knowledge, pioneering in the production of ultra-thin membranes for the electron multiplication, further work should be conducted to improve the SEE performance of the tynodes and finalize the work on their vertical stacking for the final implementation in the TiPC.

- **Thermal treatments for enhancing the TSEE of MgO**. As shown in Chapter 5, thermal annealing of MgO deposited on Si substrate improved its RSEY. The same steps should be included in the fabrication of the MgO tynodes. To prevent potential damage of the very thin tynodes during this procedure, it is preferred to perform it immediately after the deposition of the MgO film.

- **Fabrication of curved MgO tynodes**. Due to in-house availability of ALD alumina, the concept of curved tynodes is demonstrated only on this material. Similar design should be applied to ALD MgO, as it performed better in terms of electron multiplication.

- **Making the most out of diamond**. UNCD investigated in this work exhibited a rather low TSEY, even though diamond is one of the most efficient materials in the electron multiplication (as discussed in Sections 2.2.1 and 2.4.1). The effect of surface treatments on SEY of UNCD should be looked into. Compared to the procedure reported in Section 6.1.3, longer bake-out times at a higher temperature and in a high vacuum environment are suggested. Another limitation of UNCD films we reported on is their thickness. Other deposition methods of UNCD or different types of diamond should be explored to enable the fabrication of tynodes with a thicknesses of 50 nm or less.

- **Scaling up tynodes area**. The tynodes fabricated so far do not cover all the pixelized area of the CMOS detecting chip (256×256 pixels on 15×16 mm^2 area). An approach to produce such large tynodes by using ALD MgO would be etching 2×2 DRIE windows (of the same size, or slightly smaller) on a single tynode chip (instead of one opening as shown in Figure 5.2). The width of the Si support is then defined by the separation between these windows and should be optimized to provide robustness of the released tynode.

- **Validation of the focusing effect**. Vertically stacked curved tynodes reported in Chapter 6 should be clamped and investigated in a DFC setup modified to allow such measurements.

A

APPENDIX A

This Appendix gives an overview of steps in the fabrication of SiN tynodes discussed in Chapter 3.

- Substrate: 4-inch Si (100) wafers with the thickness of 300 µm, double-side polished;
- Lithography steps for alignment markers on the front side of wafers
  1. Coating of 1.4 µm-thick positive photoresist (SPR 3012) in EVG 120 (recipe: co_3012_zerolayer);
  2. Exposure in ASML PAS 5500/80 (job: zefwam);
  3. Developing in EVG 120 (recipe: dev_sp);
- Plasma etching of alignment markers in Trikon Omega (recipe: urk_npd)
- Standard Si cleaning procedure (oxygen plasma cleaning, immersion in HNO_3 (99%), rinsing in de-ionized (DI) water, immersion in HNO_3 (69.5%), DI water rinsing and drying);
- Protection layer for the release of the tynodes: 500 nm-thick thermal oxide (wet oxidation process);
- Support layer for the tynodes: LPCVD of 500 nm-thick SiN ("Type 1'' in Table 3.1);
- Lithography steps for forming the supporting grid:
  - Coating of 1.4 µm-thick positive photoresist (SPR 3012) in EVG 120 (recipe: co_3012_1.4um);
  - Exposure in ASML PAS 5500/80 (structures "Circles'' in a multi-image mask Tynode);
  - Developing in EVG 120 (recipe: dev_sp);

A

- Dry etching of the grid in Drytek Triode 384T (consuming 500 nm and up to 100 nm of SiO_2 (recipe: stdsin) and smoothening the SiO_2 surface in BHF 1:7;
- Standard Si cleaning procedure (oxygen plasma cleaning, immersion in HNO_3 (99%), rinsing in DI water, immersion in HNO_3 (69.5%), DI water rinsing and drying);
- Lithography steps for KOH openings on the backside:
  - Coating of 2.1 µm-thick positive photoresist (SPR 3012) in EVG 120 (recipe: co_3012_2.1um_noEBR);
  - Exposure in ASML PAS 5500/80 (structures "Big windows'' in a multi-image mask "Tynode'' and a separate mask "Scribe 20 × 20'');
  - Developing in EVG 120 (recipe: dev_sp);
- Dry etching of SiN and /chSiO2 in Drytek Triode 384T;
- Standard Si cleaning procedure (oxygen plasma cleaning, immersion in HNO_3 (99%), rinsing in DI water, immersion in HNO_3 (69.5%), DI water rinsing and drying);
- Deposition of the tynode film: 20 and 40 nm-thick LPCVD SiN ("Type 1'' and "Type 2'' in the Table 3.1). Recipe 4inchvar in LPCVD tube E2;
- Lithography steps for Au metallization:
  - Coating of 3.5 µm-thick negative photoresist in EVG 120 (recipe: co_nlof_3.5um);
  - Exposure in contact aligner EVG 420;
  - Soft bake at 115 °C and developing in EVG 120 (recipe: dev_liftoff).
- Evaporation of Au (100 nm) with 10 nm-thick Cr film to improve adhesion (Balzers evaporator);
- Liftoff of Au in ultrasonic acetone solution heated to 75 °C (time: 45 min);
- Release of tynodes: KOH etching of Si substrate (33% KOH solution, constantly stirred and kept at 85 °C), rinsing in DI water and removal of SiO_2 in HF (0.55%).

B

APPENDIX B

This Appendix gives an overview of steps in the fabrication of ALD Al_2O_3 and MgO tynodes discussed in Chapters 4 and 5.

- Substrate: 4-inch Si (100) wafers with the thickness of 300 µm, double-side polished;
- Lithography steps for alignment markers on the front side of wafers:
  - Coating of 1.4 µm-thick positive photoresist (SPR 3012) in EVG 120 (recipe: co_3012_zerolayer);
  - Exposure in ASML PAS 5500/80 (job: zefwam);
  - Developing in EVG 120 (recipe: dev_sp).
- Plasma etching of alignment markers in Trikon Omega (recipe: urk_npd);
- Standard Si cleaning procedure (oxygen plasma cleaning, immersion in HNO_3 (99%), rinsing in de-ionized (DI) water, immersion in HNO_3 (69.5%), DI water rinsing and drying);
- Protection layer for the release of the tynodes: 500 nm-thick thermal oxide (wet oxidation process);
- Support layer for the tynodes: LPCVD of 500 nm-thick SiN ("Type 1'' in Table 3.1);
- Lithography steps for forming the supporting grid:
  - Coating of 1.4 µm-thick positive photoresist (SPR 3012) in EVG 120 (recipe: co_3012_1.4um);
  - Exposure in ASML PAS 5500/80 (structures "Circles'' in a multi-image mask Tynode);
  - Developing in EVG 120 (recipe: dev_sp).

- Dry etching of the grid in Drytek Triode 384T (consuming 500 nm and up to 100 nm of SiO_2 (recipe: stdsin) and smoothening the SiO_2 surface in BHF 1:7;
- Standard Si cleaning procedure (oxygen plasma cleaning, immersion in HNO_3 (99%), rinsing in DI water, immersion in HNO_3 (69.5%), DI water rinsing and drying);
- Lithography steps for large windows on the backside:
  - Coating of 2.1 µm-thick positive photoresist (SPR 3012) in EVG 120 (recipe: co_3012_2.1um_noEBR);
  - Exposure in ASML PAS 5500/80 (structures "Big windows'' in a multi-image mask "Tynode'' and a separate mask "Scribe 20 × 20'');
  - Developing in EVG 120 (recipe: dev_sp).
- Dry etching of SiN and /chSiO2 in Drytek Triode 384T;
- Standard Si cleaning procedure (oxygen plasma cleaning, immersion in HNO_3 (99%), rinsing in DI water, immersion in HNO_3 (69.5%), DI water rinsing and drying);
- Deposition of the tynode film: 5 - 25 nm-thick ALD Al_2O_3 (grown in ASM F-120 reactor) or MgO (supplied by Argonne National Lab);
- Protection film on top of the tynode film: PECVD oxide (1 µm-thick, deposited at 350 or 400 °C in Novellus Concept 1);
- Release of the tynodes: removal of Si substrate by DRIE (Rapier Omega i2L) and removal of SiO_2 in HF vapour (Primax microetch SPTS);
- Conductive layer to reduce charging up: sputtering of 2 – 2.5 nm-thick TiN (Trikon Sigma 204, at 25 °C).

C

APPENDIX C

As an Appendix to Chapter 6, this section gives the overview of steps in the fabrication of the curved ALD Al_2O_3 tynodes. The process includes formation of grooves which enable vertical stacking and alignment of the tynodes, as well as metal (aluminium) grid to overcome charging up (in addition to sputtered TiN).

- Substrate: 4-inch Si (100) wafers with the thickness of 300 µm, double-side polished;
- Lithography steps for alignment markers on the front side of wafers:
  - Coating of 1.4 µm-thick positive photoresist (SPR 3012) in EVG 120 (recipe: co_3012_zerolayer);
  - Exposure in ASML PAS 5500/80 (job: zefwam);
  - Developing in EVG 120 (recipe: dev_sp).
- Plasma etching of alignment markers in Trikon Omega (recipe: urk_npd);
- Standard Si cleaning procedure (oxygen plasma cleaning, immersion in HNO_3 (99%), rinsing in de-ionized (DI) water, immersion in HNO_3 (69.5%), DI water rinsing and drying);
- Lithography steps for alignment markers on the backside of wafers:
  - Coating of 1.4 µm-thick positive photoresist (SPR 3012) in EVG 120 (recipe: co_3012_zerolayer);
  - Exposure in ASML PAS 5500/80 (job: ftba);
  - Developing in EVG 120 (recipe: dev_sp).
- Plasma etching of alignment markers in Trikon Omega (recipe: urk_npd);
- Standard Si cleaning procedure (oxygen plasma cleaning, immersion in HNO_3 (99%), rinsing in de-ionized (DI) water, immersion in HNO_3 (69.5%), DI water rinsing and drying);

- Lithography steps for the formation of Si bumps:
  - Coating of 6 – 10 µm-thick positive photoresist (AZ 9260) in EVG 120;
  - Exposure in ASML Pas 5500/80 (structures "Circles_inv'' in a multi-image mask Tynode);
  - Manual developing in EVG 120 (mixture of H_2O and developer AZ400K).
- Bake-out in air, performed to reshape photoresist pillars into droplets (30 - 90 min at 160 °C);
- Plasma etching of Si and photoresist to form hemispherical Si islands (Trikon Omega);
- Standard Si cleaning procedure (oxygen plasma cleaning, immersion in HNO_3 (99%), rinsing in de-ionized (DI) water, immersion in HNO_3 (69.5%), DI water rinsing and drying);
- Thermal oxidation for smoothening the Si surface (2 µm-thick SiO_2) and stripping of SiO_2 in BHF 1:7;
- Protection layer for the release of the tynodes: 500 nm-thick thermal oxide (wet oxidation process);
- Support layer for the tynodes and mask for KOH etching: LPCVD of 500 nm-thick SiN ("Type 1'' in Table 3.1);
- Lithography steps for forming the V-grooves on the front side:
  - Coating of 1.4 µm-thick positive photoresist (SPR 3012) in EVG 120 (recipe: co_3012_1.4um);
  - Exposure in ASML PAS 5500/80 (structures "Circles'' in a multi-image mask Tynode);
  - Developing in EVG 120 (recipe: dev_sp).
- Dry etching in Drytek Triode 384T (consuming 500 nm and 500 nm of SiO_2 (recipes: stdsin and stdoxide);
- Standard Si cleaning procedure (oxygen plasma cleaning, immersion in HNO_3 (99%), rinsing in de-ionized (DI) water, immersion in HNO_3 (69.5%), DI water rinsing and drying);
- Lithography steps for forming the V-grooves on the backside:
  - Coating of 1.4 µm-thick positive photoresist (SPR 3012) in EVG 120 (recipe: co_3012_1.4um);
  - Exposure in ASML PAS 5500/80 (structures "Circles'' in a multi-image mask Tynode);
  - Developing in EVG 120 (recipe: dev_sp).
- Dry etching in Drytek Triode 384T (consuming 500 nm and 500 nm of SiO_2 (recipes: stdsin and stdoxide);
- Standard Si cleaning procedure (oxygen plasma cleaning, immersion in HNO_3 (99%), rinsing in de-ionized (DI) water, immersion in HNO_3 (69.5%), DI water rinsing and drying);

- Etching of V-grooves on both sides of wafers in KOH 33/
- Deposition of the metal film (sputtering of 100 nm-thick Al (with 1/
- Lithography steps for forming the support grid:
  - Coating of 1.4 µm-thick positive photoresist (SPR 3012) in EVG 120 (recipe: co_3012_1.4um);
  - Exposure in ASML PAS 5500/80 (structures "Circles'' in a multi-image mask "Tynode'');
  - Developing in EVG 120 (recipe: dev_sp);
- Patterning of the metal film and supporting SiN-SiO_2 grid:
  - Plasma etching of Al in Trikon Omega (recipe: al1000);
  - Plasma etching of the gridDrytek Triode 384T (consuming 500 nm and up to 100 nm of SiO_2 (recipe: stdsin);
  - Smoothening the SiO_2 surface in BHF 1:7;
- Standard metal cleaning procedure (oxygen plasma cleaning, immersion in HNO_3 (99%), rinsing in DI water and drying);
- Deposition of the mask layer for the DRIE etching on the backside of wafers (3 µm-thick PECVD oxide grown in Novellus Concept 1);
- Lithography steps for large windows on the backside of wafers:
  - HMDS treatment (10 min);
  - Spray-coating of positive photoresist to cover the V-grooves (AZ9260) in EVG 101 (3× recipe HP_1000mbar_2ml_8layers with baking steps at 115 °C in between);
  - Exposure in ASML PAS 5500/80 (structures "Big windows'' in a multi-image mask "Tynode'' and a separate mask "Scribe 20 × 20'');
  - Manual developing in the mixture of AZ400K developer and H_2O;
- Dry etching of SiN and SiO_2 on the backside of wafers in Drytek Triode 384T (recipes: stdsin and stdoxide);
- Standard metal cleaning procedure (oxygen plasma cleaning, immersion in HNO_3 (99%), rinsing in DI water and drying);
- Deposition of the tynode film: 5 - 25 nm-thick ALD Al_2O_3 (grown in ASM F-120 reactor);
- Protection film on top of the tynode film: PECVD oxide (1 µm-thick, deposited at 350 or 400 °C in Novellus Concept 1);
- Release of the tynodes: removal of Si substrate by DRIE (Rapier Omega i2L) and removal of SiO_2 in HF vapour (Primax SPTS);
- Conductive layer to reduce charging up: sputtering of 2 – 2.5 nm-thick TiN (Trikon Sigma 204, at 25 °C).

ACKNOWLEDGEMENTS

After many iterations of writing in technical language, I am finally facing a long awaited freedom of style reserved for this section. While taking delight in this moment, please allow me to switch to a less formal voice and express my appreciation to all of you who accompanied me on this (longer than anticipated) journey.

First and foremost, I am deeply grateful to my promoters, Prof. Sarro and Prof. van der Graaf, for the great opportunity to be a part of the MEMBrane project. Thank you for your patience, guidance, all the revisions and counsel throughout my research.

For countless fruitful discussions and valuable scinetific input, I would like to express my gratitude to other collaborators within MEMBrane project: Annemarie, Bram, Conny, Daan, Gert, Hassan, John Smedley, John Sinnsheimer, Kees, Thijs, Wouter, Yevgen and my former colleagues at Nikhef. Hong Wah, it has been a great deal of fun working on this project (and exploring Berlin) with you! Some of the results presented wouldn't have been produced without help provided by Ani, Anil and Jeffrey from Argonne National Lab. I am also in owe to Floriana, Matthias and Ralu, with whom I shared memorable moments at ALD conferences.

Just like any story, this one too has a prologue, in which one of the main roles was delivered by Marko Mihailović. Thank you for bringing me into contact with Prof. Sarro and for being a survival guide in the first months of my life in the Netherlands. Iwill forever have fond memories of your extensive lectures in etymology and some great adventures (mostly coordinated with minimal planning).

Conducting research in a cleanroom is impossible without team work and sharing the knowledge in processing. For all the advice and help provided throughout my PhD, I am in debt to present and former members of ECTM department and other frequent users of cleanroom facilities: Amir M, Amir S, Andrea, Angela, Aslihan, Boyao, Bruno, Brahim, Cinzia, Daniel, Delphine, Enrico, Fabio, Federico, Filiberto, Gianluca, Gianpaolo, Giuseppe, Guangtao, Hande, Hang, Jin, Jian, Joost M, Joost R, Joost van G, Juan, Levar, Luke, Manju, Marian, Marta, Martin, Maryam, Massimo, Miki, Milica, Niko, Paul, Pan, Pelin, Pengfei, Rene, Robert, Ronaldo, Salvatore, Sarat, Shinnosuke, Sourish, Sten, Thomas, William, Xueming, Yelena, Yu, Yue and Zahra. Thank you for pulling together through every pre-maintenance madness, for enriching my magnet collection and for being a great company during so many meals in the canteen.

To all Else Kooi Laboratory stuff members (and my current colleagues), I am grateful for all the effort and quick actions taken to ensure safe and smooth operation both inside and outside the cleanroom. Alex, Bart, Bianca, Cassan, Giles, Henk,

Hugo, Hitham, Jan, Jan Cornelis, Jia, Joost, Johan, Johannes, Jord, Koos, Loek, Mario, Michiel, Paolo, Paul, Robert, Ron, Ruud, Tom, Vincent, Vinod, Wim T, Wim W, you have all been a reliable support at EKL. Charles, thank you for all the precious assistance with processing in Kavli lab.

Aleksandar, I was lucky to start my PhD journey around the same time as you. Over these six years you have always been a close and reliable friend who helped in getting through all kind of storms. I am proud of all your accomplishments and the way you set your new life in the Netherlands, from a scratch. To Silvana, I am deeply grateful for advice and support in both career and private related matters. It has been a true privilege having such a motherly figure around and learning from your patience, kindness and righteousness. I am looking forward to many more exchanges of our reading experiences, regardless of what corner of the world life brings me to. Gregory, I very much appreciate all the advice you provided in moments of panic. Thank you for being endlessly creative and ready to help with the challenges of processing. I would also like to thank Casper Juffermans for giving me the chance to work on exciting projects for EKL.

Once upon a time in fair Delft, there was a flourishing Balkan community. Today, after many graduations and job applications, the group of people I got to know as a newbie in this town, has scattered all over the Netherlands and world. For many laughs and our amusing gatherings, I am grateful to: Andrija, Branko, Dejan, Dimitrije, Ivan, Marija, Mladena, Stevan N, Stevan R, Uroš and families Somić and Pavlović. Jelena, I appreciate the warm welcome and all the effort you and your family put into making me feel a little more like at home in the Netherlands.

Habibi, our encounter is one of my favorite oddities that happened on a dance floor. The chivalry you offered to a damsel in distress was truly moving and it certainly did not deserve that one extra digit. Even with such a rough start of our friendship, I hope you will never forget to not ignore.

People from province recognize the importance of having *that one* friend living in Amsterdam, the one who often save us from boredom of weekends in Delft. Gjorgji, your cozy burrow has been a safe harbour over past two years, but that is only a cherry on top of your intelligence, charm and devotion as a friend. Thank you for introducing me to your sister Lilika, who proved that talent is running in the family. Darling, a love affair between you and your camera is the best one I know, and I am certain it will attract many great opportunities in your life. Please keep on freezing all the beautiful moments!

Some bonds seem to put up so well in spite of distance and time, and such one is with EESTEC milieu (this category people is deserving of being described with such pompous words). My dear board members, the series of events and life changes you have all gone through since our university days are simply... stupendous. Back in the university days, I couldn't have imagined you would reach such a level of maturity. Aleksandar, Andrija, Biljana, Gordana, Janko, Jovan, Marko, Milena N, Milena M, Pavle, Saša, Tihomir, it will always be a great pleasure to catch up with you!

The last thank you note is reserved for my loving family - my parents and brother who, each in their own way, have been real-life heroes for me. Mom and dad, I will forever be in your debt for all the sacrifices made for me, and for all the times you set a good example on how to stay strong and pick yourself up in rough times. I love you to bits!

LIST OF PUBLICATIONS

CONFERENCE PROCEEDINGS AND JOURNAL PAPERS

1. H. van der Graaf, H. Akhtar, N. Budko, H.W. Chan, C.W. Hagen, C.C.T. Hansson, G. Nützel, S.D. Pinto, **V. Prodanović**, B. Raftari, et al. *The tynode: A new vacuum electron multiplier*, Nuclear Instruments and Methods in Physics Research Section A: Accelerators, Spectrometers, Detectors and Associated Equipment, 847, 148-–161, 2017.
2. **V. Prodanović**, H.W. Chan, H. van der Graaf, and P.M. Sarro, *Ultra-thin alumina and silicon nitride MEMS fabricated membranes for the electron multiplication*, Nanotechnology, 29(15), 155703, 2018.
3. **V. Prodanović**, H.W. Chan, A.U. Mane, J.W. Ellam, M.M. Minjauw, C. Detavernier, H. van der Graaf, and P.M. Sarro, *Effect of thermal annealing and chemical treatments on secondary electron emission properties of atomic layer deposited Mg*, Journal of Vacuum Science Technology A, 36, 06A102, 2018.
4. **V. Prodanović**, H.W. Chan, J. Smedley, A. Theulings, S. Tao, H. van der Graaf, and P.M. Sarro, *Optimization of silicon-rich silicon nitride films for electron multiplication in timed photon counters*, 29$^{\text{th}}$ Eurosensors Conference, Procedia Engineering, 120, 1111–1114, 2015.
5. **V. Prodanović**, H.W. Chan, A.U. Mane, J.W. Elam, H. van der Graaf, and P.M. Sarro, *Ultra-thin ALD MgO membranes as MEMS transmission dynodes in a timed photon counter*, 30$^{\text{th}}$ IEEE International Conference on Micro Electro Mechanical Systems (MEMS), 740–743, 2017.
6. S. Tao, A. Theulings, **V. Prodanović**, J. Smedley, and H. van der Graaf, *Optical properties of silicon-rich silicon nitride ($Si_xN_yH_z$) from first principles*, MDPI Computation, 3(4), 657–669, 2015.
7. L. Goossen, J. Wei, G. Pandraud, **V. Prodanović**, and P.M. Sarro, *Ultra-thin integrated ALD Al_2O_3 electron-transparent windows for TEM nanoreactor applications*, 32$^{\text{nd}}$ Eurosensors Conference, MDPI Proceedings, 2(13), 1001–1004, 2018.
8. Y. Bilevych, S.E. Brunner, H.W. Chan, E. Charbon, H. v.d. Graaf, C.W. Hagen, G. Nützel, S.D. Pinto, **V. Prodanović**, D. Rotman, et. al. *Potential applications of electron emission membranes in medicine*, Nuclear Instruments and Methods in Physics Research Section A: Accelerators, Spectrometers, Detectors and Associated Equipment, 809, 171–174, 2016
9. S. Tsigaridas, M v. Beuzekom, H.W. Chan, H. v.d. Graaf, F. Haartjes, K. Heijhoff, N.P. Hessey, and **V. Prodanović** Towards spark-proof gaseous pixel detectors, Journal of Instrumentation, 11, C11016, 2016.
10. S. Tsigaridas, M v. Beuzekom, H. v.d. Graaf, F. Haartjes, K. Heijhoff, N.P. Hessey, P.J. Jong and **V. Prodanović** *Timewalk correction for the Timepix3 chip obtained with real particle data*, Nuclear Instruments and Methods in Physics Research Section A: Accelerators, Spectrometers, Detectors and Associated Equipment, 930, 185–190, 2019.

CONFERENCE PRESENTATIONS

1. "Micro-machined low-stress silicon nitride transmission dynode for electron amplification", IEEE NSS/MIC 2014, Seattle, Washington (USA), November 2014.
2. "Low-stress ultra-thin ALD alumina membranes for timed photon counter", AVS ALD/ALE 2016, Dublin, Ireland, July 2016.
3. "Thermal annealing effects on electron emission properties of ALD MgO", AVS ALD/ALE 2017, Denver, Colorado (USA), July 2017.